Monthly Notices
of the
ROYAL ASTRONOMICAL SOCIETY

MNRAS **468,** 4902–4937 (2017)
Advance Access publication 2017 March 29

doi:10.1093/mnras/stx749

A new method to unveil *blazars* among multiwavelength counterparts of unassociated *Fermi* γ-ray sources

S. Paiano,[1,2,3]★ A. Franceschini[1,2] and A. Stamerra[4,5]

[1]*Dipartimento di Fisica e Astronomia, Università di Padova, vicolo dell'Osservatorio 3, I-35122 Padova, Italy*
[2]*INAF – Osservatorio Astronomico di Padova, vicolo dell'Osservatorio 5, I-35122 Padova, Italy*
[3]*INFN – Sezione di Padova, via Marzolo 8, I-35131 Padova, Italy*
[4]*INAF – Osservatorio Astrofisico di Torino, via P. Giuria 1, I-10125 Torino, Italy*
[5]*Scuola Normale Superiore, Piazza dei Cavalieri, 7, I-56126 Pisa, Italy*

Accepted 2017 March 24. Received 2017 March 23; in original form 2015 February 11

ABSTRACT

We discuss a new method for unveiling the possible *blazar* active galactic nucleus nature among the numerous populations of unassociated gamma-ray sources (UGSs) in the *Fermi* catalogues. Our tool relies on the positional correspondence of the *Fermi* object with X-ray sources (mostly from *Swift*-XRT), correlated with other radio, infrared and optical data in the field. We built a set of spectral energy distribution templates representative of the various *blazar* classes, and we quantitatively compared them to the observed multiwavelength flux density data for all *Swift*-XRT sources found within the *Fermi* error box, by taking advantage of some well-recognized regularities in the broad-band spectral properties of the objects. We tested the procedure by comparison with a few well-known *blazar*s, and tested the chance for false-positive recognition of UGSs against known pulsars and other Galactic and extragalactic sources. Based on our spectral recognition tool, we find the *blazar* candidate counterparts for 14 2FGL UGSs among 183 selected at high galactic latitudes. Furthermore, our tool also allows us to obtain rough estimates of the redshift for the candidate blazar. In a few cases in which this has been possible (i.e. when the counterpart was an SDSS object), we verified that our estimate is consistent with the measured redshift. The estimated redshifts of the proposed UGS counterparts are larger, on average, than those of known *Fermi blazar*s, a fact that might explain the lack of previous association or identification in published catalogues.

Key words: galaxies: active – gamma-rays: galaxies – BL Lacertae objects: general.

1 INTRODUCTION

The *Fermi* gamma-ray observatory (Atwood et al. 2009) is contributing to dramatic progress in the field of high-energy astrophysics. With its high-throughput, almost instantaneous all-sky vision, the mission has offered not only a 10-fold increase in the number of catalogued sources from 100 MeV to 100 GeV, with respect to previous γ-ray missions, but also a continuous monitoring for variability studies and a huge spectral coverage (Abdo et al. 2009, 2010; Nolan et al. 2012; Acero et al. 2015).

As it often happens with new revolutionary astronomical facilities put in operation, the *Fermi* mission is also producing unexpected outcomes: Of the 1873 sources in the Second Catalogue of the Large Area Telescope (2FGL; Nolan et al. 2012), as many as one-third (576 sources) are lacking reliable association with sources detected at other wavelengths, henceforth the unassociated gamma-ray sources (UGSs). Many more can also be found in the last release of the *Fermi* catalogue (3FGL), where 1011 sources are unassociated among the 3034 objects reported.

The majority (about one thousand) of the 1297 *Fermi* associated sources in the 2FGL have been classified as active galactic nuclei (AGNs), in particular, *blazar*s [BL Lac objects and flat-spectrum radio quasars (FSRQs)]. It is thus likely that a large number of the UGSs might hide previously unknown sources of this category.

*Blazar*s are the most extreme engines of nature, producing the largest amount of radiant energy among other cosmic sources. From a sub-parsec-scale region, they accelerate entire plasma clouds to relativistic speeds, transforming fast (even maximally) rotating supermassive black holes and gravitational energy into radiation and mechanical power.

*Blazar*s are not only unique machines to test extreme physics, but can also be exploited as lighthouses to probe the distant universe. Their emitted very high energy (VHE; $E > 100$ GeV) photons are known to interact with the low-energy-photon backgrounds (the extragalactic background light (EBL), e.g. Franceschini, Rodighiero & Vaccari 2008) and decay into e^-–e^+ pairs. So, observations of the *blazar* VHE spectra and their spectral absorption, for example, with

★ E-mail: simona.paiano@oapd.inaf.it

the Cherenkov observatories or *Fermi* satellite itself, are used to test the EBL (e.g. Aharonian et al. 2006; Ackermann et al. 2012). In this regard, the identification of distant and high-redshift *blazar*s at high energies is particularly relevant, among others, to estimate the earliest EBL components due to the first-light sources (Population III stars, galaxies or quasars) in the universe (see e.g. Franceschini & Rodighiero 2017).

Expanding our knowledge of the *blazar* population at high energies and high redshifts is then a priority topic for various reasons. Several papers in the literature are dedicated to methods for the identification of the *Fermi* unassociated sources. Ackermann et al. (2012), Mirabal et al. (2012) and Doert & Errando (2014) developed statistical algorithms based on selected UGS gamma-ray features, such as spectral and variability information, to be able to discriminate between AGNs and pulsars. Other works focused on the search for AGN candidates among the 2FGL UGSs by analysing their long-wavelength counterparts: Petrov et al. (2013) and Schinzel et al. (2015) compiled a thorough catalogue of the Australia Telescope Compact Array radio sources lying inside the UGS error boxes. Other radio surveys were published by Nori et al. (2014) and Giroletti et al. (2016). Massaro et al. (2011, 2012) and D'Abrusco et al. (2013) proposed AGN candidates on the basis of the colours of the infrared (IR) counterparts in the *Wide-field Infrared Survey Explorer* (*WISE*) survey lying within the *Fermi* error ellipses. In Paggi et al. (2013), a complete analysis of the X-ray data provided by the *Swift* satellite has been performed to search for X-ray counterparts, and in Acero et al. (2013) and Landi et al. (2015), a multiwavelength approach has been adopted.

This paper contributes to the effort of exploiting such a unique all-sky gamma-ray survey in the search for a high-energy-emitting AGN population, with a new approach based on a total-band spectral energy distribution (SED) analysis.

The *blazar* non-thermal radiation dominates, and often hides, the emission from the host galaxy or from the AGN substructures. For most *blazar*s, especially for the BL Lac objects, this results in a featureless optical spectrum, thus hindering redshift measurement. Our tool for *blazar* recognition among the UGSs has then been tailored to offer at the same time a rough estimate of their redshift. This also takes advantage of the known relationship between the frequencies of the synchrotron and inverse Compton (IC) peaks and the source luminosities (sometimes referred to as the *blazar* sequence; Fossati et al. 1998; Ghisellini et al. 2017). In any case, our method is completely empirical, model-independent and not relying on prior assumptions, except for the requirement that the UGSs, proposed as *Fermi blazar* candidates, are detected in X-rays.

Note that in this paper, we propose a possible physical relationship between the UGS and the *blazar*-like object, to be considered as a candidate for the association. In our case, improving from a proposed association to an identification for the source would require, among others, spectroscopic follow-up and confirmation.

With the last *Fermi* catalogue released (3FGL; Acero et al. 2015), the number of UGSs wherein to exercise our *blazar* recognition tool will be further substantially amplified to as many as 1010 objects out of a total of 3034 sources, with chances to expand the number of gamma-ray-selected AGNs. While our UGS primary selection relies on the 2FGL catalogue, we make full use of the newer 3FGL to confirm those sources and to improve their error box and *Fermi* photometry.

This paper is organized as follows. In Section 2, we review the UGS selection. In Section 3 and Appendix A, we discuss our procedures for the counterpart selection of UGSs. In particular, Appendix A includes finding charts and the multiwavelength SED for the UGS counterparts. *We define as potential association of a UGS a set of sources consistently detected in various bands, all positionally coincident, and within the Fermi error box.* In Section 4, we build the library of multiwavelength SED templates from known *blazar*s, selected from the 3FGL catalogue. This SED template set is then used in Section 5 to build up our tool for the *blazar* recognition and characterization. In this section, the validity of the method is verified on bona fide *blazar*s, against known Galactic and extragalactic sources, and also the false-positive associations are tested. We then proceed in Section 6 to present the results of our proposed method for a set of UGSs, and defer to Section 7 some discussion and the conclusions.

Throughout this paper, we assume a standard *Wilkinson Microwave Anisotropy Probe* (*WMAP*) cosmology with $H_0 = 70\,\mathrm{km\,s^{-1}}$, $\Omega_\Lambda = 0.7$ and $\Omega_\mathrm{M} = 0.3$ (Spergel et al. 2007).

2 THE UGS SELECTION

For as many as 576 sources in the second *Fermi*-LAT catalogue, no plausible associations or identifications have yet been found. This makes an important component of the high-energy sky, and may hide new classes of AGNs, like the *extreme blazars* (Costamante et al. 2001; Bonnoli et al. 2015), the dark matter (DM) candidates (Belikov, Buckley & Hooper 2012; Zechlin & Horns 2012; Zechlin et al. 2012) or even unexpected high-energy phenomena.

To set up a procedure assisting the recognition of AGN populations among *Fermi* UGSs, we selected the UGS sample from the 2FGL catalogue following these basic selection criteria:

(i) No association in the 2FGL and no association in other gamma-ray catalogues (those from the EGRET and AGILE missions in particular), or catalogues at other wavelengths are considered by the *Fermi* collaboration.

(ii) Sky positions lie outside the Galactic plane, with a Galactic latitude $|b| > 20^\circ$. Many UGSs are in the Galactic plane, but we exclude this region because it is very crowded and confused, and the *Fermi* procedure hardly converges towards correct associations. Furthermore, this gives us a higher probability to select extragalactic sources.

An additional possible criterion is the variability index on the 2-yr baseline of the *Fermi* 2FGL observations. This might be used to select DM candidates among UGSs, because they are expected to be stable in time (Bertone, Hooper & Silk 2005). In any case, we do not consider flux variability in our primary UGS-selected sample, as most of them do not show significant flux variation.

A total of 183 UGSs from the 2FGL catalogue survive the selection criteria. While we referred to the 2FGL for our UGS selection at the time when the present project started, for all subsequent analyses, we used data from the 3FGL catalogue, yielding a decisive improvement in the *Fermi*/LAT source position uncertainty and photometry.

3 SEARCH FOR UGS MULTIWAVELENGTH COUNTERPARTS

In spite of the improvement allowed by the 3FGL, the association and identification of the *Fermi* sources is complicated, or even prevented, by the large *Fermi*-LAT error boxes of typically a few arcminutes radius (for a fraction of UGSs, this may even exceed ~10 arcmin). Our approach for finding potential counterparts for all of the 183 UGSs was to identify all detected X-ray sources inside the *Fermi* error box, and, if there are X-ray sources, then check for

the existence of counterparts at lower energies (radio, IR, optical) to build up a broad-band SED.

Following previous works in the literature (Stephen et al. 2010; Takahashi et al. 2012; Acero et al. 2013; Takeuchi et al. 2013; Landi et al. 2015), our UGS recognition procedure is primarily based on the available *Swift*/XRT X-ray imaging data on the *Fermi* source error-box position. Without a reliable X-ray counterpart, the method cannot be applied.

Not all gamma-ray sources have detectable X-ray counterparts inside their error box. This lack may be due to the intrinsic faintness of the source, X-ray flux variability, shallow depth of the X-ray exposure or the lack of X-ray observations of the field. Hints about the fraction of X-ray-emitting *blazars*, and among them of gamma-ray-emitting objects, can be derived from the BZCAT catalogue (Massaro et al. 2009). It represents an exhaustive, although by no means complete, list of sources classified as *blazars*, useful to look for general trends. The sample of 3561 *blazars* of the fifth BZCAT contains 63 per cent of objects detected in the soft X-ray band and 28 per cent of *Fermi*/LAT sources. Among the latter, 79 per cent are X-ray emitters. In conclusion, a large fraction of gamma-ray *blazars* contain an X-ray counterpart within the *Fermi*/LAT error box. We then expect that a substantial fraction of *Fermi* UGSs might be within the reach of our analysis, in consideration of the sensitivity and extensive coverage by the *Swift*/XRT telescope of the UGS sample. The counterparts found for the UGSs are proposed associations, to be subsequently verified once new gamma-ray catalogues are matched to other samples for the next releases.

Thanks to the X-ray positional uncertainties usually of the order of a few arcseconds, we typically have one to a few sources with multiwavelength photometric data inside the *Swift* source error box.

Subsequent to the X-ray detection, the radio band is important for our recognition work, since all discovered *blazars* have been identified as radio-loud sources so far.

Although primarily dedicated to the identification of gamma-ray bursts, the *Swift*/XRT telescope (Gehrels 2004), thanks to its rapid responsivity and high sensitivity, has been systematically used to obtain X-ray follow-up observations for most of UGSs (e.g. Falcone et al. 2011; Falcone, Stroh & Pryal 2014). So far, out of 183 UGSs selected, ∼130 have dedicated *Swift* observations. In our XRT analysis, we used only the PC mode[1] data. We analysed them through the UK Swift Science Data Centre XRT tool,[2] which provides X-ray images, source positions, spectra and light curves (Evans et al. 2009) of any object in the *Swift*/XRT field of view.

For our purposes, we used the total XRT 0.3–10 keV energy band to generate the X-ray image of the UGS sky field. The X-ray sky maps of our UGS sample are shown in the figures of Appendix A, and we checked which X-ray sources (*green circles*) fall inside the 3FGL 95 per cent confidence error box (*yellow ellipse*). For comparison, we also indicated with magenta ellipses the positional uncertainties of the 2FGL, with white crosses the X-ray sources of the Swift XRT Point Source Catalogue (1SXPS; Evans et al. 2014), and the radio sources of the NRAO VLA Sky Survey (NVSS) and Sydney University Molonglo Sky Survey (SUMSS) catalogues with cyan circles (with a radius equal to the semimajor axis of the positional error) or ellipses.

For each of the X-ray sources within the *Fermi* error box, we provided the position, with the corresponding error radius, and the X-ray spectrum. Two types of position determinations are available for the XRT sources: the *unenhanced* position, estimated using only a point spread function fit, and the *enhanced position* (Goad et al. 2007) where the absolute astrometry is corrected using field stars in the UVOT telescope and the systematic uncertainty is then decreased to 1.4 arcsec (90 per cent confidence), if compared to the 3.5 arcsec systematic for the *unenhanced* positions. The X-ray energy spectrum is estimated in the 0.3–10 keV band. The output spectra are downloaded and then fitted using the XSPEC software (version 12.8.1g; Arnaud 1996) of the HEASOFT FTOOL package. According to the number of total counts, the spectral data are analysed in different ways. If the source has less than 25 counts, the total flux is calculated by the mission count rate simulator WebPIMMS,[3] using a power-law model with photon spectral index 2. If the found X-ray counterpart is reported in the 1SXPS catalogue (Evans et al. 2014), we consider the corresponding photometric data points provided by the catalogue and available in the ASI-ASDC data base. With more than 25 total counts, we used an unbinned analysis by applying the Cash statistics. For bright sources with at least 150 counts, we binned (with the FTOOL *grppha*) the spectra with a minimum of 20 counts per spectral bin.

Once the list of the X-ray counterparts inside the *Fermi* error box is defined, our next step is to search for counterparts in radio, IR and optical bands, around their XRT *enhanced* position (or the *unenhanced* one if the former is not available), using a search radius corresponding to the 90 per cent confidence error radius (green circle, as exemplified in Fig. A1, upper panel). The results are displayed in the close-up images (i.e. Fig. A1, upper right-hand panel) where, on the XRT sky map, we superimpose entries from the radio NVSS (Condon et al. 1998) and SUMSS catalogues (Mauch et al. 2003), from the *WISE* (Wright et al. 2010; Cutri 2013) (blue crosses) and the 2MASS catalogues (Skrutskie et al. 2006) (green diamonds) in the near- and mid-IR bands, and finally from the USNO-B1.0 catalogue (Monet et al. 2003) or the Sloan Digital Sky Survey (SDSS) catalogue (Ahn et al. 2012, 2014) (magenta crosses) in the optical. The error on the optical and IR positions is neglected since it is several times smaller than the uncertainty on the X-ray position.

On the other hand, a spurious optical source may fall within the X-ray error box. Taking into consideration the number of objects and sky coverage in SDSS and USNO optical catalogues, the source sky density is ∼38 000 deg^{-2}; 2MASS and *WISE* have a lower source density. Then, the expected number of accidental optical sources in an error box of a typical radius from 2 to 5 arcsec (the minimum and maximum in our sample) spans from 0.03 to 0.2. Therefore, in our UGS sample of 14 objects, 5 of them with an error-box radius of 4 arcsec, we do expect up to approximately one spurious optical source in the X-ray error boxes. We note that in our sample there is no UGS with more than one optical source in the X-ray error box.

As a further check on the goodness of the XRT position estimates, we superimposed on the XRT image the positions of the X-ray sources from the 1SXPS reported by Evans et al. (2014). As can be seen in the sky maps of Appendix A, each XRT position found with our procedure is compatible with the 1SXPS positions.

The multiwavelength counterpart data set of a given UGS is then used to create the broad-band SEDs (Fig. A1, bottom panel). We combined these data through the SED Builder tool of the ASI ASDC

[1] Photon-counting (PC) mode: PC mode is the more traditional frame transfer operation of an X-ray CCD. It retains full imaging and spectroscopic resolution, but the time resolution is only 2.5 s. The instrument is operated in this mode only at very low fluxes (useful below 1 mCrab).

[2] http://www.swift.ac.uk/user_objects/

[3] http://heasarc.gsfc.nasa.gov/Tools/w3pimms.html

data base.[4] The *Fermi* flux points are taken from the 3FGL catalogue. All the X-ray-plotted data are corrected for Galactic absorption as available from the XSPEC package. If available, we include in the analysis also the X-ray data points reported by Takeuchi et al. (2013) (black points) and in the 1SXPS catalogue so that we can consider a cross-check of our analysis.

In Appendix A, we report details about our UGS counterpart search procedure for a sample of 14 *Fermi* UGSs among the 183 objects of our primary list.

4 DEFINITION OF A BLAZAR SED TEMPLATE SET

Since we are interested in recognizing *blazar* candidates among the *Fermi* UGS population, we built a tool for the systematic comparison of the broad-band SED of UGS counterparts with spectral templates representing various categories of the *blazar* populations. One possibility would be to use the so-called *blazar sequence* reported by Fossati et al. (1998) and Donato et al. (2001), and updated in Ghisellini et al. (2017), which is defined in terms of functional dependences of the spectral parameters for both the synchrotron and IC components. However, as explained in Section 4.2, we preferred to adopt a different, more empirical, approach.

4.1 A sample of known blazars

We defined a reference sample of known blazars, for which we collected all the available photometric data, grouping them into four categories defined in the *Fermi* 3LAC catalogue (the third catalogue of AGNs detected by the *Fermi*-LAT; Ackermann et al. 2015) and characterized by different spectral properties and luminosities: the low-synchrotron-peaked sources (LSPs, with synchrotron peak frequency $<10^{14}$ Hz), the intermediate-synchrotron-peaked sources (ISPs, with a synchrotron peak frequency between 10^{14} and 10^{15} Hz), the high-synchrotron-peaked sources (HSPs, peak frequency $>10^{15}$ Hz) and the extremely high peaked BL Lacs (EHBLs). The latter class (Costamante et al. 2001) is a new emerging population of BL Lac objects with extreme properties (a large ratio between the X-ray and the radio flux, and the hardness of the X-ray continuum locating the synchrotron peak in the medium–hard X-ray band).

In order to build a *blazar* SED template library, we started our selection from all *blazars* (FSRQs and BL Lac objects) present in the 3LAC catalogue at high Galactic latitude ($|b| > 20^{\circ}$), with a certain SED classification and a likelihood ratio reliability between radio/gamma bands and X-ray/gamma bands greater than 0. We cross-matched this preliminary selected sample with the BZCAT, and we rejected all objects without X-ray flux and with an uncertain or unknown redshift in the BZCAT. To ensure a good spectral coverage and a precise SED characterization, we performed a cross-match with the *WISE*, 2MASS and *Swift* (1SWXRT) catalogues. We use only the identified LSPs of the 3LAC. Finally, we performed an extensive search in literature to assess the robustness of the published redshifts, in addition to examining the published optical spectra, and we selected only the sources with secure redshift.

We also include the source PG 1553+113, having a very extensive multiband photometry but a still uncertain distance, for which we adopt a redshift of 0.5 following Danforth et al. (2010) and Prandini et al. (2010). PG 1553+113 is thought to be among the most distant HSP objects known and was considered as an extragalactic standard candle in the VHE band. Moreover, PG 1553+113 shows very moderate variability at all frequencies, which makes it a good candidate to build a robust average SED.

The final list of our adopted *blazar* templates is composed of 50 sources, including 20 LSPs, 12 ISPs, 16 HSPs and 2 EHBLs, and is reported in Table 1, where we indicate the source name, the 3LAC *blazar* SED class and the redshift from literature. We have considered this list of objects as sufficiently representative of the various *blazar* categories. Further enlarging this template data base would be possible and can be done in the future.

The ASI Science Data Centre Database and SED Builder tool have been used to collect the whole set of archived historical observations for every *blazar* of our sample. For each source, we created a data vector containing the monochromatic luminosities versus emission rest-frame frequencies, computed from the redshift of the object and standard expressions for the luminosity distance. *K*-corrections for all the photometric data have been computed assuming a flat frequency-independent spectrum in $\nu F(\nu)$. The data points range from the radio to the high-energy frequencies, and the complete list of the data catalogues used is reported in the ASI Science Data Centre SED Builder tool.[5]

Examples of SED data collected for four *blazars* are shown in Fig. 1.

4.2 Building the SED template set

Once the archive of multifrequency photometric data for all sample *blazar*s was collected, the next step was to fit these data with simple analytic representations for each object. We first divided the data in equally spaced frequency bins and calculated the average of the logarithms of the luminosity measurements inside each bin. This allowed us to minimize the effects of flux variability. Altogether, we obtained a library of 50 averaged *blazar* SEDs for the objects in Table 1.

For each of these sources, we fitted the average photometric data using a simply parametrized analytic form with a double power law with exponential convergence: one component representing the low-frequency synchrotron peak and the other representing the high-frequency IC peak. This function has the following expression:

$$\nu L(\nu) = \nu L_1(\nu) + \nu L_2(\nu), \tag{1}$$

with

$$\nu L_1(\nu) = A \left(\frac{\nu}{\nu_1}\right)^{1-\alpha} \exp\left\{-\frac{1}{2\sigma_1^2}\left[\log\left(1+\frac{\nu}{\nu_1}\right)\right]^2\right\},$$

$$\nu L_2(\nu) = B \left(\frac{\nu}{\nu_2}\right)^{1-\alpha} \exp\left\{-\frac{1}{2\sigma_2^2}\left[\log\left(1+\frac{\nu}{\nu_2}\right)\right]^2\right\}.$$

This has seven free parameters: A and B are the normalizations of the two emission components, α determines the slopes of the two power-law functions that are assumed to coincide (consistent both with the SSC assumption for the *blazar* modelling and with the data), ν_1 and ν_2 are the characteristic frequencies of the two emission bumps, and, finally, σ_1 and σ_2 determine the two bump widths.

[4] http://tools.asdc.asi.it/SED/

[5] http://tools.asdc.asi.it/SED/docs/SED_catalogs_reference.html

Table 1. The *blazars* used for our SED template library. The first column is the name of the *blazar*, the second column indicates the 3LAC *blazar* SED classification: LSP denotes the low-synchrotron-peaked sources, and ISP and HSP are the intermediate-synchrotron-peaked and high-synchrotron-peaked objects, respectively. The E-HBL is the emerging class of the extremely high peaked BL Lac objects (Costamante et al. 2001). In the third column is reported the redshift taken from literature.

Source name	3LAC SED class	Redshift
3C 279	LSP	0.536
3C 345	LSP	0.593
3C 454	LSP	0.859
4C +21.35	LSP	0.435
4C +28.07	LSP	1.213
4C +38.41	LSP	1.814
4C +49.22	LSP	0.334
AO 0235+164	LSP	0.94
CTA 102	LSP	1.037
OJ 287	LSP	0.306
PKS 0402−362	LSP	1.417
PKS 0420−01	LSP	0.916
PKS 0454−234	LSP	1.003
PKS 1502+106	LSP	1.839
PKS1510−08	LSP	0.36
PKS 2142−75	LSP	1.138
PKS 2144+092	LSP	1.113
PKS 2227−08	LSP	1.56
PMN J0017−0512	LSP	0.227
S4 1030+61	LSP	1.401
3C 371	ISP	0.046
4C +55.17	ISP	0.899
87GB 165604.4+601702	ISP	0.623
AP Librae	ISP	0.048
GB6 J0945+5757	ISP	0.229
NRAO 350	ISP	0.518
OS 562	ISP	0.751
PKS 0403−13	ISP	0.571
PKS 1004−217	ISP	0.33
PMN J0422−0643	ISP	0.242
SBS 1200+608	ISP	0.0653
W Comae	ISP	0.103
1ES 0414+009	HSP	0.287
1ES 0806+524	HSP	0.138
1H 0323+022	HSP	0.147
1RXS J023832.6−311658	HSP	0.232
Mrk 180	HSP	0.045
Mrk 501	HSP	0.034
Mrk 421	HSP	0.031
PG 1437+398	HSP	0.349
PKS 2005−489	HSP	0.071
RBS 0334	HSP	0.411
RBS 0958	HSP	0.138
RX J0847.1+1133	HSP	0.199
RX J1136.5+6737	HSP	0.136
TXS 1055+567	HSP	0.143
TXS 2106+030	HSP	0.149
PG 1553+113	HSP	0.5[a]
1ES 0229+200	EHBL	0.140
1ES 0347−121	EHBL	0.185

[a] The redshift of PG 1553+113 is not spectroscopic.

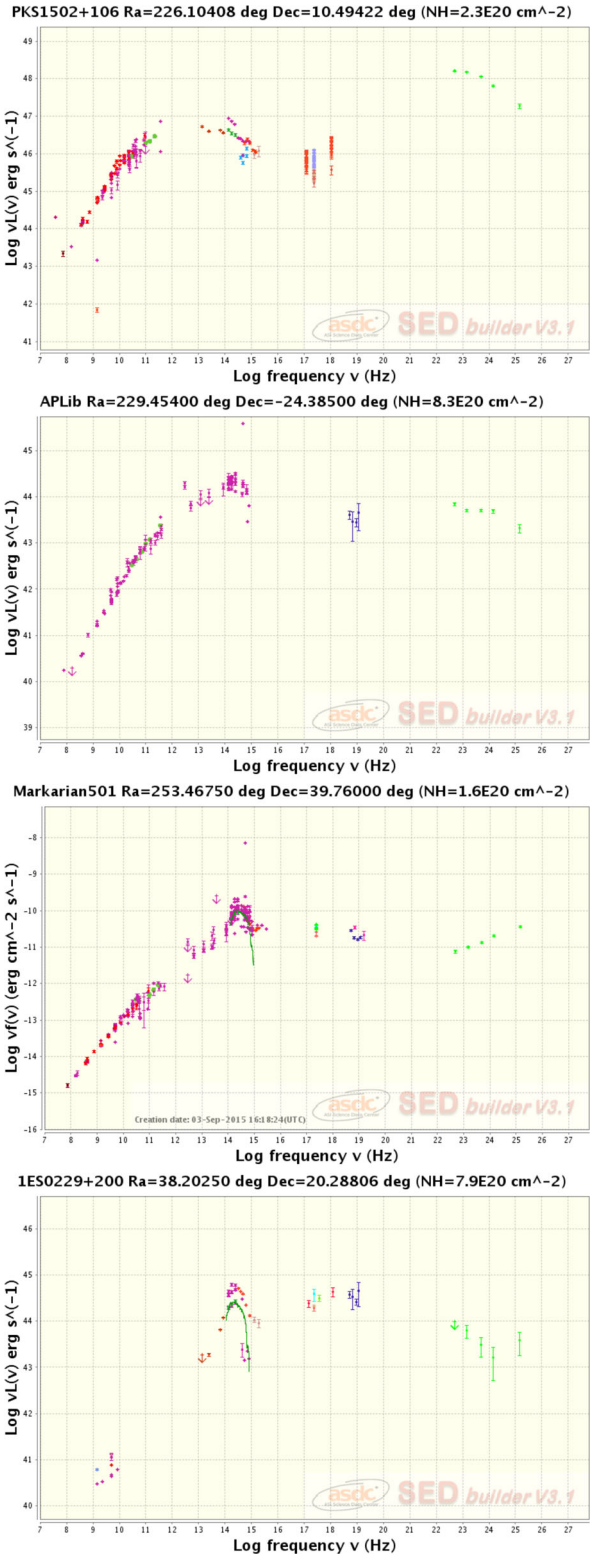

Figure 1. Examples of the SEDs of four *blazars* in our SED template library: PKS 1502+106 is an LSP *blazar*, ApLib is an ISP object, Markarian 501 is an HSP object and 1ES 0229+200 is an EHBL object. (The SEDs are expressed as νF_ν versus the frequency ν.)

Examples of resulting fitting curves for the average SEDs of the four representative *blazar*s are reported in Fig. 2, where the SED data are the geometric averages of the luminosity measurements inside each frequency bin. Note that two of the sources, the low-redshift Mrk 501 and 1ES 0229+200, show evidence for a narrow peak at $\log \nu \simeq 14$ to be attributed to the host galaxy, which is not fitted by our analytic formula. Indeed, the formula aims at reproducing only the non-thermal power-law *blazar* emissions. When comparing the SED templates to UGS SED data, we check a posteriori if a galactic contribution might show up (which essentially does not happen in most of our investigated cases that tend to be sources at high redshifts where the *blazar* emission dominates over the host galaxy).

We adopted this simple analytic representation for the average SEDs instead of using more physical models for *blazar* emission (like the SSC model itself), to be model-independent and to achieve good adherence to the data. In particular, SSC models have some difficulties to reproduce data in the radio band. Unlike the approach of Fossati et al. (1998), Donato et al. (2001) and Ghisellini et al. (2017), we did not average out the SEDs of the different sources.

We collect in Fig. 3 all the SED templates of our spectral library and grouped into the following four *blazar* classes: the LSP, ISP, HSP and E-HBL. The plot reveals the general behaviour found by Donato et al. (2001) and Ghisellini et al. (2017): The LSPs (red curves) occupy the highest luminosity values of the sequence, with the peak emission frequencies falling at lower energies with respect to those of HSPs (mainly BL Lac objects).

5 ASSOCIATING UGS WITH *BLAZAR* CLASSES

Once the broad-band spectral properties of the *blazar* populations are defined, we proceed to compare them with the SEDs of all our *Fermi* UGSs discussed in Section 3.

To this purpose, we developed an algorithm to assess the similarity of the UGS SED with those of *blazar*s of a given class, and to obtain some information on the *blazar* category and the redshift.

5.1 The algorithm

Our *blazar* recognition tool requires the following steps to be performed[6]:

(i) We start by considering the plots of luminosity versus frequency reported in Fig. 3 for all four *blazar* categories, including the SEDs of all sources in each category. The units in these plots are the logarithm of the $\nu L(\nu)$ luminosity in erg s^{-1} on the y-axis, and the logarithm of photon frequency ν in Hz on the x-axis.

(ii) Using the observed multiwavelength fluxes of a given UGS counterpart, we convert them into $\nu L(\nu)$ luminosities by assuming a suitable grid of redshifts z spanning a range of values from 0.05 to 2.0. Here again, we calculate the K corrections adopting flat spectra to be consistent with Section 4.1 for the template set. We then overplot the luminosity data points on the SED templates of all *blazar* classes, as illustrated in Fig. 5 and in the following.

[6] The numerical code for the *blazar* recognition is written in IDL and SUPERMONGO, for the ease of graphical comparison between the photometric data and the SED templates.

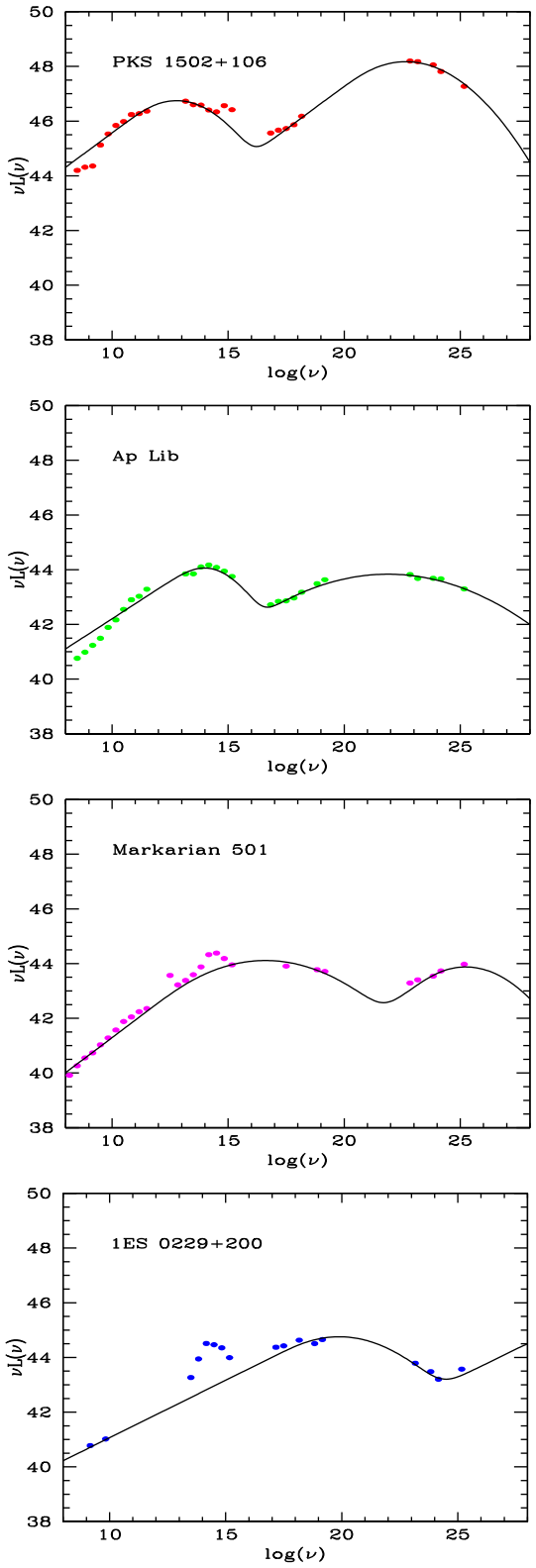

Figure 2. Examples of best fits for the multiwavelegth SED data points of the four *blazars* reported in Fig. 1. The fits are based on the analytic form in equation (1).

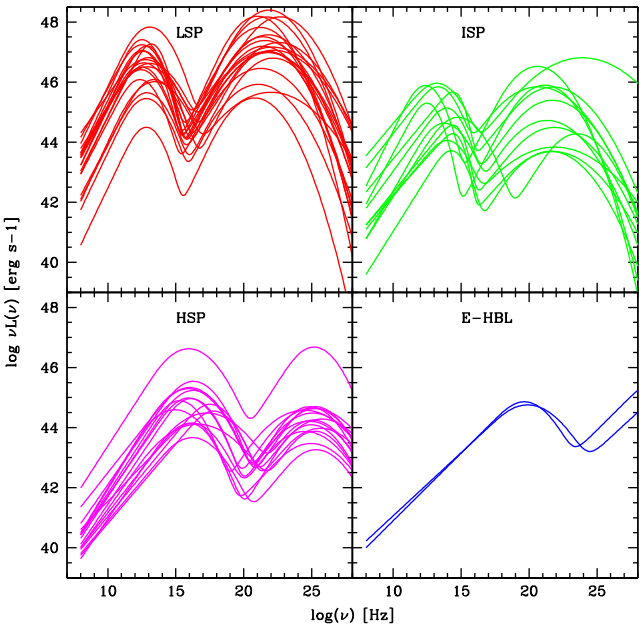

Figure 3. Analytic fits with a double power law and exponential convergence for the 50 average SEDs of the objects of our *blazar* library, categorized into the following four classes: LSP (red), ISP (green), HSP (magenta) and EHBL (blue).

(iii) For the same UGS counterpart, for every redshift of the grid and with respect to every *j*th SED of the *blazar* template set, the $\chi^2_{\rm min}$ statistic is calculated as the minimum of all values of

$$\chi^2_j = \sum_i \frac{\left\{\log\left[\nu_i L_i(\nu_i)\right] - \log\left[\nu_i l_j(\nu_i)\right]\right\}^2}{\left\{0.01\log\left[\nu_i l_j(\nu_i)\right]\right\}^2}. \quad (2)$$

The reduced $\chi^2_{\nu,j}$ is obtained by dividing by the number of data points. The minimum of this quantity, $\chi^2_{\nu,\rm min}$, offers a measure of how close is that *j*th SED template to the observational UGS SED for a given assumed redshift in the grid.

(iv) The second quantity that we use to estimate the similarity of the UGS SED with the *blazar* SED templates (and for a given assumed UGS's redshift in the grid) is the *minimum average distance* (MAD), defined as

$$\mathrm{MAD} = \frac{1}{N_{\rm SED}} \cdot |\sum_j (\chi_j)|, \quad (3)$$

with

$$\chi_j = \sum_i \frac{\log\left[\nu_i L_i(\nu_i)\right] - \log\left[\nu_i l_j(\nu_i)\right]}{0.01\log\left[\nu_i l_j(\nu_i)\right]},$$

where *i* is running over all photometric data points for that UGS, *j* is the index flagging every SED of the *blazar* template set and $\nu_i l_j(\nu_i)$ is the luminosity of the *j*th SED template interpolated at the frequency ν_i. The normalization factor $N_{\rm SED}$ is the number of templates of a given class of *blazars*. MAD is a measure of how far is the UGS SED, for a given assumed redshift of the grid, from the distribution of the SEDs of that *blazar* template category. Note that while $\chi^2_{\nu,\rm min}$ measures the match of data to a single template SED, MAD refers to the whole distribution of the SEDs in the *blazar* class and how far it is from the object data points.

(v) For a given UGS and its counterparts, the goodness of the recognition, the best-guess redshift and the spectral class are found by first considering the $\chi^2_{\nu,\rm min}$ statistics. In the cases in which we have more than one counterpart or when there are degeneracies in the χ^2 solutions as for the redshift, the MAD statistics are used to get a qualitative measure of the relative likelihood of these various solutions.

The MAD statistics measure the distance of the assumed UGS luminosity data points from the whole distribution of the SED templates. Consequently, it provides us a first hint about the *blazar* class and luminosity, and thus the source redshift by comparison with the observed fluxes. Instead, the $\chi^2_{\nu,\rm min}$ value is more closely related to the spectral shapes of both the UGS and the individual spectral templates and, in particular, to the slopes of the rising and descending parts of the two spectral components of the UGS SED. Hence, it evaluates the degree of similarity in shape of the SED of the UGSs and the *blazar* templates.

So, our *blazar* recognition procedure also offers a method of estimating a tentative redshift for the UGS, in cases where the agreement between the observational and template SEDs is good. We deem this a valuable contribution, considering the difficulty of measuring *blazar* redshifts and the number of objects for which it is unknown.

5.2 Characterizing the $\chi^2_{\rm min}$ and MAD statistics

The reduced $\chi^2_{\rm min}$ statistics have a well-defined χ^2 theoretical probability distribution under the assumptions of statistically independent data and Gaussian-distributed errors. Unfortunately, this is not our typical case because we are in the presence of flux variability and ill-defined photometric uncertainties. Consequently, we have adopted arbitrarily fixed errors for all data points (corresponding to 1 per cent of the luminosity value). In conclusion, we cannot simply use the χ^2 for testing our best-fitting solutions, nor do we have any statistics for our MAD test. We then proceeded to a rough characterization of the $\chi^2_{\nu,\rm min}$ and MAD statistics in the following way.

For the $\chi^2_{\nu,\rm min}$ test, we considered all *blazars* of the template set discussed in the previous section. For all these sources, we ignored their redshift and calculated the $\nu L(\nu)$ values by adopting redshifts within our grid of values of $z = 0.05$–2. Then, we calculated the values of $\chi^2_{\nu,\rm min}$ from equation (2) for all redshifts and all sources by comparing such estimated $\nu L(\nu)$ values with all best-fitting SEDs, excluding from the calculation the SED template of the source itself. The resulting values are reported as black histograms in Fig. 4 (top panel). The blue histogram, instead, represents the $\chi^2_{\nu,\rm min}$ distribution for the a priori known good solutions, which are the solutions for which the *blazar* class and redshift are consistent with the real source properties. (We considered a good solution if the found redshift value is within $\delta z/z \leq 0.1$ of the real redshift.)

So, the black histogram details the distribution of the $\chi^2_{\nu,\rm min}$ values that would be obtained from a blind application of the test to *blazar*s of unknown class and redshift. The fraction of random solutions with $\chi^2_{\nu,\rm min} \leq 1.1$ is 4 per cent, which can be considered as our approximate *confidence* figure. Note that we expect that the $\chi^2_{\nu,\rm min}$ test would obtain higher values on average when applied to *Fermi* objects other than *blazar*s. This indeed will be checked against non-blazar sources in Section 5.6. So the figure of 4 per cent can be considered as a conservative one. Our good solutions will be obtained for values of our $\chi^2_{\nu,\rm min}$ statistics, $\chi^2_{\nu,\rm min} \leq 1.1$.

We have performed a similar characterization of the MAD statistics, whose results are reported in the bottom panel of Fig. 4. Here, the black histogram is calculated from equation (3) for all sources in the template set, assuming that we do not know a priori the source

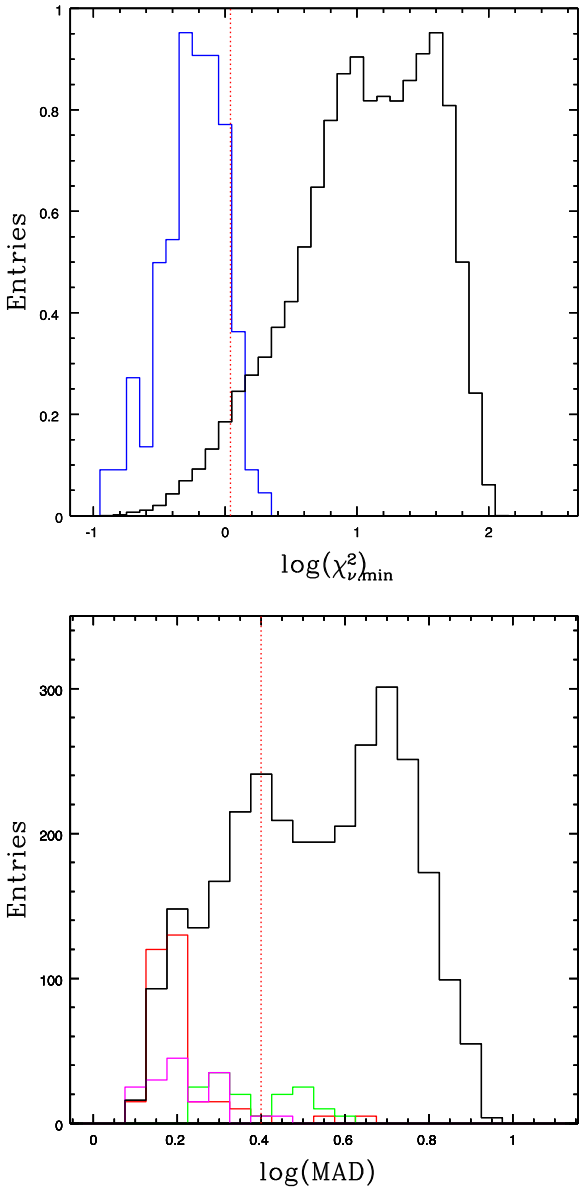

Figure 4. The top panel illustrates our test statistics for the $\chi^2_{\nu,\min}$. Black histogram: the distribution of the total $\chi^2_{\nu,\min}$ values calculated using the SED of each source of the sample used to build the template and assuming to ignore the real source redshift and the *blazar* class. The blue histogram are the good solutions, as discussed in Section 5.2. The vertical line marks our adopted *confidence* value for $\chi^2_{\nu,\min}$. The bottom panel illustrates a similar analysis performed for the MAD statistics. Coloured histograms refer to the MAD distribution of 'good' solutions for the four different classes of *blazar*s, with the same colour code as in Fig. 3: LSP (red), ISP (green) and HSPs (magenta). The vertical line marks our adopted *confidence* value for MAD. In this case, this value represents a guideline for good solutions.

redshift and class. The coloured histograms show the corresponding histograms for 'good' redshift solutions ($\delta z/z \leq 0.1$ of the real value) for the three main *blazar* classes. We see that the MAD test performs well in identifying good solutions for the LSP and HSP, and less well for the ISP, whose MAD distribution for the good solutions has substantial overlap with that of the random population. As a guideline, we will consider as potentially good *blazar* recognitions those with MAD < 2.5, however, without excluding solutions with higher MAD values. It is clear that, as anticipated, MAD offers a rather complementary test potentially useful for disentangling among degenerate solutions.

In all our later analyses, when applying our test to *Fermi* UGSs and other sources, we offer a graphical summary of the test performance in the form of plots of $\chi^2_{\nu,\min}$ versus MAD statistics for the four *blazar* classes and various redshifts (see e.g. Fig. 5). The quadrant at $\chi^2_{\nu,\min} < 1.1$ and MAD < 2.5 indicates regions where to look for potentially good solutions.

In general, our analysis can be effectively applied in cases in which there is a sufficient sampling of the synchrotron component of the *blazar* SED. This means having at least three reliable data points over the synchrotron part, and assuming that the *Fermi* and X-ray data are sufficient to sample the IC component.

5.3 Testing of the *blazar* recognition tool on known objects

As a sanity check and to test the effectiveness of our method in recognizing *blazar*-like sources among UGSs, we applied it on a few well-known *blazars*: 1ES 1215+303, 1ES 1011+496, 1ES 2344+514 and 3C 279 (which is also present in the sample used to build the SED templates). We have also made a test on the well-known high-redshift HSP 1ES 1424+240 with redshift $z = 0.604$ (Paiano et al. 2017). We assumed these to be sources with unknown class and redshift, and run blindly the algorithm on the simultaneous photometric data collected during dedicated campaigns for each *blazar*. Note that, to make it a meaningful test for the source 3C 279, we use here a different flux data set from that used for building the SED template set in Section 4.1: In that case, the whole set of historical observations in the ASDC archive was used, while here the test is done, instead, on completely independent sets of simultaneous observations, as detailed below for the five test sources.

Following the above-described recognition procedure, from the flux data of the five sources, we determined the corresponding luminosity values as a function of the redshift values of our grid. Then, the luminosity data were overplotted with different colours in the four panels for the *blazar* classes, as shown in Figs 5–9. The MAD and χ^2_ν statistics were computed for every redshift and every SED template. The results for the five well-known *blazar* sources are briefly discussed below.

(i) Results for 1ES 1215+303: This is an HSP *blazar* (Abdo et al. 2010) with redshift $z = 0.129$ (Paiano et al. 2017). For this source, we used the flux data collected during a multiwavelength campaign performed in 2011 (Aleksić et al. 2012) and triggered by an optical outburst of the source. The data were taken simultaneously from the radio to VHE band. The minima of the MAD and $\chi^2_{\nu,\min}$ statistics are reported in Fig. 5 and are used to select the best-fitting SED template. The minimum value of $\chi^2_{\nu,\min}$ is associated with an SED template of the HSP class (*green curve*), suggesting that 1ES 1215+303 is an HSP object with a redshift of about 0.1.

(ii) Results for 1ES 1011+496: For the test *blazar* 1ES 1011+496 at $z = 0.212$, we used the simultaneous multiwavelength data obtained by the observational campaign in 2012 (Aleksić et al. 2016). We constructed the diagnostic plots, shown in Fig. 6, with the corresponding table including the MAD and $\chi^2_{\nu,\min}$ values. The minimum $\chi^2_{\nu,\min}$ corresponds to the HSP class with a significant level of degeneracy. We found three best-fitting SED template candidates with the values of MAD and $\chi^2_{\nu,\min}$ in the *good solution* quadrant defined in Section 5.2. The first solution assumes for 1ES 1011+496 a redshift of $z = 0.1$, providing a $\chi^2_{\nu,\min} \sim 0.29$, while the second one, with $\chi^2_{\nu,\min} \sim 0.37$, corresponds to a redshift of 0.05.

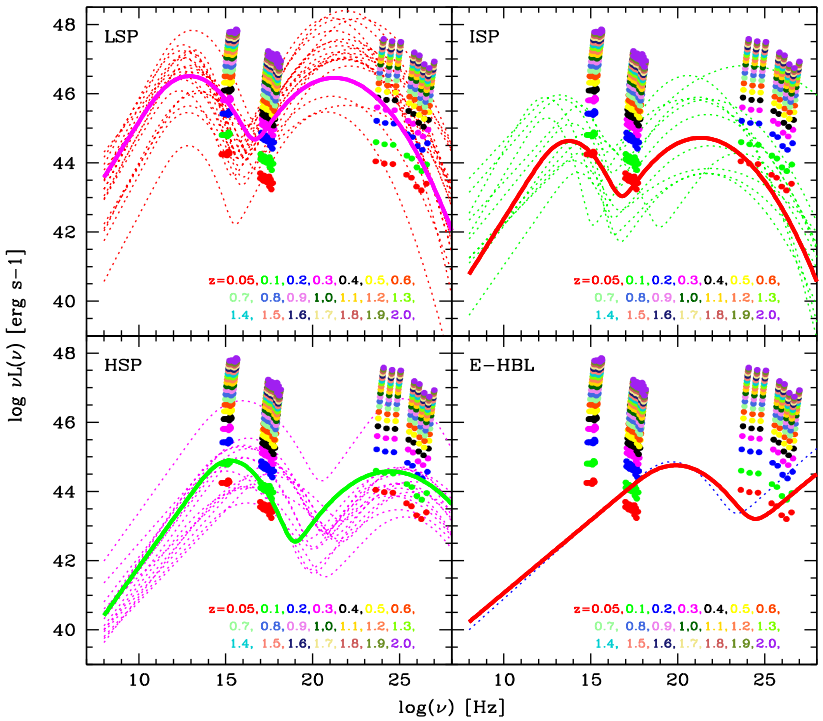

Class	$\chi^2_{\nu,min}$	MAD	z
LSP	0.44	1.73	0.2
ISP	0.37	1.79	0.05
HSP	**0.09**	**1.48**	**0.1**
EHBL	3.42	1.78	0.05

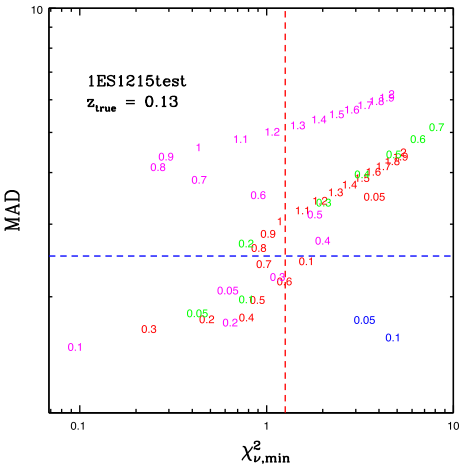

Figure 5. Spectral luminosity points of 1ES 1215+303 for different assumed redshifts (from 0.05 to 2.0), compared to our *blazar* SED template sets. The latter are built from archive data of known *blazars* for the four classes of LSP, ISP, HSP and EHBL. The coloured SEDs indicate the best-fitting redshift solutions for each class. The values of MAD and $\chi^2_{\rm min}$ in the table are referred to as the best-fitting SED template of each class (and shown as bold coloured lines). The plot on the right-hand side shows the values of MAD and $\chi^2_{\rm min}$ obtained by comparing photometric data for the source and the SED template set for different assumed redshifts. For 1ES 1215+303, our best-guess recognition is an HSP at $z \sim 0.1$ (*green line*).

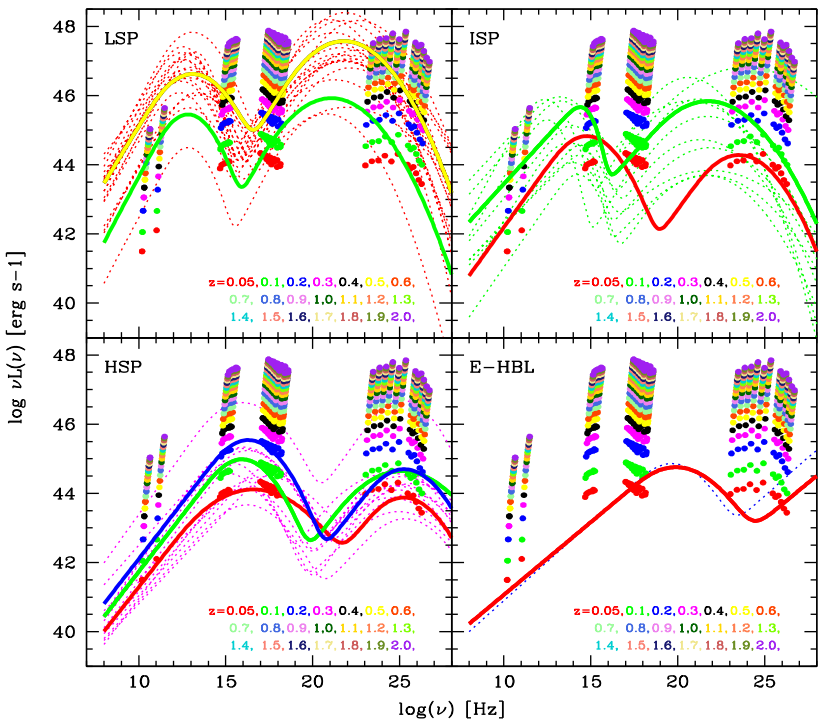

Class	$\chi^2_{\nu,min}$	MAD	z
LSP	2.32	2.50	0.1
LSP	2.78	2.23	0.5
ISP	2.35	2.61	0.1
ISP	2.14	2.63	0.05
HSP	**0.29**	**1.43**	**0.1**
HSP	0.37	1.42	0.05
HSP	0.77	2.23	0.2
EHBL	1.39	0.95	0.05

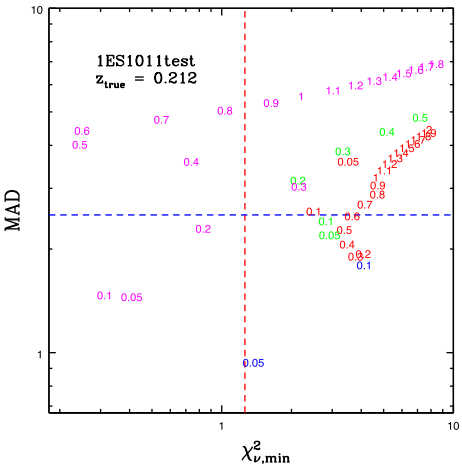

Figure 6. The same diagnostic plot as in Fig. 5 for 1ES 1011+496. Here, the best-guess recognition is an HSP at $z \sim 0.1$ (green line).

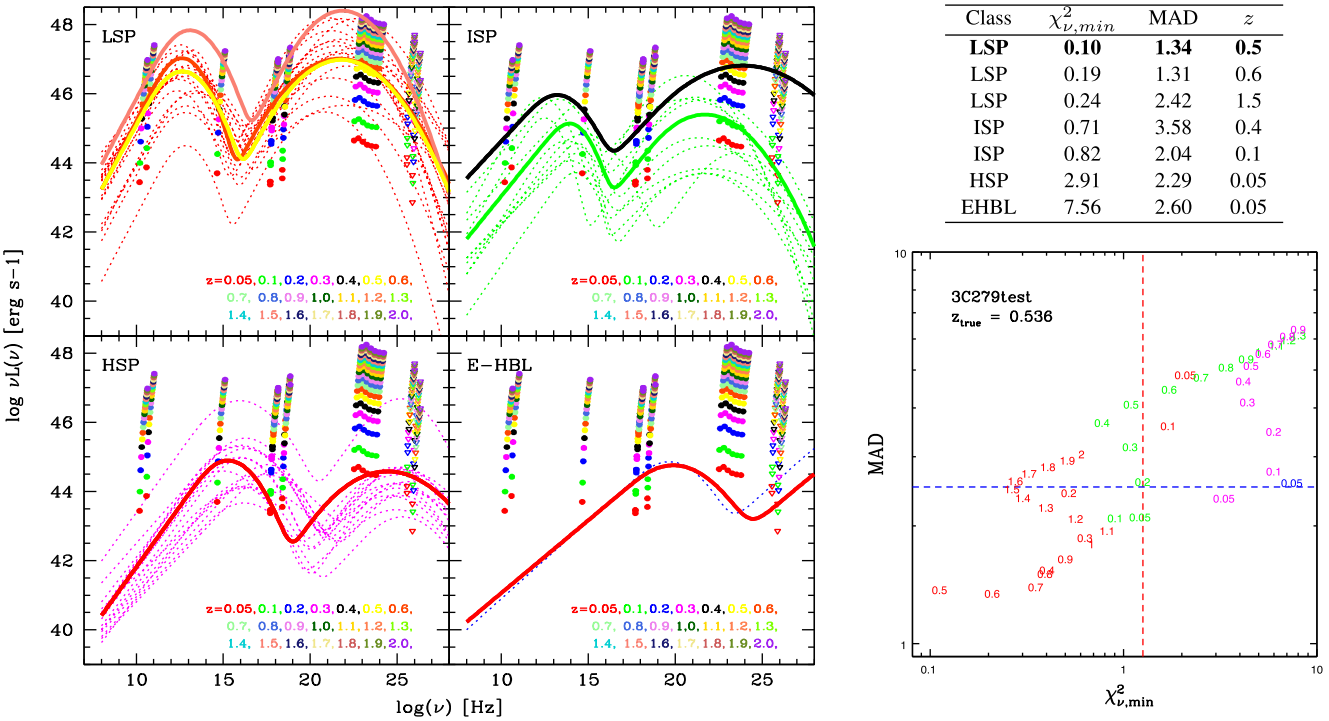

Class	$\chi^2_{\nu,min}$	MAD	z
LSP	**0.10**	**1.34**	**0.5**
LSP	0.19	1.31	0.6
LSP	0.24	2.42	1.5
ISP	0.71	3.58	0.4
ISP	0.82	2.04	0.1
HSP	2.91	2.29	0.05
EHBL	7.56	2.60	0.05

Figure 7. The same diagnostic plot as Fig. 5 for 3C 279. Here, the best-guess recognition is an LSP at $z \sim 0.5$ (yellow line).

The third solution provides a $\chi^2_{\nu,\rm min} \sim 0.77$, with a higher MAD value.

Even at this level of degeneracy, our tool is pretty much in agreement with the real *blazar* classification and the real redshift of $z = 0.212$ (Albert et al. 2007).

(iii) Results for 3C 279: This is another test *blazar* studied is 3C 279, the first LSP discovered to emit VHE gamma rays in 2006 (MAGIC Collaboration et al. 2008) and with a redshift of 0.536 (Hewitt & Burbidge 1993), making it one of most distant VHE-emitting sources discovered so far. The multiwavelength data, used in the *blazar* diagnostic plots, are taken from Aleksić et al. (2014a), obtained during the 2011 observational campaign performed from February 8 to April 11, when the source was in a low state. We see from Fig. 7 that we get an excellent match only for an LSP class and a redshift that is very consistent, within the uncertainties of our method, with the observed redshift. Such a good match with this well-known high-redshift source makes us confident about the validity of the test even for distant high-luminosity objects.

(iv) Results for 1ES 2344+514: This BL Lac object is classified as an HSP with a redshift of $z = 0.044$ (Perlman et al. 1996). It was targeted in 2008 by a simultaneous broad-band observational campaign from radio to VHE energies, during which this source was found in a low-flux state (Aleksić et al. 2013). We used these simultaneous multiwavelength data to test our *blazar* recognition tool. Concerning the HE gamma-ray flux, we decided to use the 1FGL catalogue flux points because we can consider them quasi-simultaneous with the data collected during the 2008 season. The diagnostic plots for this source are shown in Fig. 8 with the values of the MAD and $\chi^2_{\nu,\rm min}$ statistics. Our procedure indicates a good solution with an HSP at $z \simeq 0.2$, but few other solutions at lower redshift are within the confidence limits of $\chi^2_{\nu,\rm min}$ and MAD defined in Section 5.2. On one hand, for this source, our test fully confirms the classification as an HSP *blazar*, while, on the other hand, our test clearly indicates for it a low redshift, in spite of some degeneracy.

(v) Results for PKS 1424+240: The last *blazar* used as a test for our tool is the BL Lac object PKS 1424+240 belonging to the class of the HSPs. Recently, the redshift of the source, $z = 0.604$, was determined (Paiano et al. 2017), which makes it among the most distant TeV BL Lac objects. PKS 1424+240 was observed in the framework of a multiwavelength campaign during 2009 and 2010, allowing us to build a well-covered simultaneous broad-band SED from the radio to VHE regime (Aleksić et al. 2014b). The diagnostic plots, resulting from our *blazar* tool, are shown in Fig. 9. We found an excellent match with an HSP with $z \simeq 0.6$, assuming a very high luminosity, although a correspondingly bad value of MAD.

5.4 Test on non-blazar *Fermi* extragalactic sources

We have tested our method on extragalactic sources of the 3LAC catalogue that are classified as non-*blazars*. The results are summarized in Table 2. Double values correspond to multiple solutions with an acceptable fit.

The only type-1 Seyfert galaxy, Circinus, is clearly classified by our tool as a non-*blazar* object.

In the 3LAC catalogue, there are five steep spectrum radio quasars, but only two have a good X-ray coverage. For these, we find that the global SEDs are not evidently distinguishable from classical *blazars*.

We have considered 14 radio galaxies among the 16 present in the 3LAC catalogue (for the excluded sources, there is no X-ray coverage): All objects are rejected as *blazars* by our algorithm because of a global misfit, with the exception for PKS 0625−35, the only radio galaxy with an HSP SED reported in the 3LAC catalogue, and NGC 1218, which shows a marginal MAD value.

Finally, about the narrow-line Seyfert-1 galaxy (NLSG1) class, there are five objects reported in the 3LAC catalogue, and we analysed them with our recognition tool. Note that the most marginal

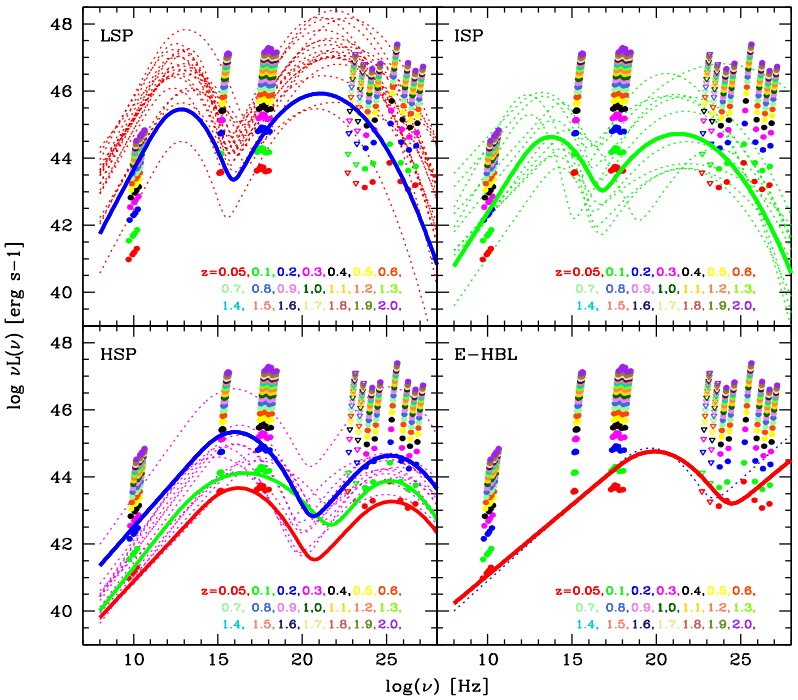

Class	$\chi^2_{\nu,min}$	MAD	z
LSP	3.61	2.49	0.3
ISP	2.39	2.29	0.1
ISP	2.79	2.35	0.2
HSP	**0.34**	**1.57**	**0.2**
HSP	**0.40**	**1.91**	**0.05**
HSP	0.44	1.37	0.1
EHBL	1.05	0.96	0.05

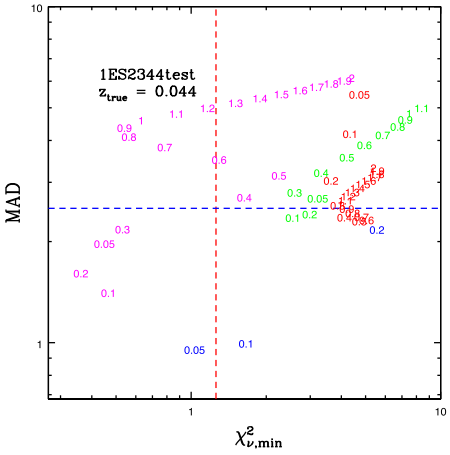

Figure 8. The same diagnostic plot as in Fig. 5 for 1ES 2344+514. Here, the best-guess recognition is an HSP at $z \sim 0.2$ (blue line).

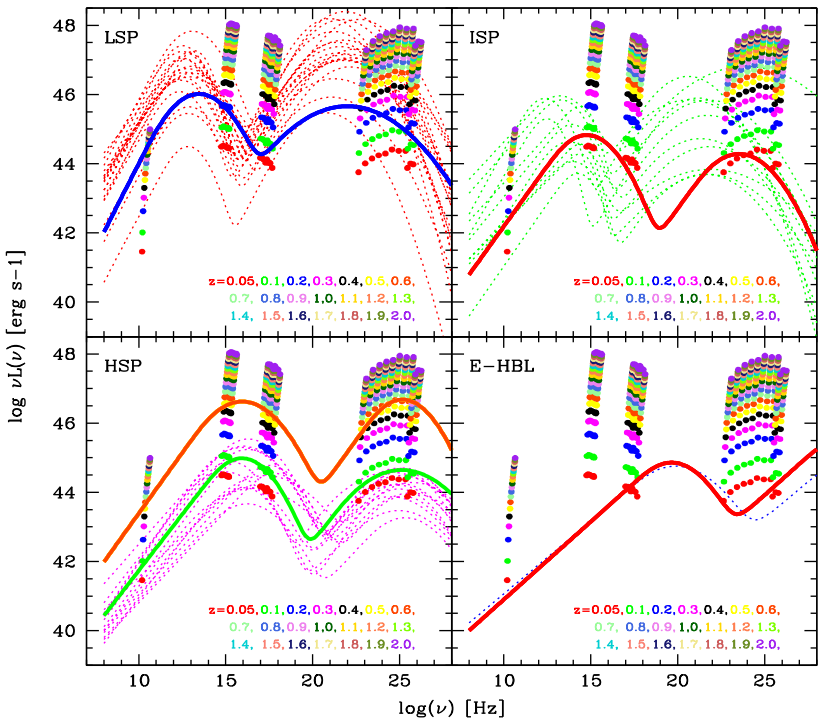

Class	$\chi^2_{\nu,min}$	MAD	z
LSP	2.29	2.06	0.2
ISP	0.91	2.01	0.05
HSP	**0.09**	**4.44**	**0.6**
HSP	0.21	1.56	0.1
EHBL	3.02	1.43	0.05

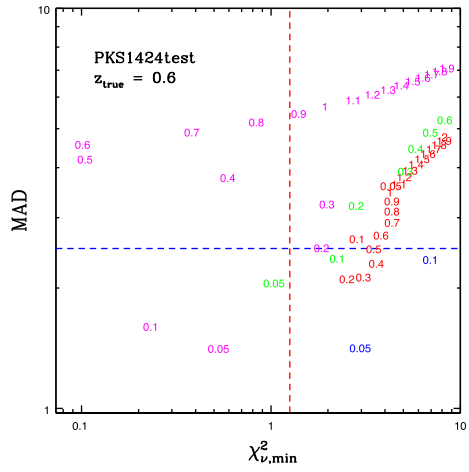

Figure 9. The same diagnostic plot as in Fig. 5 for 1ES 1424+240. Here, the best-guess recognition is an HSP at $z \sim 0.6$ (orange line).

source among these is 1H 0323+342, having a marginally acceptable $\chi^2_{\rm min}$. We classify this as an ISP with a consistent tentative redshift estimate by our method with respect to the correct one. All other four NLSG1s reveal fairly acceptable fits in our test as blazar objects. We do not consider in this paper the reason for this similarity between apparently different classes of sources, which will be discussed instead in a future paper.

5.5 A counter-example: 2FGL J1544.5−1126 (3FGL J1544.6−1125)

Our tool is also suited to exclude a *blazar* recognition: We consider, for example, the source 2FGL J1544.5−1126 in our UGS catalogue, a rather complicated case.

From the *Swift*/XRT observations of this UGS error box (see Fig. A9), we proposed the X-ray source 1RXS J154439.4−112820,

Table 2. Summary of the results of our test on non-*blazar* sources. Column 1: object name; column 2: 3FGL name; column 3: optical classification taken from 3LAC; column 4: 3FGL SED classification; column 5: redshift taken from NED; column 6: $\chi^2_{\rm min}$; column 7: MAD; column 8: tool classification proposed; and column 9: redshift proposed. We remark that the solutions with $\chi^2_{\rm min} > 1.1$ or MAD > 2.5 cannot be considered acceptable and the object is not recognized as a *blazar*-like source.

Name	3FGL name	Optical classification	3FGL SED class	Redshift	$\chi^2_{\rm min}$	MAD	AGN class proposed	Redshift proposed
Circinus galaxy	3FGL J1413.2−6518	sy	HSP	0.0015	6.62	3.22	LSP	0.1
3C 207	3FGL J0840.8+1315	ssrq	LSP	0.681	0.53	1.54	LSP	1.2
3C 380	3FGL J1829.6+4844	ssrq	LSP	0.695	0.91	1.81	LSP	0.7
PKS 2004−447	3FGL J2007.8−4429	nlsy1	LSP	0.24	0.28–0.26	1.83–2.34	ISP–ISP	0.4–0.7
PMN J0948+0022	3FGL J0948.8+0021	nlsy1	LSP	0.585	0.83–0.98	2.62–1.81	LSP–LSP	0.4–1.6
SBS 0846+513	3FGL J0849.9+5108	nlsy1	LSP	0.584	0.42–0.43	1.87–1.92	LSP–ISP	0.9–0.4
1H 0323+342	3FGL J0325.2+3410	nlsy1	HSP	0.061	1.08	2.11	ISP	0.1
PKS 1502+036	3FGL J1505.1+0326	nlsy1	LSP	0.409	0.40–0.45	1.95–1.78	LSP–ISP	0.9–0.4
NGC 1275	3FGL J0319.8+4130	rdg	LSP	0.0175	1.41	2.45	LSP	0.1
IC 310	3FGL J0316.6+4119	rdg	–	0.019	2.27	2.31	ISP	0.1
M 87	3FGL J1230.9+1224	rdg	–	0.0043	1.51	2.61	ISP	0.1
3C 303	3FGL J1442.6+5156	rdg	–	0.014	1.33	2.11	LSP	0.7
4C +39.12	3FGL J0334.2+3915	rdg	–	0.021	5.19	2.87	ISP	0.1
NGC 6251	3FGL J1630.6+8232	rdg	LSP	0.02	1.50	2.58	ISP	0.3
Pic A	3FGL J0519.2−4542	rdg	LSP	0.035	0.59	2.96	ISP	0.3
PKS 0625−35	3FGL J0627.0−3529	rdg	HSP	0.055	1.01	1.88	HSP	0.05
NGC 2484	3FGL J0758.7+3747	rdg	ISP	0.042	3.38	2.62	ISP	0.1
Cen B	3FGL J1346.6−6027	rdg	ISP	0.013	1.99	2.012	LSP	0.3
Cen A Core	3FGL J1325.4−4301	rdg	LSP	0.0018	2.59	2.09	LSP	0.3
3C 111	3FGL J0418.5+3813c	rdg	–	0.049	1.57	2.11	ISP	0.05
NGC 1218	3FGL J0308.6+0408	rdg	ISP	0.029	0.58	2.30	ISP	0.05
3C 264	3FGL J1145.1+1935	rdg	–	0.022	1.55	2.46	ISP	0.05

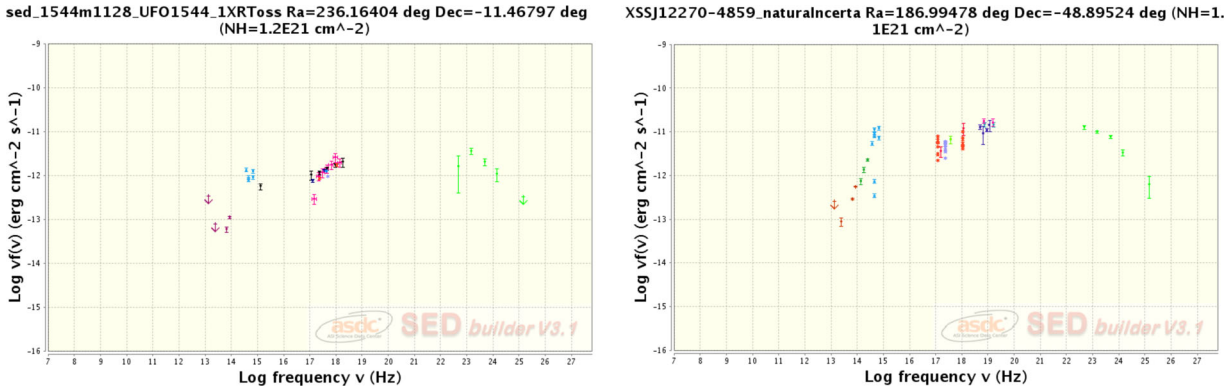

Figure 10. Comparison of the SEDs of 2FGL J1544.5−1126 and the low galactic latitude transitional millisecond pulsar binaries XSS J1227−4859 and 3FGL J1227.9−4854, two sources for which a galactic origin is suggested. The two SED behaviours appear virtually identical.

the brightest X-ray source in the field, as the likely X-ray counterpart of the *Fermi* source. This association is also proposed by Bogdanov & Halpern (2015), who identify 2FGL J1544.5−1126 as a transitional millisecond pulsar binary in an accretion state. They also note that the *Fermi* source 3FGL J1227.9−4854 (2FGL J1227.7−4853 in the 2FGL catalogue), associated with the transitional millisecond pulsar binaries XSS J12270−4859 (Bonnet-Bidaud et al. 2012), has a radio-to-gamma SED very similar to the 2FGL J1544.5−1126 SED, as illustrated in Fig. 10.

We applied our *blazar* recognition procedure (see Fig. 11), assuming 1RXS J154439.4−112820 as the most likely counterpart. From the $\chi^2_{\nu,\rm min}$–MAD plot, we note that actually no SED template can suitably match the observational data, independently of the assumed redshift (all $\chi^2_{\nu,\rm min}$ values are too high). Hence, our results suggest that a standard *blazar* classification for this source is quite unlikely.

The nature of the brighter X-ray source 1RXS J154439.4−112820 has been studied with optical spectroscopy by Masetti et al. (2013). These data show a Galactic source characterized by broad emission lines (Balmer series and helium transitions, EW $\sim$ 20 Å, FWHM $> 800\,{\rm km\,s^{-1}}$, where EW and FWHM are, respectively, equivalent width and full width at half-maximum).

5.6 Testing the rate of false-positive recognitions with known pulsars and other Galactic sources

We have further tested the validity of our *blazar* recognition tool against the observed SEDs of 15 Galactic sources of different HE

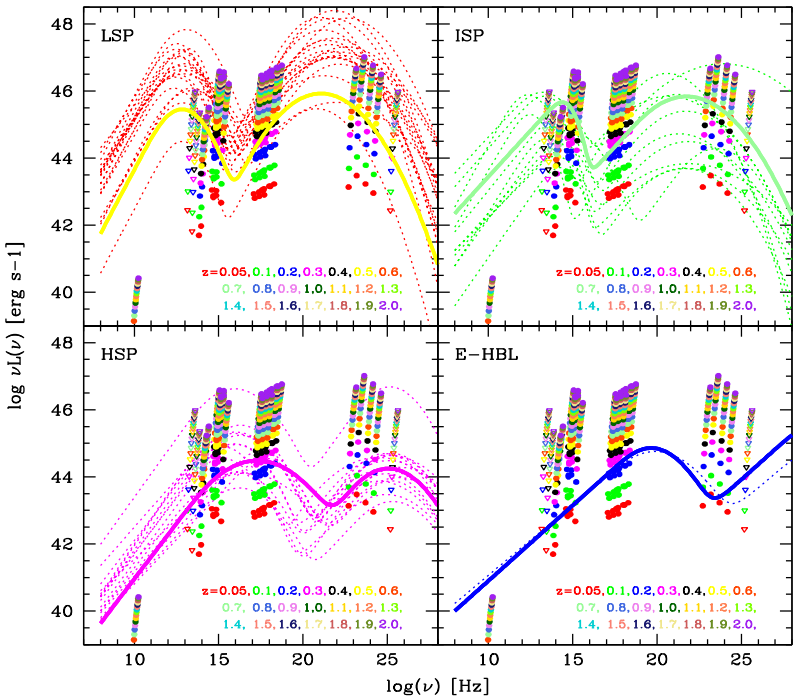

Class	$\chi^2_{\nu,min}$	MAD	z
LSP	7.22	2.58	0.5
ISP	7.19	3.17	0.7
HSP	2.70	1.85	0.3
EHBL	4.15	1.33	0.2

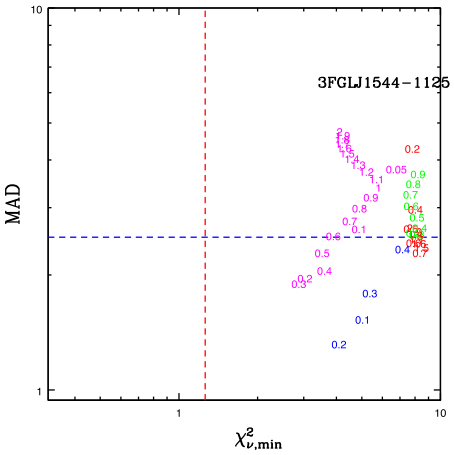

Figure 11. Spectral luminosity points of 2FGL J1544.5−1126 for different assumed redshifts (from 0.05 to 2.0), same as in Fig. 5. For 2FGL J1544.5−1126, there is no clear solution within our considered *blazar* categories.

classes included in the 3FGL catalogue, in order to verify the chance of false recognition. The objects have a spectral coverage similar to that of our *blazar* SED template set, and the multiwavelength fluxes are retrieved from the ASDC archive. The selected sample of Galactic objects includes the following:

(i) Seven pulsars detected in the *Fermi* surveys with good multiwavelength coverage and with a galactic latitude higher than 20°. They are PSR J0437−4715, PSR J0614−3329, PSR J1024−0719, PSR J1614−2230, PSR J2124−3358, plus the well-known Vela pulsar and the brightest HE millisecond pulsar PSR J2339−0533. We excluded the Geminga pulsar because of lack of sufficient spectral coverage.

(ii) The Crab Nebula, whose pulsar wind nebula is assumed to be the standard candle in high-energy astrophysics.

(iii) V407 Cyg, the only nova known in the 3FGL catalogue.

(iv) The HE binary Eta Carinae and the three high-mass binaries LS 5039, 1FGL J1018.6−5856 and LS I+61 303.

(v) The supernova remnants Cas A and SNR G349+002, also present in the 3FGL catalogue.

In Fig. 12, we report a graphical summary of the results obtained applying our method to 11 of the test Galactic sources. With no exception, these show high or very high values of $\chi^2_{\nu,\rm min} > 1$, and also typically large values for MAD. For the remaining four cases, the inferred values of $\chi^2_{\nu,\rm min}$ and MAD exceed our considered boundaries of 10 in both statistics, and therefore the algorithm plots are not shown. It is worth noting that for the pulsar PSR J2339−0533, our method would find acceptable fits for the LSP class at high redshift ($z = 1.1$–1.3). Indeed, we know that the source is located at 450 pc (Ray & et al 2015), such that our inferred radio luminosity ($\sim 10^{44}$ erg s^{-1}) from the best-fitting spectrum would imply an enormous continuum flux if located at that distance, which is excluded by the (unpublished) observational radio upper limits reported in Ray & et al (2015). A radio detection or an upper limit would immediately rule out a *blazar* classification for this source. This illustrates that the radio data may result in significant constraints on the UGS classification. In summary, our *blazar* recognition tool appears rather robust against misinterpreting pulsars and Galactic sources as AGNs.

6 UGS RECOGNITION RESULTS

We then proceeded to exploit our *blazar* recognition tool for the analysis of 14 *Fermi* UGSs of the 2FGL catalogue, whose multiwavelength counterparts have been previously defined and discussed. These make a subset of our complete, flux-limited UGS sample described in Section 2, for which we will discuss clear evidence in favour of a *blazar* recognition and provide a tentative estimate about the redshift. Results of our recognition procedure for them are detailed in the following sections.

6.1 2FGL J0102.2+0943 (3FGL J0102.1+0943)

The error-box area of this signal-to-noise ratio (S/N) = 7.09 *Fermi* detection was observed for a total of about 4 ks by *Swift*/XRT (details are reported in Appendix A). We found only one counterpart, for which we got data in the X-ray (*Swift*/XRT), optical (SDSS), IR (2MASS) and radio (NVSS) bands. The diagnostic plots obtained by our *blazar* recognition code, with the MAD and $\chi^2_{\nu,\rm min}$ values corresponding to the best-fitting SED templates, are reported in Fig. 13. The template with the minimum $\chi^2_{\nu,\rm min}$ corresponds to an HSP SED, for a best-fitting redshift of $z \sim 0.5$. An HSP blazar at about such redshift is our proposed classification for 2FGL J0102.2+0943.

6.2 2FGL J0116.6−6153 (3FGL J0116.3−6153)

This gamma-ray source is reported with a 9.9σ significance in the 3FGL. It was unassociated in the 2FGL catalogue, but in the

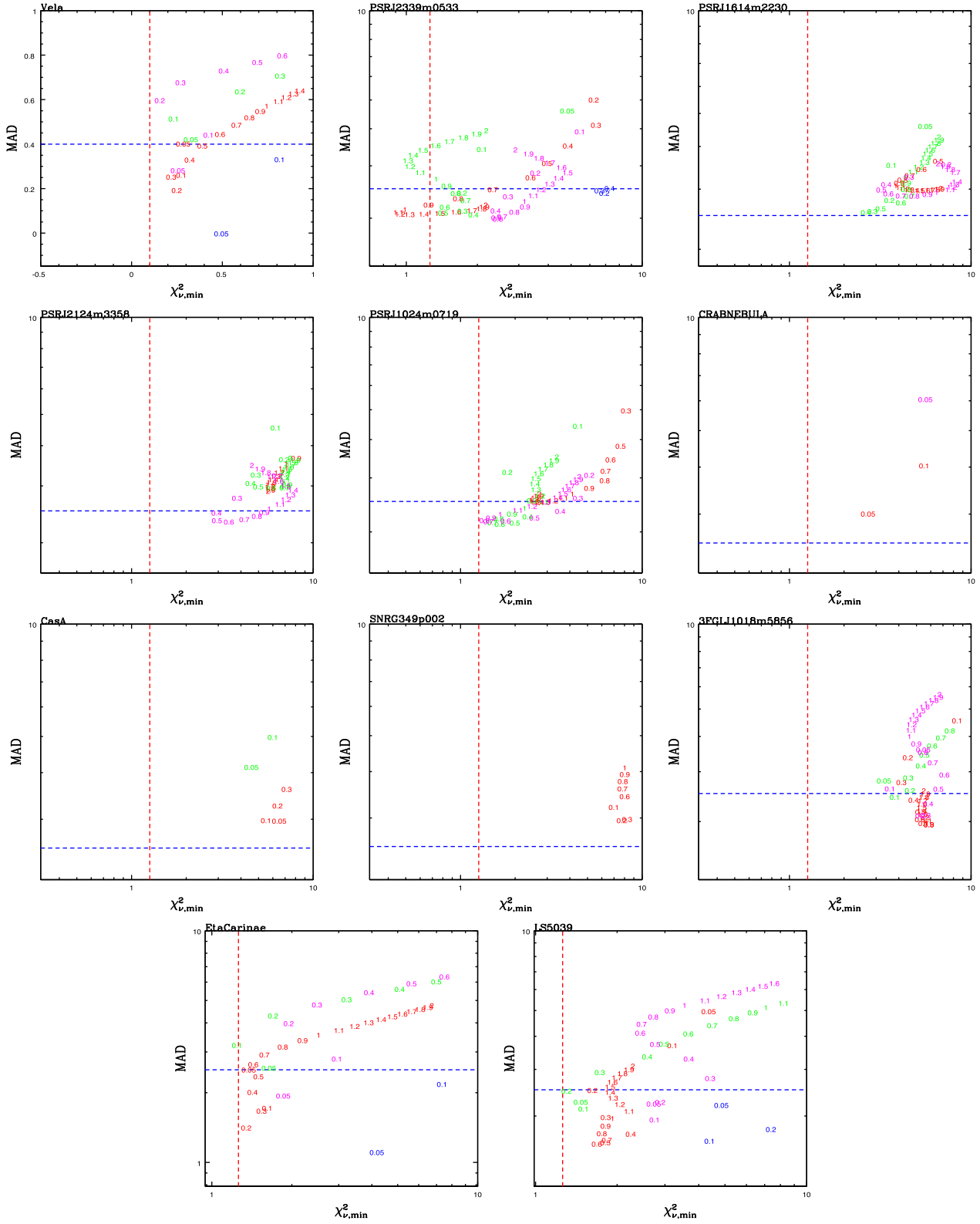

Figure 12. A graphical summary of the results of our *blazar* recognition method for Galactic sources. The plots show the values of MAD and $\chi^2_{\min}$ obtained by comparing photometric data for the sources and the SED template set for a wide range of redshifts. The high values of the statistics indicate these sources as non-*blazar*s.

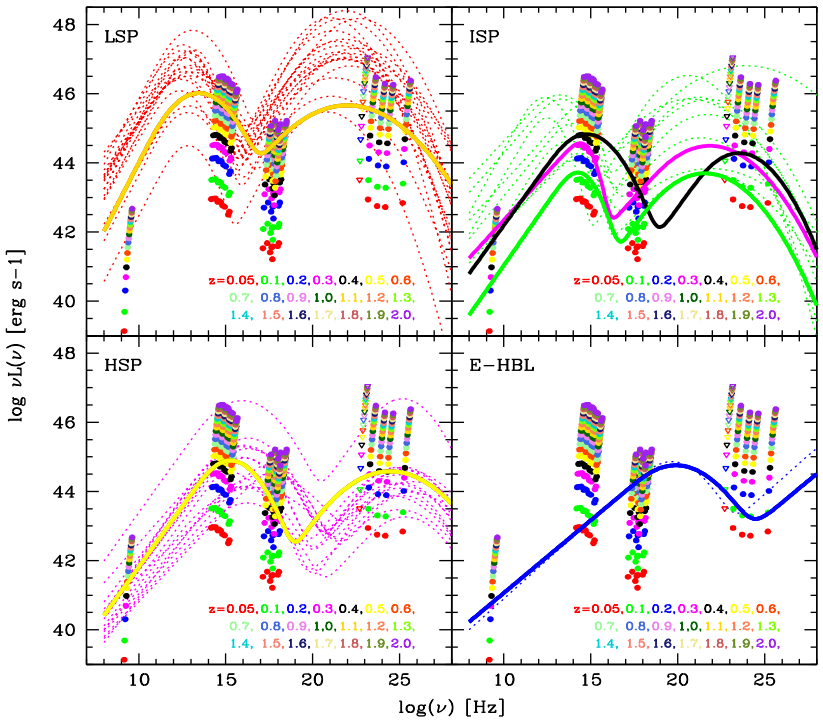

Class	$\chi^2_{\nu,min}$	MAD	z
LSP	0.88	2.29	1.1
ISP	0.64	3.33	0.1
ISP	0.71	1.96	0.3
ISP	0.78	1.92	0.4
HSP	**0.43**	**1.81**	**0.5**
EHBL	7.31	2.47	0.2

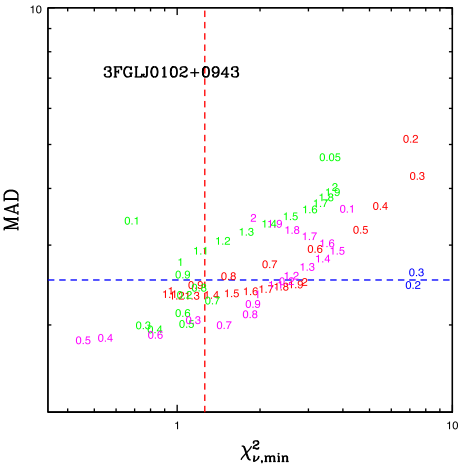

Figure 13. Spectral luminosity points of 2FGL J0102.2+0943 for different assumed redshifts (from 0.05 to 2.0), compared to the *blazar* SED templates. The latter are built from archive data of known *blazars* for the four classes: LSP, ISP, HSP and EHBL. The values of MAD and $\chi^2_{\nu,\rm min}$ reported in the table are referred to as the best-fitting SED template of each class (bold coloured line). The colour of the selected SED template refers to the best-fitting redshift indicated by our method. For 2FGL J0102.2+0943, the best-guess recognition is an HSP at $z \sim 0.5$ (yellow line).

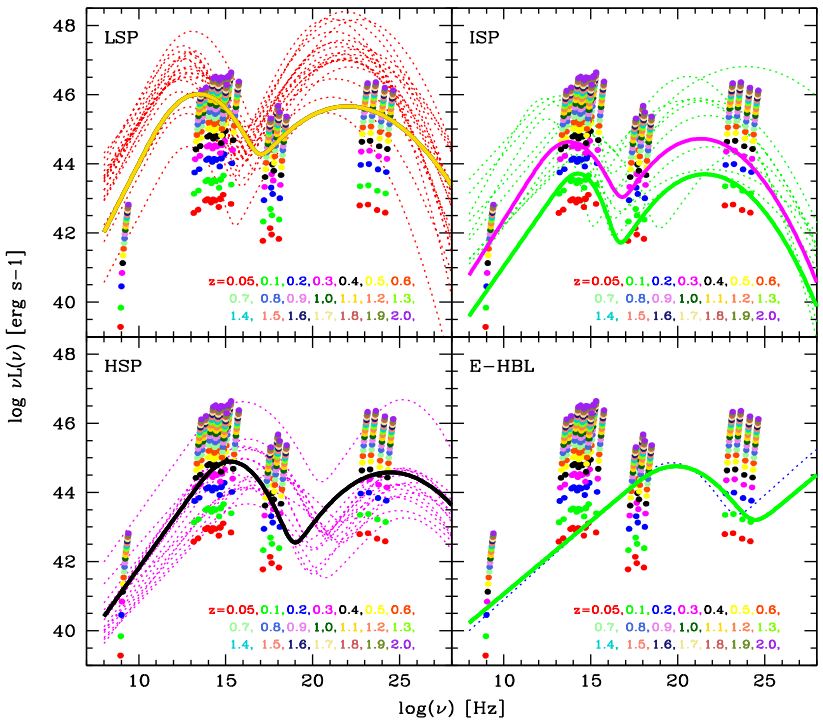

Class	$\chi^2_{\nu,min}$	MAD	z
LSP	0.67	2.11	1.1
ISP	0.33	3.08	0.1
ISP	0.41	1.78	0.3
HSP	**0.27**	**1.62**	**0.4**
EHBL	4.80	1.78	0.1

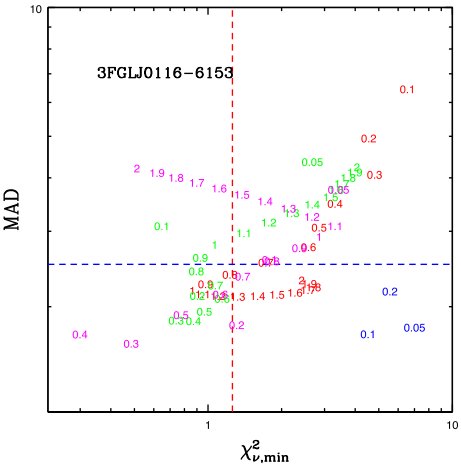

Figure 14. The same diagnostic plots as in Fig. 13 for the source 2FGL J0116.6−6153. The best-guess recognition is an HSP at $z \sim 0.4$ (black line).

3FGL and 3LAC catalogues, it is classified as an ISP BL Lac object with unknown redshift. In the 3.3 ks *Swift*/XRT image, we found only one X-ray source as a possible counterpart (Fig. A2). The broad-band SED, obtained by combining the multiwavelength fluxes of this counterpart, was analysed with our method, and the resulting plots are shown in Fig. 14. These indicate, as a best-guess classification, an HSP *blazar* with a tentative redshift of ∼0.4.

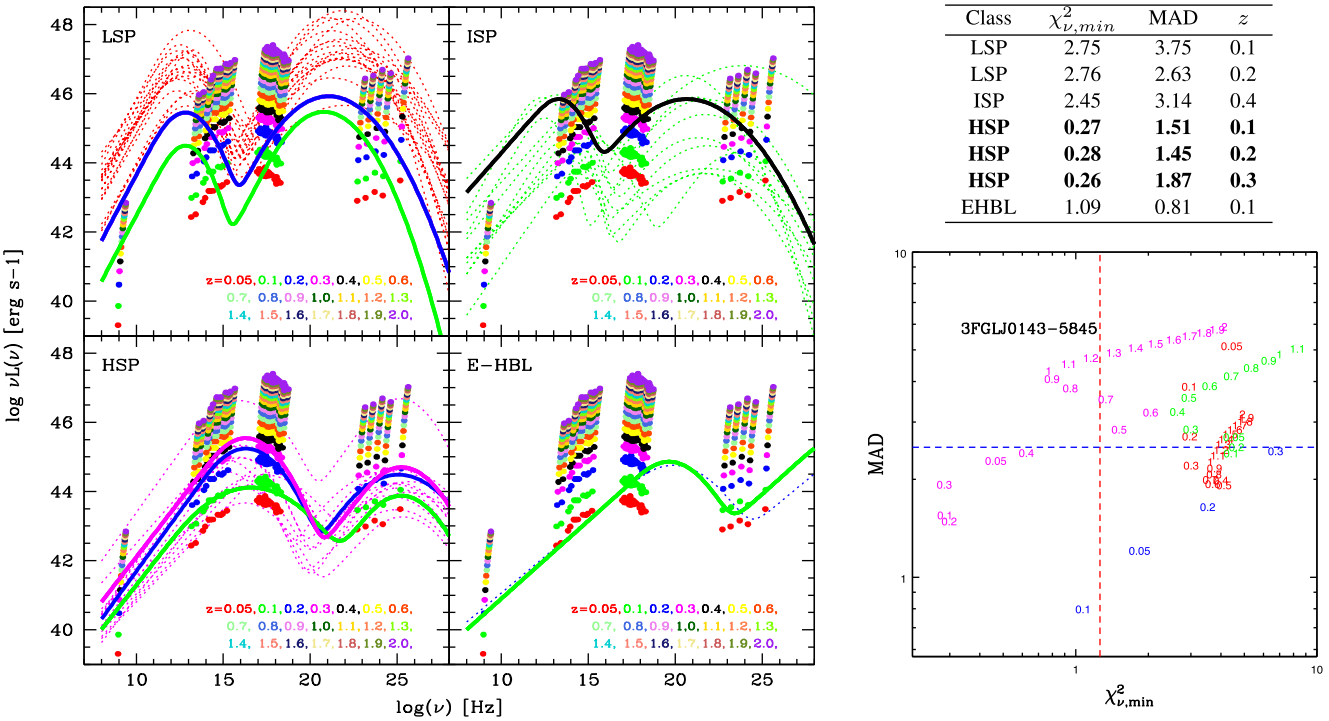

Class	$\chi^2_{\nu,min}$	MAD	z
LSP	2.75	3.75	0.1
LSP	2.76	2.63	0.2
ISP	2.45	3.14	0.4
HSP	**0.27**	**1.51**	**0.1**
HSP	**0.28**	**1.45**	**0.2**
HSP	**0.26**	**1.87**	**0.3**
EHBL	1.09	0.81	0.1

Figure 15. The same diagnostic plot as in Fig. 13 for the source 2FGL J0143.6−5844. Here, the best-guess recognition is an HSP at $z \sim 0.1$–0.3 (green, blue and magenta lines).

This result is in agreement with the association and the classification of the 3FGL catalogue and with the optical spectroscopic classification as a BL Lac object reported in Landoni et al. (2015) for the IR counterpart WISE J011619.62−615343.4. No spectroscopic redshift estimates are provided by them due to the lack of optical emission or absorption features in the optical spectrum.

6.3 2FGL J0143.6−5844 (3FGL J0143.7−5845)

This bright gamma-ray source is classified as a UGS in the 2FGL, but as a BL Lac object with unknown redshift in the 3FGL and 3LAC catalogues. The source was observed by *Swift*/XRT for about 4.5 ks. As discussed in Section A3, within the 3FGL *Fermi* error box, a very bright X-ray source has been found with multiwavelength counterparts, and the resulting multiwavelength SED (Fig. A3, bottom panel) presents a good spectral coverage. Our *blazar* recognition tool (Fig. 15) indicates clearly a minimum $\chi^2_{\rm min}$ corresponding to an HSP template that fits the source luminosity data assuming a redshift of 0.1–0.3. Our proposed *association* and classification is in agreement with the 3LAC classification and with the optical spectrum reported in Landoni et al. (2015), where the source is classified as a BL Lac object with unknown redshift for lack of optical features.

Since the source shows a hard *Fermi* spectrum[7] of $\Gamma < 1.84$ and is reported in the Second Fermi LAT Catalogue of high-energy sources (Ackermann et al. 2016, 2FHL catalogue), it could be an interesting target for TeV observations, once the EBL absorption is taken into account.

[7] According to the 3FGL catalogue, the hard-spectrum sources have a spectral index $\Gamma < 2.2$.

6.4 2FGL J0338.2+1306 (3FGL J0338.5+1303)

This source is reported in the 3FGL and 3LAC catalogues as a *blazar* candidate of uncertain type of the second subtype (BCU-II)[8] and with a detection significance of 11.90σ (in the 2FGL, it was classified as unassociated). The error-box field is analysed in Appendix A4, where only one candidate counterpart is found. The broad-band SED of this object is reported in Fig. A4, including the *Swift*/XRT imaging photometry. The output plots of our *blazar* recognition tool are shown in Fig. 16. We have two best-fitting solutions for the minimum $\chi^2_{\nu,\rm min}$ belonging to the HSP class with $z = 0.3$ and 1.9, the latter having a very large MAD value. For such a high redshift value, even the *Fermi* fluxes would be strongly damped because of the pair-production by the EBL (Franceschini et al. 2008): the last *Fermi* point at $\sim$e^{25} Hz by about a factor of 10, which is not seen in the data.

In conclusion, we consider the HSP solution with redshift $z \sim 0.3$ as our preferred solution, and it is worth noting that our proposal is confirmed by the recent work of Marchesini, Masetti & Chavushyan (2016), where the optical spectrum of the counterpart reveals a BL Lac object nature with an unknown redshift due to the lack of emission and absorption lines.

[8] The 3LAC sources classified as *blazar* candidates of uncertain type are categorized into three sub-types: the BCU-I sources where the counterpart has a published optical spectrum but is not sensitive enough for a classification as an FSRQ or a BL Lac; the BCU-II objects with the counterpart lacking an optical spectrum, but a reliable evaluation of the SED synchrotron-peak position is possible; the BCU-III sources for which the counterpart is lacking both an optical spectrum and an estimated synchrotron-peak position but shows *blazar*-like broad-band emission and a flat radio spectrum.

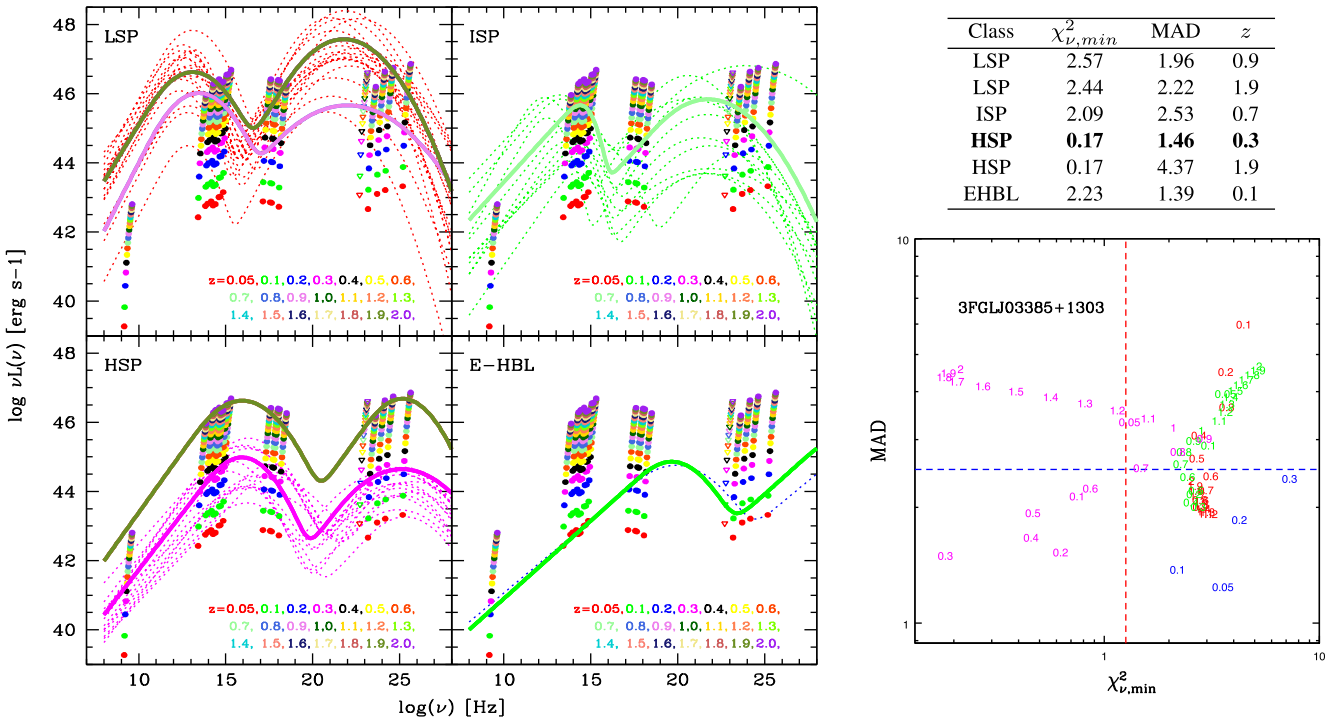

Class	$\chi^2_{\nu,min}$	MAD	z
LSP	2.57	1.96	0.9
LSP	2.44	2.22	1.9
ISP	2.09	2.53	0.7
HSP	**0.17**	**1.46**	**0.3**
HSP	0.17	4.37	1.9
EHBL	2.23	1.39	0.1

Figure 16. The same diagnostic plot as in Fig. 13 for the source 2FGL J0338.2+1306. Here, the best-guess recognition is an HSP at $z \sim 0.3$ (magenta line).

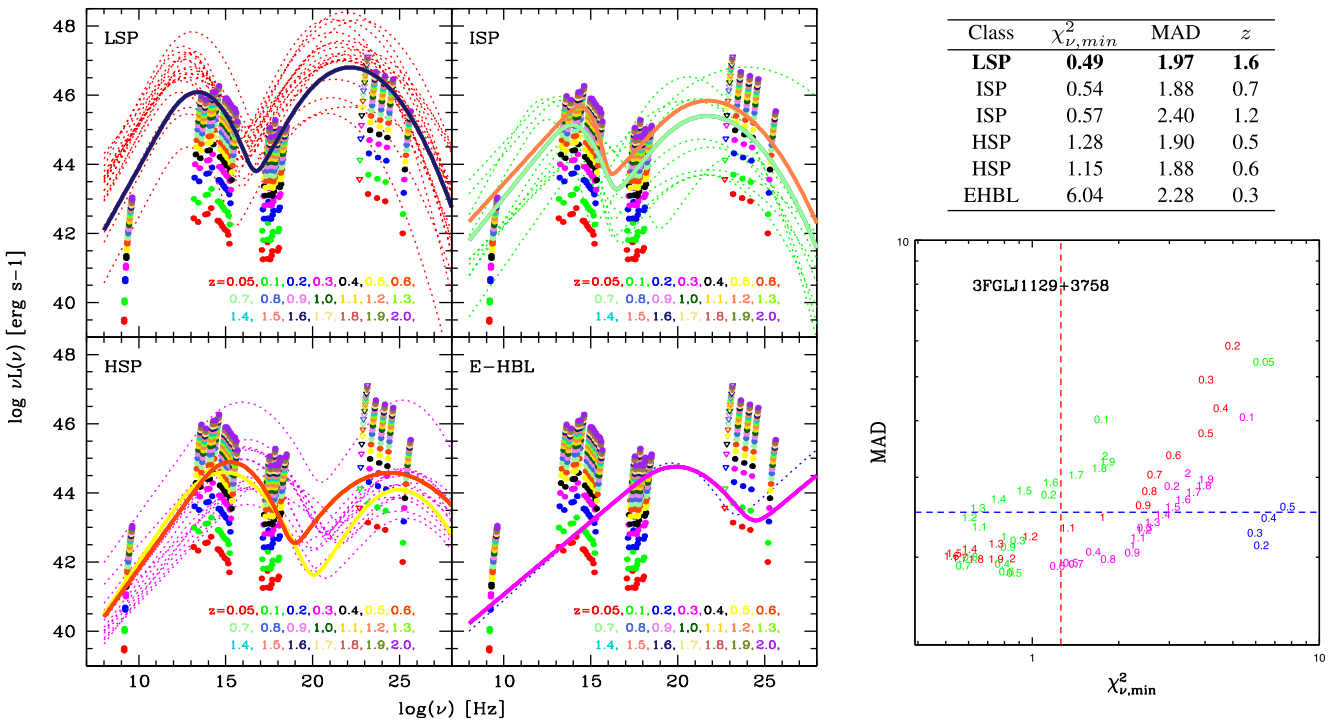

Class	$\chi^2_{\nu,min}$	MAD	z
LSP	**0.49**	**1.97**	**1.6**
ISP	0.54	1.88	0.7
ISP	0.57	2.40	1.2
HSP	1.28	1.90	0.5
HSP	1.15	1.88	0.6
EHBL	6.04	2.28	0.3

Figure 17. The same diagnostic plot as in Fig. 13 for the source 2FGL J1129.5+3758. Here, the best-guess recognition is an LSP at $z \sim 1.6$ (dark blue line).

6.5 2FGL J1129.5+3758 (3FGL J1129.0+3758)

The error-box area of this S/N = 10.25 gamma-ray emitter was observed for a total of about 4.7 ks by *Swift*/XRT, and the X-ray sky map is reported in Fig. A5. We proposed the object XRT J1129−375857 as the likely X-ray counterpart, and we were able to build its multifrequency SED spanning from the radio to HE band. Our *blazar*-like recognition code results in the diagnostic plots reported in Fig. 17, and the SED template with the minimum $\chi^2_{\nu,\min}$ corresponds to an LSP SED, for a best-fitting redshift of $z \sim 1.6$. However, we can see a significant degeneracy with other solutions belonging to the same class of LSP at $z \sim 1.2$–1.5 and to the ISP class at $z \sim 0.5$–1.2. In either case, a high value of the redshift is indicated.

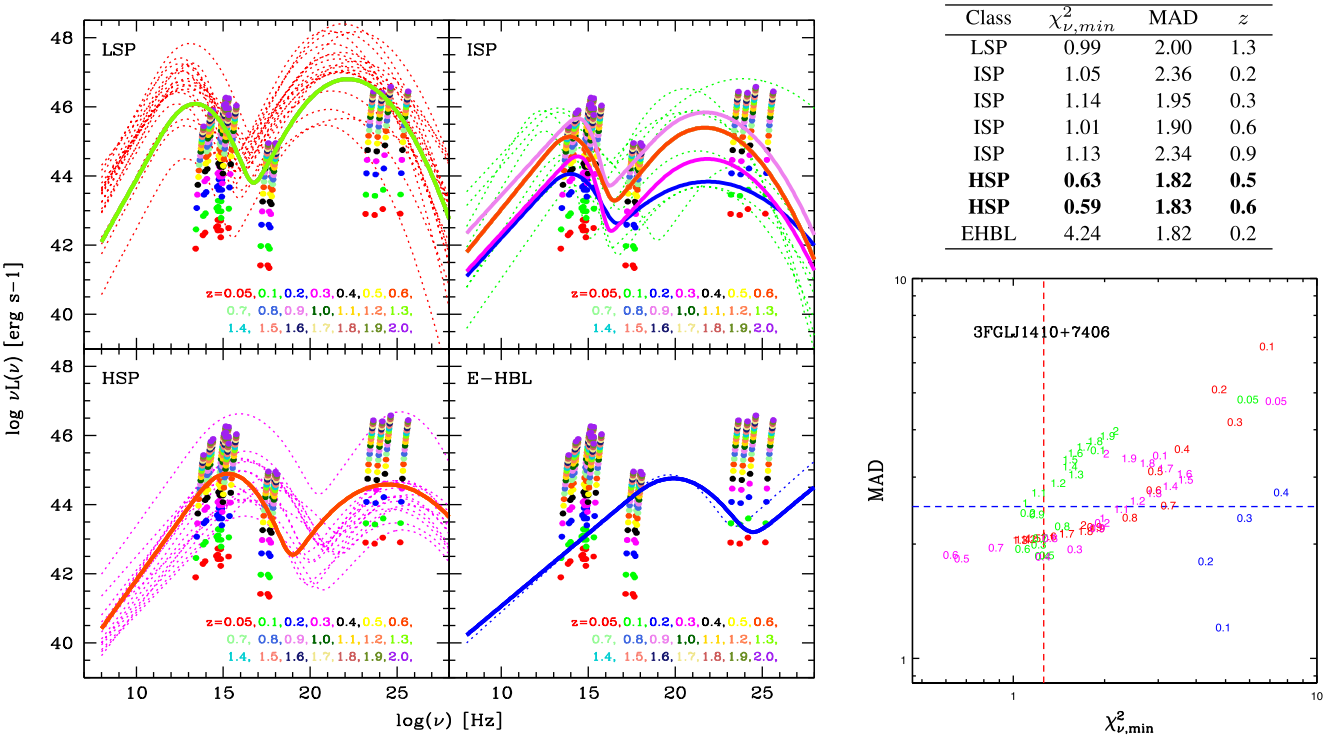

Class	$\chi^2_{\nu,min}$	MAD	z
LSP	0.99	2.00	1.3
ISP	1.05	2.36	0.2
ISP	1.14	1.95	0.3
ISP	1.01	1.90	0.6
ISP	1.13	2.34	0.9
HSP	**0.63**	**1.82**	**0.5**
HSP	**0.59**	**1.83**	**0.6**
EHBL	4.24	1.82	0.2

Figure 18. The same diagnostic plot as in Fig. 13 for the source XRT J141045+740509. Here, the best-guess recognition is an HSP at $z \sim 0.5$–0.6 (yellow and orange lines that result in overlapping).

6.6 2FGL J1410.4+7411 (3FGL J1410.9+7406)

Thanks to the new reduced 3FGL error box of this *Fermi* UGS, we can find an X-ray source that can be proposed as a likely counterpart for the source (see the details in Appendix A6). Despite the lack of a radio counterpart, which could help the tool to constrain the classification and the redshift for this object, we have a good spectral coverage at the other frequencies and we can build a multiwavelength SED for the counterpart XRT J141045+740509. Based on our *blazar*-like SED recognition tool (Fig. 18), we suggest that the nature of 2FGL J1410.4+7411 is an HSP object with a high tentative redshift of $z = 0.5$–0.6. An optical classification of our proposed counterpart is provided by Marchesini et al. (2016). The optical spectrum shows emission lines, allowing us to classify the source as a new NLSY1 with $z = 0.429$.

6.7 2FGL J1502.1+5548 (3FGL J1502.2+5553)

The source is still a UGS in the 3FGL catalogue with a detection significance of 12.6σ. In the 3FGL error-box region of the source, the only X-ray source found is 1SXPS J150229.0+555204, which is spatially coincident with a radio source. We propose it as the likely X-ray counterpart for 2FGL J1502.1+5548 (the broad-band SED and details in Appendix A7). The resulting plots by our *blazar* SED-recognition tool are shown in Fig. 19. The best-fitting SED template, with minimum $\chi^2_{\nu,\rm min}$, belongs to the LSP class at redshift $\sim$1.6–1.9, but a similarly good solution is found with a template of the ISP class at lower redshift ($z \sim 0.4$–0.7). Hence, for this source, the *blazar* classification and redshift are uncertain (but a high redshift is indicated), probably due to the limited spectral coverage of the synchrotron peak for this source. Photon–photon absorption by the EBL is not expected to seriously affect the *Fermi* fluxes even for the high-redshift solution.

6.8 2FGL J1511.8−0513 (3FGL J1511.8−0513)

This object is present in the 3FGL and 3LAC catalogues with a significance of 10.59σ, and its new classification is a *blazar* candidate of uncertain type with unknown redshift. Two X-ray sources are found in the source region observed by *Swift*-XRT (Appendix A8), but only the brightest, XRT J151148−051348, is in the reduced 3FGL error ellipse and also proposed as counterpart in the *Fermi* catalogue. The diagnostic plots for the X-ray counterpart are shown in Fig. 20, and the best-fitting SED template corresponds to an HSP with a tentative redshift $z = 0.1$–0.2. Our classification is in agreement with the result reported in Álvarez Crespo et al. (2016), where the source is classified as a BL Lac object with unknown redshift, on the basis of its featureless optical spectrum.

6.9 2FGL J1614.8+4703 (3FGL J1615.8+4712)

The multiwavelength counterpart set for this source is discussed in Appendix A10, and we propose the *Swift* source XRT J161541+471110 as the likely X-ray counterpart, in agreement with the association reported in the 3FGL and 3LAC catalogues. In Fig. A10, we show its multiwavelength SED built from its counterpart set. Based on our *blazar* recognition tool (Fig. 21) and on the minimum value of $\chi^2_{\rm min}$, we suggest that 2FGL J1614.8+4703 is an ISP object at redshift $z = 0.3$. For this object, the SDSS survey has reported the presence of an early-type spiral (Sa) (A10) in the position of our optical counterpart, with a measured spectroscopic

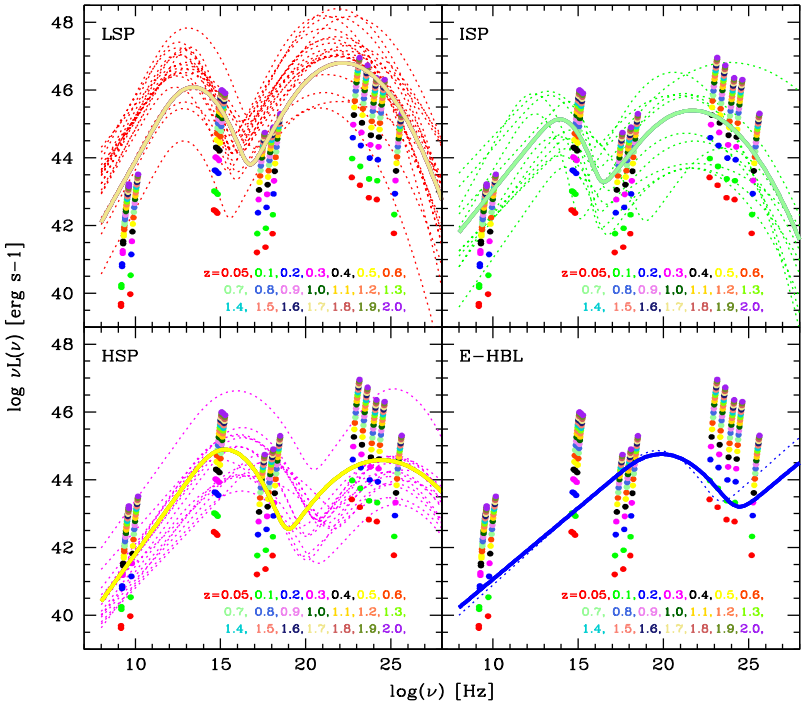

Class	$\chi^2_{\nu,min}$	MAD	z
LSP	**0.61**	**2.20**	**1.7**
ISP	0.75	2.08	0.7
HSP	1.59	2.04	0.5
EHBL	4.29	1.80	0.2

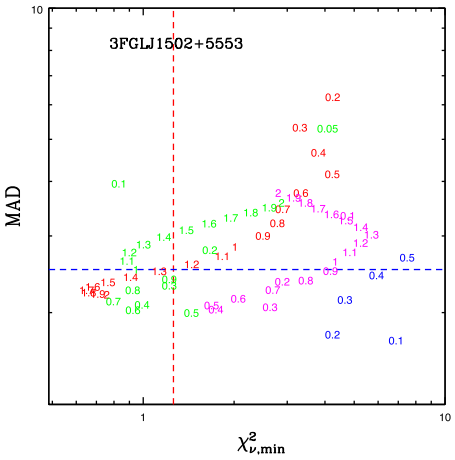

Figure 19. The same diagnostic plot as in Fig. 13 for the source 1SXPS J150229.0+555204. Here, the best-guess recognition is an LSP at $z \sim 1.7$ (beige line).

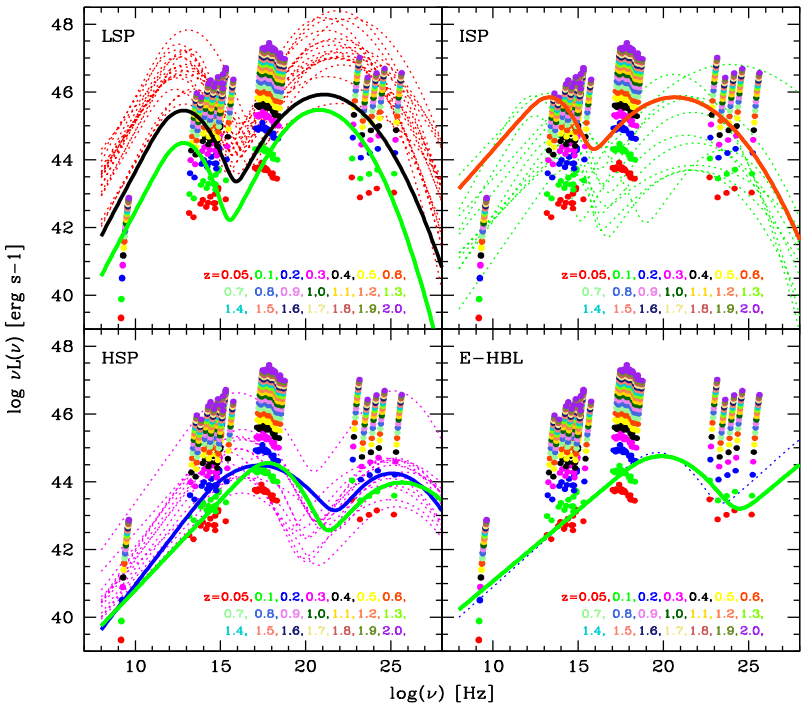

Class	$\chi^2_{\nu,min}$	MAD	z
LSP	3.40	4.76	0.1
LSP	3.47	2.49	0.4
ISP	3.85	3.10	0.6
HSP	**0.60**	**1.86**	**0.1**
HSP	**0.68**	**1.55**	**0.2**
EHBL	0.90	0.80	0.1

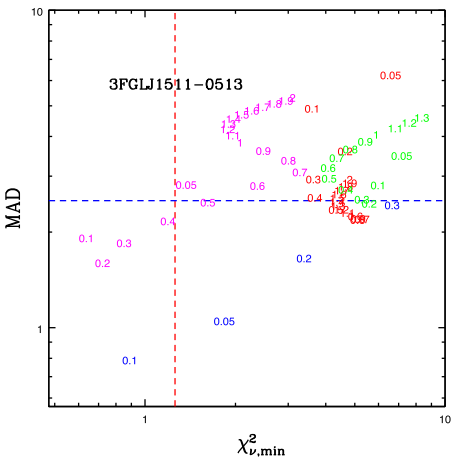

Figure 20. The same diagnostic plot of Fig. 13 for the source XRT J151148−051348, the X-ray counterpart candidate for 2FGL J1511.8−0513 for different assumed redshifts (from 0.05 to 2.0). Here, the best-guess recognition is an HSP at $z \sim 0.1$–0.2 (green and blue lines, respectively).

redshift of $z = 0.19$, which may represent the host galaxy of a very faint low-z *blazar*.

6.10 2FGL J1704.3+1235 (3FGL J1704.1+1234)

Inside the error box of this 3FGL S/N = 9.43 *Fermi* source (details in Appendix A11), we found only one bright X-ray counterpart with data in the radio, optical and IR. This appears to be a robust and unique counterpart for 2FGL J1704.3+1235. For this source, the SDSS survey reports the presence of an unresolved reddish object, in the source position, classified as a *star*. Based on our *blazar*-like SED recognition tool (Fig. 22), we find two possible solutions. One is in terms of an HSP object with tentative redshift $z = 0.3$. A fit at this redshift appears to be confirmed by some evidence of an host

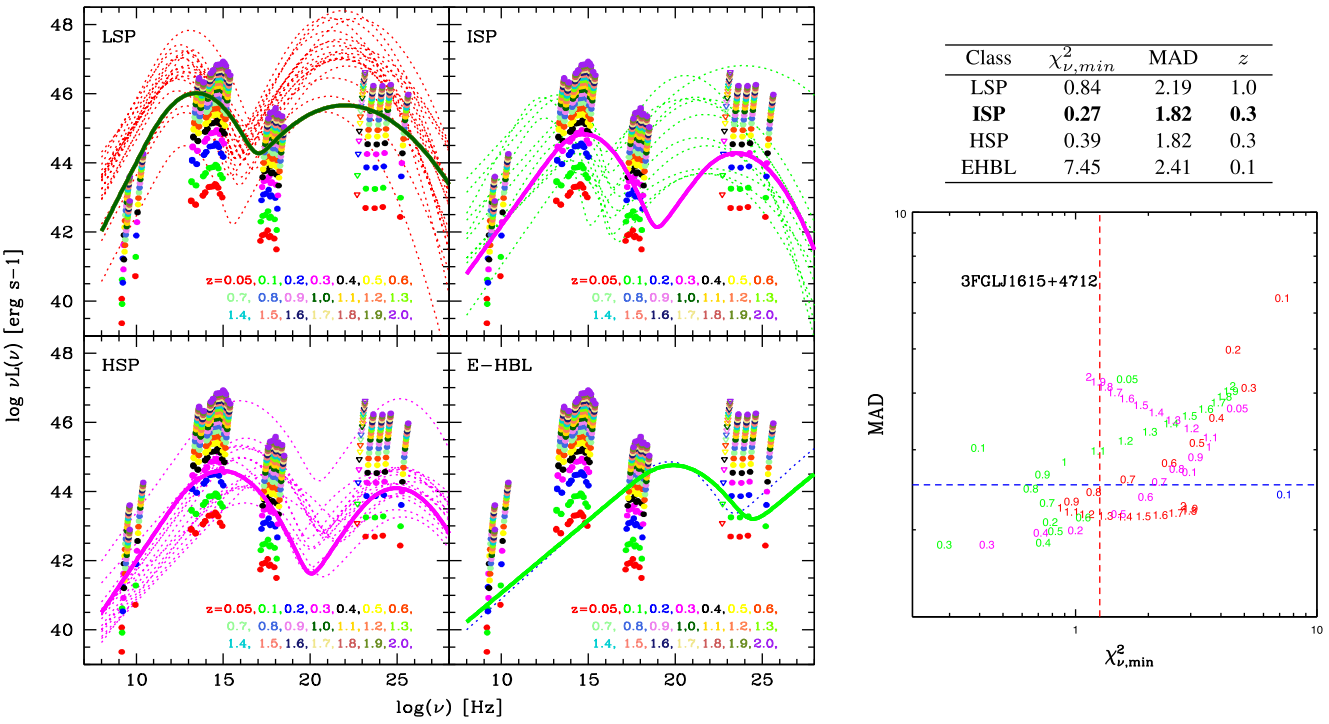

Class	$\chi^2_{\nu,min}$	MAD	z
LSP	0.84	2.19	1.0
ISP	**0.27**	**1.82**	**0.3**
HSP	0.39	1.82	0.3
EHBL	7.45	2.41	0.1

Figure 21. The same diagnostic plot as in Fig. 13 for the source 2FGL J1614.8+4703. Here, the best-guess recognition is an ISP at $z \sim 0.3$ (magenta line).

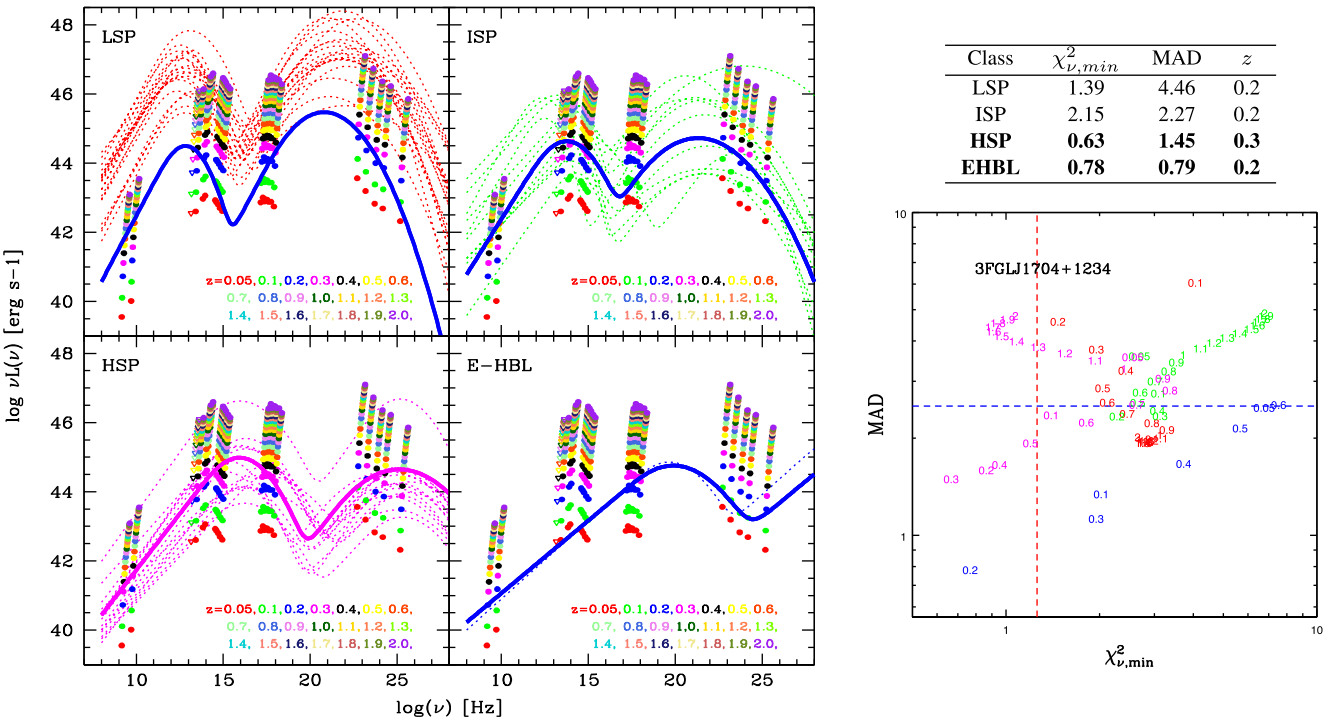

Class	$\chi^2_{\nu,min}$	MAD	z
LSP	1.39	4.46	0.2
ISP	2.15	2.27	0.2
HSP	**0.63**	**1.45**	**0.3**
EHBL	**0.78**	**0.79**	**0.2**

Figure 22. The same diagnostic plot as in Fig. 13 for the source 2FGL J1704.3+1235. Here, we propose two best-guess solutions in terms of an HSP object at $z \sim 0.3$ (magenta line) and EHBL at $z \sim 0.2$.

galaxy contribution in the optical, as illustrated in Fig. A11. Despite our resulting fit to the *Fermi* data turns out to be quite poor, our result is in broad agreement with the classification provided by Álvarez Crespo et al. (2016), where the optical spectrum of the proposed potential counterpart suggests a BL Lac object nature with a redshift of $z = 0.45$. The other solution is instead for an EHBL classification with $z = 0.2$. This source certainly requires further scrutiny, given the robustness and the uniqueness of the *association*.

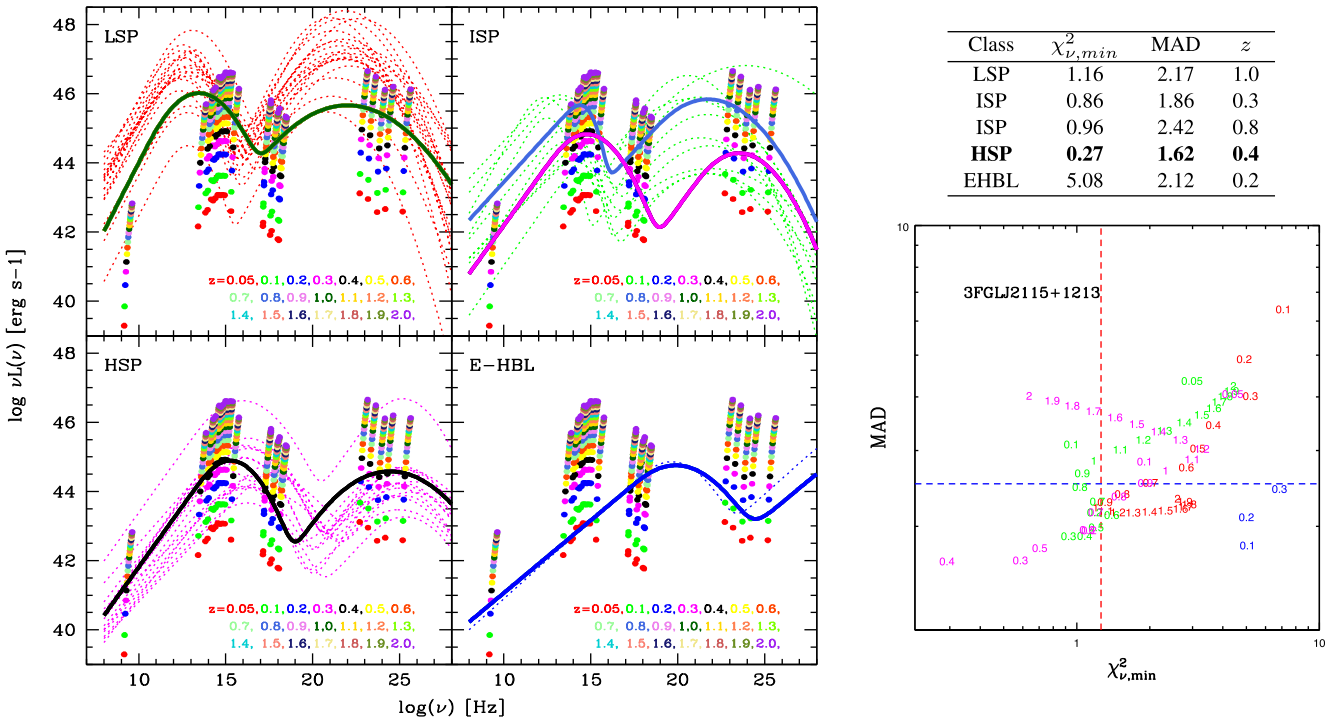

Class	$\chi^2_{\nu,min}$	MAD	z
LSP	1.16	2.17	1.0
ISP	0.86	1.86	0.3
ISP	0.96	2.42	0.8
HSP	**0.27**	**1.62**	**0.4**
EHBL	5.08	2.12	0.2

Figure 23. The same diagnostic plot as in Fig. 13 for the source 2FGL J2115.3+1549. For this source, we propose the best-guess solution in terms of an HSP at $z \sim 0.4$ (black line).

6.11 2FGL J2115.4+1213 (3FGL J2115.2+1213)

Of the two X-ray sources found in the 3FGL error box of 2FGL J2115.4+1213, as discussed in Appendix A12, the fainter one has essentially no counterparts in other bands. Instead, for the brighter X-ray source, XRT J211522+121801, we find counterparts in all bands, and for this reason, it is proposed as our likely X-ray counterpart. Based on our *blazar* recognition algorithm (see Fig. 23), we suggest that 2FGL J2115.4+1213 is a *blazar* of the HSP class at redshift $z = 0.4$. About the optical counterpart, the SDSS survey reports the presence of an unresolved object that is classified as a *star*.

6.12 2FGL J2246.3+1549 (3FGL J2246.2+1547)

This gamma-ray emitter is reported in the 3FGL and 3LAC catalogues with a detection significance of 9.5σ, and it is classified as a *blazar* candidate of unknown type (BCU-II) with an ISP SED classification and an unknown redshift. From the analysis of the XRT data covering the error-box field (discussed in Appendix A13), we found only one faint X-ray source with positional counterparts in various bands. Despite this source is not within the 3FGL, we suggest this as X-ray counterpart because it is the only X-ray source detected around the 2FGL J2246.3+1549 sky region and, moreover, our proposal is in agreement with the 3FGL association. The plots based on our tool are shown in Fig. 24. The best-fitting SED template indicates a classification as ISP object with a tentative redshift from $z \sim 0.3$ to ~ 0.8, although the upper value corresponds to an only marginally acceptable MAD.

6.13 2FGL J2347.2+0707 (3FGL J2346.7+0705)

Inside the 3FGL error box of this S/N = 13.83 *Fermi* source of 3 arcmin (see Appendix A14), we found a bright X-ray source with good counterparts in the radio, optical and IR. This counterpart set is in agreement with the 3FGL and 3LAC association, where the source is classified as a BCU-II with an ISP SED and with unknown redshift. Based on our *blazar* recognition code (see Fig. 25), we suggest that the source is a *blazar* of the ISP–HSP class with a best-fitting redshift of $z = 0.2$. The SDSS survey (dr12) reports the presence of an $r = 16.62$ BL Lac object in our proposed counterpart position, for which a spectroscopic redshift of $z \sim 0.17$ is provided by the SDSS automatic analysis procedure, and that is in good agreement and supportive of our result. Further dedicated optical observations are needed to confirm this result.

7 DISCUSSION AND CONCLUSIONS

The *Fermi* mission unveiled a mine of information about the high-energy Universe, which is far from having been completely exploited yet. In particular, a large fraction of the sources of the 2FGL catalogue and a comparable fraction in 3FGL are still waiting for reliable identification. As many as 576 of those high-confidence UGSs may be either pulsars, other kinds of Galactic objects or more likely high-energy-emitting AGNs, mainly BL Lac objects or FSRQs. There is also a non-negligible chance that these signals might hide entirely new classes of sources, and even the electromagnetic signatures of (either decaying or annihilating) non-baryonic massive particles that are expected to constitute the DM in the Universe. In the recently released 3FGL catalogue, there are 1010 unidentified sources, exactly one-third of the 3034 detected sources.

As a further step towards a more complete characterization of the UGS population, we discussed in this paper a new method for recognizing sources with a *blazar*-like SED among the UGSs. This tool is based on the observed multiwavelength flux density data, and takes advantage of some well-recognized regularities in the spectral properties of the *blazar* population, like the dependence of the peak

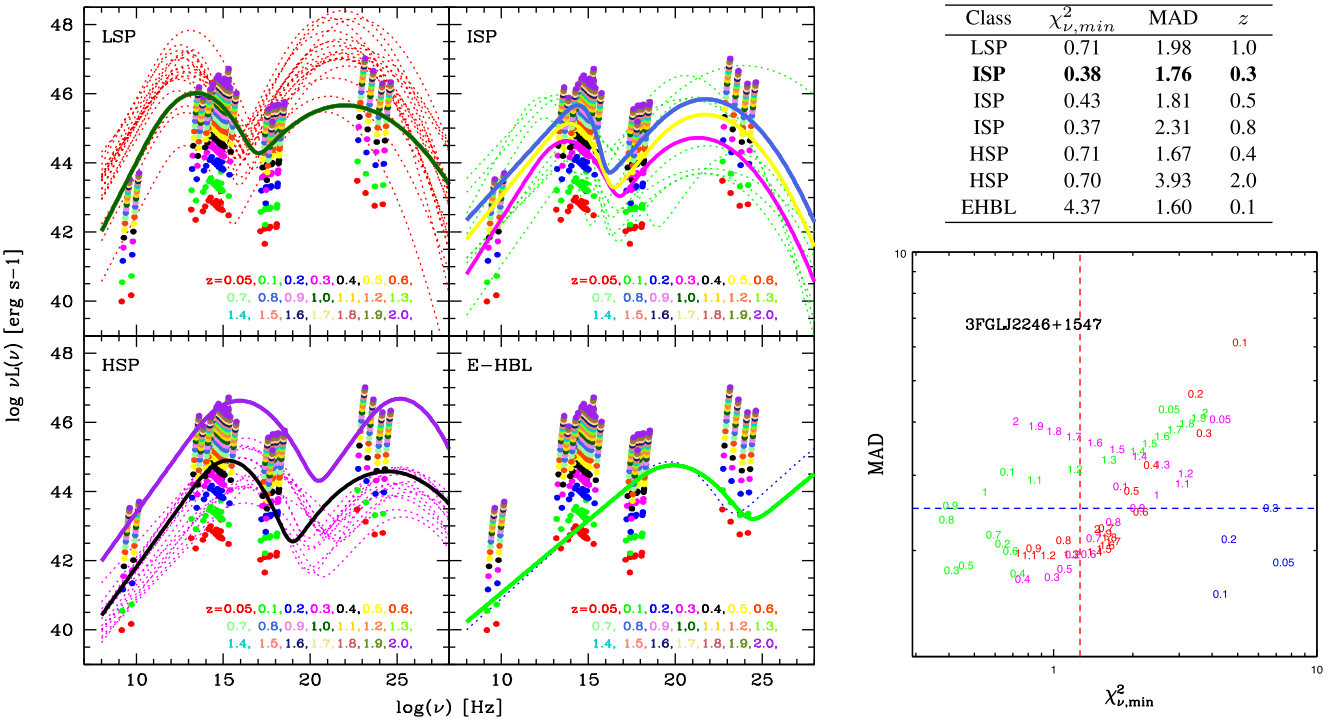

Class	$\chi^2_{\nu,min}$	MAD	z
LSP	0.71	1.98	1.0
ISP	**0.38**	**1.76**	**0.3**
ISP	0.43	1.81	0.5
ISP	0.37	2.31	0.8
HSP	0.71	1.67	0.4
HSP	0.70	3.93	2.0
EHBL	4.37	1.60	0.1

Figure 24. The same diagnostic plot as in Fig. 13 for the source 2FGL J2246.3+1549. For 2FGL J2246.3+1549, we propose two best-guess solutions in term of an ISP at either $z \sim 0.3$ (magenta line) or at $z \sim 0.8$ (blue line).

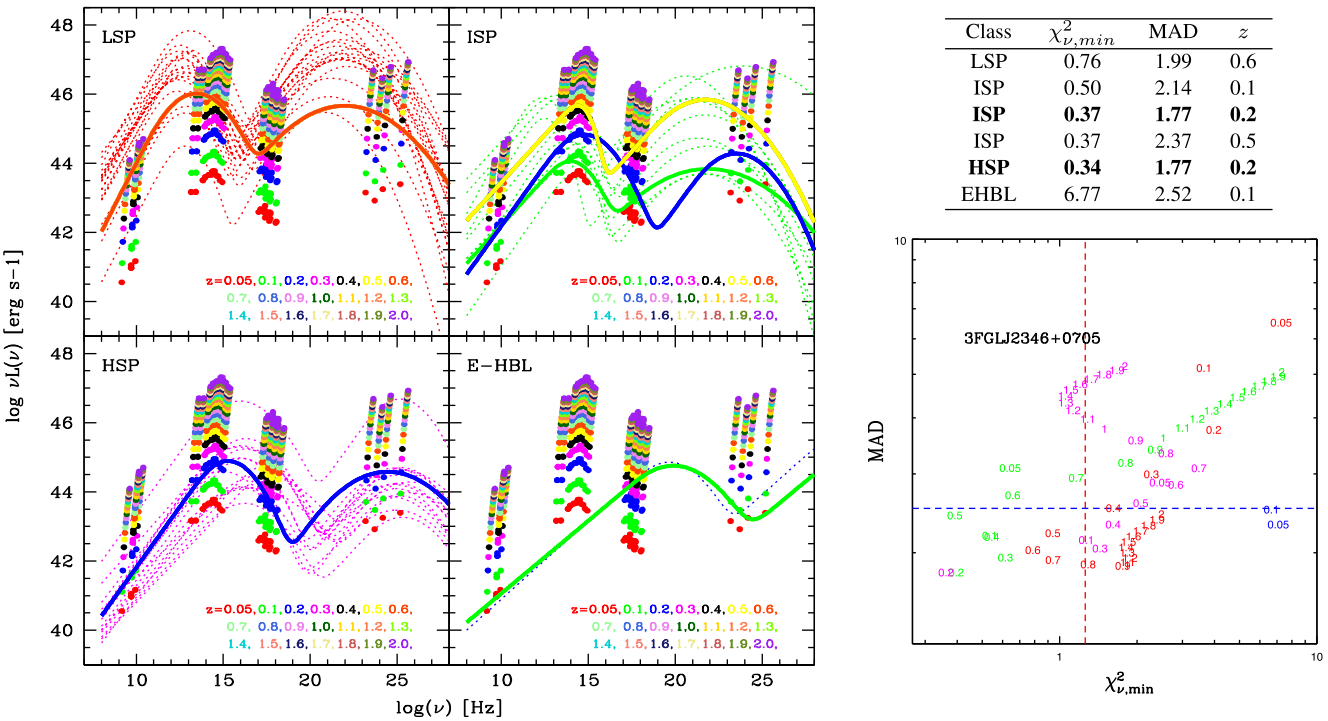

Class	$\chi^2_{\nu,min}$	MAD	z
LSP	0.76	1.99	0.6
ISP	0.50	2.14	0.1
ISP	**0.37**	**1.77**	**0.2**
ISP	0.37	2.37	0.5
HSP	**0.34**	**1.77**	**0.2**
EHBL	6.77	2.52	0.1

Figure 25. The same diagnostic plot as in Fig. 13 for the source 2FGL J2347.2+0707. Here, the best-guess recognition is an HSP–ISP at $z \sim 0.2$ (yellow line).

frequencies of the synchrotron and IC on source luminosity, and the spectral slopes. The procedure is tested by comparison with a few well-known *blazars*, pulsars and other Galactic sources, and then used for proposing the recognition of 14 UGSs selected in the 2FGL catalogue at high galactic latitudes. The 3FGL classification for these 14 sources includes 7 UGSs, 3 *blazars* (two BL Lac objects and one FSRQ) and 4 active galaxies of unknown type (BCU).

A summary of our results is reported in Table 3, and for all sources of our UGS sample, we report our proposed *blazar* typology and a rough estimate of the redshift. We find *blazar*-like counterparts for

Table 3. Summary of our proposed *blazar* classification and SED analysis for the UGS sample considered in this work. In the first column, we report the 2FGL name and the X-ray source name proposed as likely counterparts; in the second and third columns, we report the 3FGL name and the classification (UGS = unassociated gamma-ray source, BCU = active galaxy of uncertain type, BLLac = BL Lac object type, FSRQ = flat spectrum radio quasar) and the SED class; in the fourth column we report the coordinates of the optical source of the proposed X-ray counterpart (the ∗ symbol indicates that the proposed counterpart is an SDSS source); the fifth and sixth columns are the classification type and the estimated redshift found by running our *blazar* recognition tool; and finally, the spectroscopic classification (BLL = BL Lac object, NLSY1 = narrow-line Seyfert 1 galaxy, G = elliptical galaxy) and the redshift reported in literature (see for details the text of the notes for each source) for the proposed optical source counterpart.

2FGL name Counterpart name	3FGL name	3FGL (SED) classification	Optical coordinates (RA, Dec.)	AGN class proposed	Redshift from tool	Classification and Redshift from spectroscopy
2FGL J0102.2+0943 XRT J010217+094411	3FGL J0102.1+0943	UGS (–)	(01 02 17.11, +09 44 9.53)*	HSP	0.5	–
2FGL J0116.6−6153 XRT J011619−615340	3FGL J0116.3−6153	BLLac (ISP)	(01 16 19.58, −61 53 43.08)	HSP	0.4	BLL, $z = ?$
2FGL J0143.6−5844 XRT J014347−584551	3FGL J0143.7−5845	BLLac (HSP)	(01 43 47.40,−58 45 51.48)	HSP	0.3	–
2FGL J0338.2+1306 XRT J033829+130216	3FGL J0338.5+1303	BCU-II (HSP)	(03 38 29.26, +13 02 15.72)	HSP	0.3	BLL, $z = ?$
2FGL J1129.5+3758 XRT J112903−375857	3FGL J1129.0+3758	UGS (–)	(11 29 03.36, +37 56 56.07)	LSP	1.6	–
2FGL J1410.9+7406 XRT J141045+740509	3FGL J1410.9+7406	UGS (–)	(14 10 45.84, +74 05 11.04)	HSP	0.5-0.6	NSLY1, $z = 0.429$
2FGL J1502.1+5548 1SXPS J150229.0+555204	3FGL J1502.2+5553	UGS (–)	(15 02 29.07, 55 52 04.09)	LSP-ISP	0.7-1.7	–
2FGL J1511.8−0513 XRT J151148-051348	3FGL J1511.8−0513	BCU-III (–)	(15 11 48.48, −05 13 46.74)	HSP	0.1-0.2	BLL, $z = ?$
2FGL J1544.5−1126 XRT J154439−112804	3FGL J1544.6−1125	UGS (–)	(15 44 39.36, −11 28 04.44)	counter-example	–	–
2FGL J1614.8+4703 XRT J161541+471110	3FGL J1615.8+4712	FSRQ (LSP)	(16 15 41.28, +47 11 11.76)*	ISP	0.3	G, $z = 0.19$
3FGL J1704.3+1235 XRT J170409+123421	3FGL J1704.1+1234	UGS (–)	(17 04 09.60, +12 34 21.36)*	HSP	0.3	BLL, $z = 0.45$
2FGL J2115.4+1213 XRT J211522+121801	3FGL J2115.2+1213	UGS (–)	(21 15 22.08, +12 18 02.88)	HSP	0.4	–
2FGL J2246.3+1549 XRT J224005+154434	3FGL J2246.2+1547	BCU-II (ISP)	(22 46 05.04, +15 44 35.52)*	ISP	0.3–0.8	–
3FGL J2347.2+0707 XRT J234640+070507	3FGL J2346.7+0705	BCU-II (ISP)	(23 46 39.84, +07 05 06.86)*	ISP–HSP	0.2	BLL, z=0.17

13 of these UGSs (the remaining one is 2FGL J1544.5−1126, our counter-example for which we disfavour an AGN classification): The majority of them belong to the HSP class, a couple are of the LSP class and two of the ISP class. This is in agreement with the results of previous works, such as Mirabal et al. (2012) and Doert & Errando (2014), and with the *Fermi* 3LAC classification when a given UGS is classified as AGN in the 3FGL catalogue. Identification works based on optical spectroscopic observations (i.e. Masetti et al. 2013; Landoni et al. 2015; Álvarez Crespo et al. 2016; Marchesini et al. 2016) show the typical power-law optical spectrum for seven sources of our UGS sample, and therefore they confirm our classification and redshift (in the case of presence of emission and absorption lines). For our proposed counterparts, we suggest substantial values of redshift, from about $z \sim 0.2$ upwards. These relatively high redshifts may partly explain their lack of previous association or identification in published catalogues, although other explanations are possible.

To better understand the general properties of these new counterparts, and to further test the reliability of our method, we have built colour–colour diagrams for *Fermi* sources of various nature, based on existing multiwavelength data. These sources include pulsars, microquasars and AGNs, the latter classified by the 3LAC catalogue into HSPs, ISPs and LSPs, corresponding to our *blazar* classification scheme.

In Fig. 26 (upper panel), we plot the γ-ray-to-X-ray flux ratios versus radio-to-X-ray ratios. For ease of comparison with previous works, we also plot the corresponding broad-band spectral indices (bottom panel). The radio and X-ray fluxes of the counterparts associated with the 3FGL sources of different astronomical classes have been derived from the 3LAC and 2PC (the Second Pulsar Fermi Catalogue; Abdo et al. 2013) catalogues. As we see, there is a clear separation between the HSP and LSP classes of sources, while the ISP objects span the whole range of properties from HSP to LSP. A total of 12 of the 2FGL UGSs that we recognize as *blazar*s in this paper (and for which we could calculate the radio-to-gamma-ray spectral index) are shown as black points in Fig. 26. All of them are situated in the *blazar* region, in agreement with our proposed classification. There is also a good agreement between the colour region and our estimate of the UGS *blazar* classes, perhaps with the exception of sources 1 and 2 in the plot, which we classify

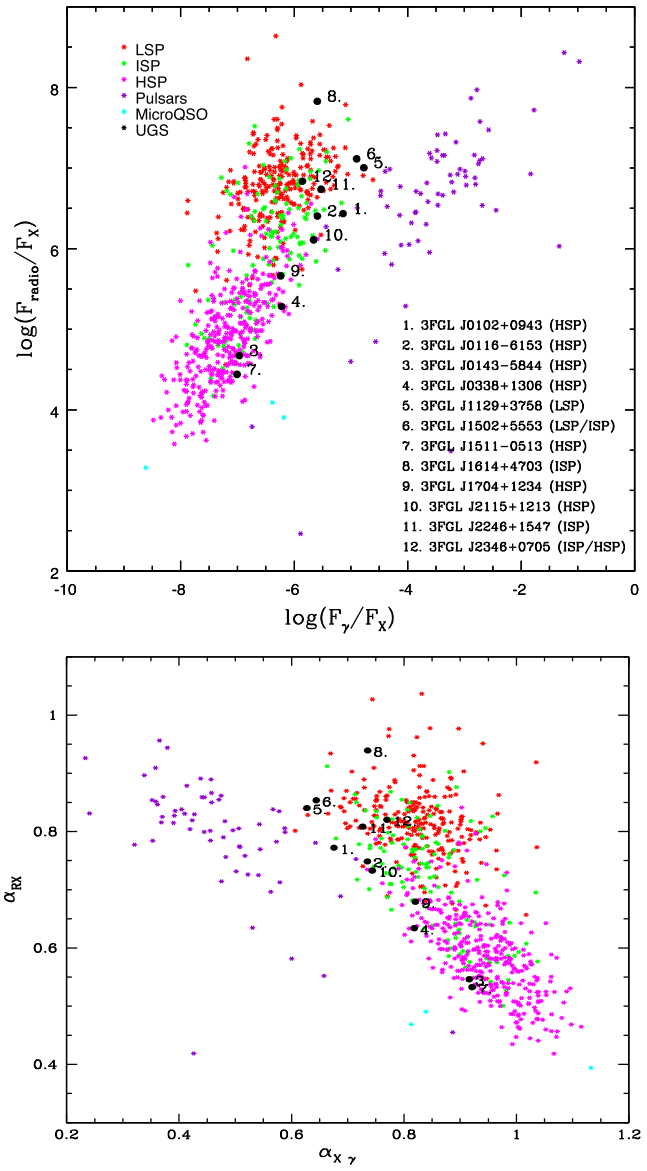

Figure 26. Top panel: the gamma-ray-to-X-ray versus radio-to-X-ray flux ratios for 3FGL objects of different classes. Bottom panel: the gamma-ray-to-X-ray spectral indices versus radio-to-X-ray spectral indices for the same 3FGL objects. The broad-band spectral index is defined as $\alpha_{ij} \equiv -\log(F_j/F_i)/\log(\nu_j/\nu_i)$. Red, magenta and green stars indicate the *blazar* sources categorized into LSP, ISP and HSP objects. Violet stars represent the data points of sources that are associated with pulsars in the 2PC and 2FGL catalogues. The black points show 12 UGSs studied in this paper and for which we provide a possible recognition as *blazars*. The inset details the UGS names and our proposed *blazar* classification.

as HSP, but that fall in the ISP colour region. The rest of our associated objects, instead, fall in the expected regions. We also note a tendency for our UGSs to fall closer to the right-hand-side border of the multiwavelength colour distributions (to the left-hand side of the spectral index region), while the radio to X-ray colour appears consistent. This is likely explained as a selection effect due to the higher than average gamma-ray and lower than average X-ray fluxes for our UGSs compared to standard luminous *blazar*s in the *Fermi* catalogues.

The obvious next step will be to obtain spectroscopic observations of our proposed UGS counterparts lacking a optical spectrum. Given the brightness of the sources and their characteristic featureless spectrum, confirming a BL Lac nature of the candidates, or the LSP nature from the strong emission lines, should be a relatively easy task. Much more difficult, or even impossible, might instead be the redshift measurement, for which, however, our analysis offers at least a guideline.

From tests carried out in this paper, our new method to study unassociated *Fermi* objects, based on the analysis of radio-to-γ total-band SEDs, appears to offer a valuable tool to assist in the investigation of the large number of gamma-ray sources still missing a physical interpretation.

ACKNOWLEDGEMENTS

We acknowledge helpful discussions and suggestions by Stefano Vercellone and Patrizia Romano. This work has benefited from a collaboration with the MAGIC project, in particular, the Padova MAGIC team. Edoardo Iani helped us to draw some of the figures.

This work made use of data supplied by the UK Swift Science Data Centre at the University of Leicester. Part of this work is based on archival data, software and online services provided by the ASI Science Data Centre (ASDC). This publication makes use of data products from the Wide-field Infrared Survey Explorer, which is a joint project of the University of California, Los Angeles, and the Jet Propulsion Laboratory/California Institute of Technology, funded by the National Aeronautics and Space Administration.

We are grateful to an anonymous referee for his careful reading and numerous suggestions that helped in improving this paper. The financial contributions by the contracts INAF ASTRI (PI: E. Giro) and INAF E-ELT (PI: R. Falomo), and by the Padova University, are also acknowledged.

The financial contributions by the contracts INAF ASTRI (PI: E. Giro) and INAF E-ELT (PI: R. Falomo), and by the Padova University, are also acknowledged.

REFERENCES

Álvarez Crespo N., Masetti N., Ricci F., Landoni M., Patiño-Álvarez V., 2016, AJ, 151, 32
Álvarez Crespo N., Massaro F., Milisavljevic D., Landoni M., Chavushyan V., Patiño-Álvarez V., Masetti N., 2016, AJ, 151, 95
Abdo A. A. et al., 2009, ApJS, 183, 46
Abdo A. A. et al., 2010, ApJS, 188, 405
Abdo A. A., Ackermann M., Ajello M., Antolini E. et al., 2010, ApJ, 722, 520
Abdo A. A. et al., 2013, ApJS, 208, 17
Acero F. et al., 2013, ApJ, 779, 133
Acero F. et al., 2015, ApJS, 218, 23
Ackermann M., Ajello M., Allafort A., Schady P., Baldini L., Ballet J., 2012, Science, 338, 1190
Ackermann M., Ajello M., Allafort A., Antolini E., Baldini L. et al., 2012, ApJ, 753, 83
Ackermann M., Ajello M., Atwood W. B., Baldini L., Ballet J., Barbiellini G. et al., 2015, ApJ, 810, 14
Ackermann M. et al., 2016, ApJS, 222, 5
Aharonian F., Akhperjanian A. G., Bazer-Bachi A. R. et al., 2006, Nature, 440, 1018
Ahn C. P. et al., 2012, ApJS, 203, 21
Ahn C. P. et al., 2014, ApJS, 211, 17
Albert J., Aliu E., Anderhub H., Antoranz P. et al., 2007, ApJ, 667, L21
Aleksić J., Alvarez E. A., Antonelli L. A. et al., 2012, A&A, 544, A142
Aleksić J., Antonelli L. A., Antoranz P. et al., 2013, A&A, 556, A67
Aleksić J., Ansoldi S., Antonelli L. A. et al., 2014a, A&A, 567, A41
Aleksić J., Ansoldi S., Antonelli L. A. et al., 2014b, A&A, 567, A135

Aleksić J., Ansoldi S., Antonelli L. A., Antoranz P., 2016, A&A, 591, A10
Arnaud K. A., 1996, in Jacoby G., Barnes J., eds, ASP Conf. Ser. Vol. 101, Astronomical Data Analysis Software and Systems V. Astron. Soc. Pac., San Francisco, p. 101
Atwood W. B. et al., 2009, ApJ, 697, 1071
Belikov A. V., Buckley M. R., Hooper D., 2012, Phys. Rev. D, 86, 043504
Bertone G., Hooper D., Silk J., 2005, Phys. Rep., 405, 279
Bogdanov S., Halpern J. P., 2015, ApJ, 803, L27
Bonnet-Bidaud J. M., de Martino D., Mouchet M., Falanga M., Belloni T., Masetti N., Mukai K., Matt G., 2012, Mem. Soc. Astron. Ital., 83, 742
Bonnoli G., Tavecchio F., Ghisellini G., Sbarrato T., 2015, MNRAS, 451, 611
Condon J. J., Cotton W. D., Greisen E. W., Yin Q. F., Perley R. A., Taylor G. B., Broderick J. J., 1998, AJ, 115, 1693
Costamante L. et al., 2001, A&A, 371, 512
Cutri R. M. et al., 2013, Explanatory Supplement to the AllWISE Data Release Products
D'Abrusco R., Massaro F., Paggi A., Masetti N., Tosti G., Giroletti M., Smith H. A., 2013, ApJS, 206, 12
Danforth C. W., Keeney B. A., Stocke J. T., Shull J. M., Yao Y., 2010, ApJ, 720, 976
Doert M., Errando M., 2014, ApJ, 782, 41
Donato D., Ghisellini G., Tagliaferri G., Fossati G., 2001, A&A, 375, 739
Evans P. A., Beardmore A. P., Page K. L., Osborne J. P. et al., 2009, MNRAS, 397, 1177
Evans P. A. et al., 2014, ApJS, 210, 8
Falcone A. et al., 2011, AAS/High Energy Astrophysics Division, Vol. 12, Systematic Search for X-ray Counterparts of Fermi-LAT Unassociated Sources Using Swift Observations. p. 04.03
Falcone A., Stroh M., Pryal M., 2014, American Astronomical Society Meeting Abstracts 223, Vol. 223, Using Swift to Obtain X-ray Monitoring of Fermi Blazars and X-ray Counterparts to Fermi Unassociated Sources. p. 301.05
Fossati G., Maraschi L., Celotti A., Comastri A., Ghisellini G., 1998, MNRAS, 299, 433
Franceschini A., Rodighiero G., Vaccari M., 2008, A&A, 487, 837
Franceschini A., Rodighiero G., 2017, A&A, in press
Gehrels N., 2004, ApJ, 611, 1005
Ghisellini G., Righi C., Costamante L., Tavecchio F., 2017, MNRAS, preprint (arXiv:e-prints)
Giroletti M., Massaro F., D'Abrusco R., Lico R., 2016, A&A, 588, A141
Goad M. R., Tyler L. G., Beardmore A. P., Evans P. A. et al., 2007, A&A, 476, 1401
Hewitt A., Burbidge G., 1993, ApJS, 87, 451
Landi R., Bassani L., Stephen J. B., Masetti N., Malizia A., Ubertini P., 2015, A&A, 581, A57
Landoni M. et al., 2015, AJ, 149, 163
MAGIC Collaboration et al., 2008, Science, 320, 1752
Marchesini E. J., Masetti N., Chavushyan V., 2016, A&A, 596, A10
Masetti N., Sbarufatti B., Parisi P. et al., 2013, A&A, 559, A58
Massaro E., Giommi P., Leto C., Marchegiani P., Maselli A., Perri M., Piranomonte S., Sclavi S., 2009, A&A, 495, 691
Massaro F., D'Abrusco R., Ajello M., Grindlay J. E., Smith H. A., 2011, ApJ, 740, L48
Massaro F., D'Abrusco R., Tosti G., Ajello M., Paggi A., Gasparrini D., 2012, ApJ, 752, 61
Mauch T., Murphy T., Buttery H. J., Curran J., Hunstead R. W., Piestrzynski B., Robertson J. G., Sadler E. M., 2003, MNRAS, 342, 1117
Mirabal N., Frías-Martinez V., Hassan T., Frías-Martinez E., 2012, MNRAS, 424, L64
Monet D. G., Levine S. E., Canzian B., Ables H. D. et al., 2003, AJ, 125, 984
Nolan P. L. et al., 2012, ApJS, 199, 31
Nori M., Giroletti M., Massaro F., D'Abrusco R., Paggi A., Tosti G., Funk S., 2014, ApJS, 212, 3
Paggi A., Massaro F., D'Abrusco R., Smith H. A., Masetti N., Giroletti M., Tosti G., Funk S., 2013, ApJS, 209, 9
Paiano S., Landoni M., Falomo R., Treves A., Scarpa R., Righi C., 2017, ApJ, 837, 144
Perlman E. S. et al., 1996, ApJS, 104, 251
Petrov L., Mahony E. K., Edwards P. G., Sadler E. M., Schinzel F. K., McConnell D., 2013, MNRAS, 432, 1294
Prandini E., Bonnoli G., Maraschi L., Mariotti M., Tavecchio F., 2010, MNRAS, 405, L76
Ray P. S. et al., 2015, available at http://www.iac.es/congreso/ns-ewass-2015/
Schinzel F. K., Petrov L., Taylor G. B., Mahony E. K., Edwards P. G., Kovalev Y. Y., 2015, ApJS, 217, 4
Skrutskie M. F., Cutri R. M., Stiening R., Weinberg M. D. et al., 2006, AJ, 131, 1163
Spergel D. N. et al., 2007, ApJS, 170, 377
Stephen J. B., Bassani L., Landi R., Malizia A., Sguera V., Bazzano A., Masetti N., 2010, MNRAS, 408, 422
Takahashi Y. et al., 2012, ApJ, 747, 64
Takeuchi Y., Kataoka J., Maeda K., Takahashi Y., Nakamori T., Tahara M., 2013, ApJS, 208, 25
Wright E. L. et al., 2010, AJ, 140, 1868
Zechlin H.-S., Horns D., 2012, J. Cosmol. Astropart. Phys., 11, 50
Zechlin H.-S., Fernandes M. V., Elsässer D., Horns D., 2012, A&A, 538, A93

APPENDIX A: MULTIWAVELENGTH COUNTERPARTS FOR A SELECTED SAMPLE OF *Fermi* UGSS

A1 2FGL J0102.2+0943

This UGS shows a detection significance of 7.09σ (5.5σ) and an error box of 4.8 arcmin (7.8 arcmin) in the 3FGL (2FGL) catalogue. Two observations are performed by *Swift*/XRT for a total exposure time of about 4000 s. Using the XRT imaging analysis tool of the UK Swift Science Data Centre, in the X-ray sky map (Fig. A1, upper left-hand panel), for this *Fermi* source, only one faint X-ray source is detected within the 3FGL error box (yellow ellipse), with (RA, Dec.) = ($01^{\rm h}02^{\rm m}17\overset{\rm s}{.}15$, $09^{\circ}44'11\overset{''}{.}16$) and a 90 per cent positional error radius of 4.5 arcsec. The estimated count rate is ($2.624\times 10^{-3} \pm 8.314\times 10^{-4}$) counts s^{-1} for a total of 11 counts. Superimposing the catalogues of the other wavelengths with the DS9 plotting tool (Fig. A1, upper right-hand panel), we find a positional coincidence with the radio source NVSS J010217+094407, the IR source 2MASS 01021713+0944098 and the optical source SDSS J010217.10+094409.5. Another IR source appears positionally coincident within the XRT error box, but we do not consider it because the coincidence is very marginal and the corresponding optical source is outside the region. Through the SED Builder tool of the ASI ASDC Data Centre, we build the multifrequency SED (Fig. A1, bottom panel), combining the fluxes of the proposed set of counterparts and including also the XRT flux data from Takeuchi et al. (2013) and the X-ray data points taken from the 1SXPS catalogue (Evans et al. 2014).

A2 2FGL J0116.6−6153

In the 3FGL (2FGL) catalogue, this object is reported with a detection significance of 9.90σ (5.5σ) and a 95 per cent semimajor axis of $0\overset{\circ}{.}04$ (6 arcmin). In the 3FGL, its new classification is a *blazar* of BL Lac type. Two *Swift*-XRT observations are available for a total of 3276 s. Through the UK Swift data analysis, we obtain the X-ray image shown in Fig. A2 (upper left-hand panel). Within the 3FGL error box (yellow ellipse), we detect only one X-ray source with (RA, Dec.) = ($01^{\rm h}16^{\rm m}19\overset{\rm s}{.}24$, $-61^{\circ}53'40\overset{''}{.}2$) with a 90 per cent

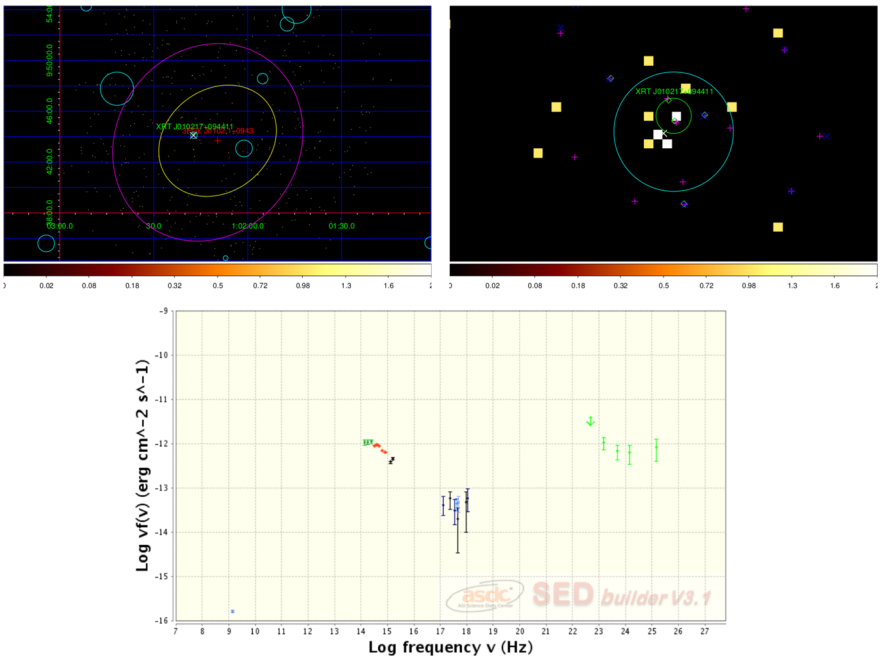

Figure A1. Upper left-hand panel: *Swift*/XRT images of 2FGL J0102.2 +0943 created using the online data analysis tool of UK Swift Science Data Centre. The red cross is the position of 2FGL J0102.2+0943 as reported in the 3FGL catalogue and the yellow (magenta) ellipse is the 95 per cent error region of the 3FGL (2FGL) catalogue. The XRT source detected in this work, XRT 010217+094411, is displayed as a green circle. The cyan circles show the error circles of the NVSS radio sources and the white crosses are *Swift*/XRT objects of the 1SXPS catalogue (Evans et al. 2014). Upper right-hand panel: close-up of the XRT J010217+094411 sky map. The white cross is the position of the XRT source in the 1SXPS catalogue. The blue and magenta crosses are the positions of *WISE* and SDSS objects, and the green diamonds correspond to 2MASS sources. Bottom panel: broad-band SED of 2FGL J0102.2+0943 created using the SED Builder tool of the ASI ASDC Data Centre. We combine NVSS radio data (light blue points), IR 2MASS data (dark green points) and SDSS optical data (red points) with the HE gamma-ray data (green points) from the 3FGL catalogue. The X-ray flux is taken from the 1SXPS catalogue (blue points) and from Takeuchi et al. (2013) (black points).

error radius of 5.7 arcsec. The estimated net count rate is ($6.424\times 10^{-3} \pm 1.432\times 10^{-3}$) counts s^{-1}. Hence, we propose this object as the most likely counterpart of 2FGL J0116.6−6153. From the close-up image in Fig. A2 (upper right-hand panel), the radio source SUMSS J011619−615343, the IR sources WISE J011619−615343 and 2MASS 01161959−6153434, and the optical source USNOB U0281−0014602 are spatially coincident with the X-ray position of XRT J011619−615340. The multiwavelength SED (Fig. A2, bottom panel) is built by combining all available flux data of this set of counterparts.

A3 2FGL J0143.6−5844

In the 3FGL (2FGL) catalogue, this source is reported with a detection significance of 18.98σ (14.2σ) and a 95 per cent semimajor axis of 2.4 arcmin (3.6 arcmin). The new 3FGL classification for the source is *blazar* of BL Lac type. 2FGL J0143.6−5844 has been observed by *Swift*/XRT, which was pointing at the coordinates of the 1FGL J0143.9−5845 and collecting 4348 s of good exposure time. The XRT sky map is shown in Fig. A3 (upper left-hand panel), with only one X-ray source detected within the 3FGL error box. We suggest XRT J014347−584551 as the likely X-ray counterpart for 2FGL J0143.6−5844. It is a very bright X-ray source with a count rate of ($3.765 \times 10^{-1} \pm 9.337\times 10^{-1}$) counts s^{-1}. The XRT-enhanced position is (RA, Dec.) = ($01^{h}43^{m}47^{s}.57$, $-58^{\circ}45'51''.6$) with an error radius of 1.9 arcsec. In the close-up image (Fig. A3, upper right-hand panel), we find that the radio source SUMSS J014347−584550, together with the IR sources WISE J014347−584551 and 2MASS 01434742−5845514, and the optical object USNOA2.0 U0300_00524092 are spatially coincident with the error region of the X-ray counterpart. In the bottom panel of the same figure, the corresponding broad-band SED built is shown. The magenta points are the X-ray data calculated from our dedicated XRT analysis, the black points are the X-ray spectrum taken from Takeuchi et al. (2013) and the blue points are from the 1SXPS catalogue.

A4 2FGL J0338.2+1306

This gamma-ray emitter is a *Fermi* source with a detection significance of 11.90σ (5.8σ) and an error box of 1.8 arcmin (6.6 arcmin) in the 3FGL (2FGL) catalogue. In the 3FGL catalogue, this source is classified as an active galaxy of uncertain type (BCU-II). It was observed by *Swift*/XRT on 2012 July 4 with an exposure time of 3344 s. The resulting XRT sky map is shown in Fig. A4 (upper left-hand panel). We found only one X-ray source, XRT J033829+130216, within the 3FGL error box (yellow ellipse). Therefore, we decide to propose it as the most likely X-ray counterpart, according to the 3FGL association. From the image analysis, the XRT positional error for this source is 2.1 arcsec and its count rate is ($7.160\times 10^{-2} \pm 4.653\times 10^{-3}$) counts s^{-1} with 242 total counts found. Using an appropriate absorbed model, the integral flux in the energy range 0.3–10 keV is 4.1319×10^{-12} erg cm^{-2} s^{-1}. Looking at the close-up image (Fig. A4, upper right-hand panel), we can see that the radio source NVSS J033829+130215, the IR sources WISE J033829+130215 and 2MASS 03382926+1302151, and the

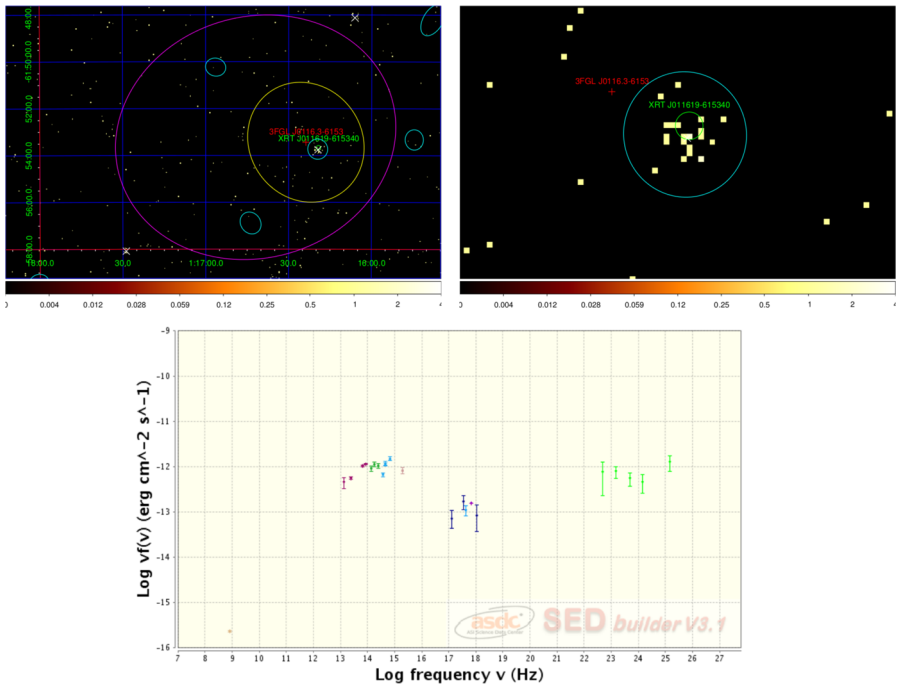

Figure A2. Upper left-hand panel: *Swift*/XRT images of 2FGL J0116.6 −6153 created using the online data analysis tool of UK Swift Science Data Centre. The red cross is the 2FGL J0116.6−6153 position as reported in the 3FGL, and the yellow (magenta) ellipse is the 95 per cent error region of 3FGL (2FGL) catalogue. The X-ray source XRT J011619−615340, detected in this work, is displayed as a green circle. The cyan ellipses show the error ellipses of the SUMSS radio sources and the white crosses are *Swift*/XRT objects of the 1SXPS catalogue (Evans et al. 2014). Upper right-hand panel: close-up sky map of XRT J011619−615340. The blue and magenta crosses are the positions of *WISE* and USNO objects, and the green diamond corresponds to 2MASS source. Bottom panel: broad-band SED of 2FGL J0116.6−6153 created using the SED Builder tool of the ASI ASDC Data Centre. We combine SUMSS radio data (beige point), *WISE* and 2MASS IR data (violet and green points), and USNOB1.0 optical data (blue points) with the HE γ-ray data (green points) from the 3FGL catalogue. The X-ray data points (blue points) are taken from the 1SXPS catalogue.

optical USNOB 1030−0045117 are spatially coincident with the X-ray object. The multifrequency SED (bottom panel) is obtained by combining the data points of these objects.

A5 2FGL J1129.5+3758

In the 3FGL catalogue, 2FGL J1129.5+3758 is still an unidentified object with a detection significance = 10.25σ and a 95 per cent semimajor axis of 3.6 arcmin. In 2014, the *Swift* satellite provided about 4700 s of data. Through the X-ray image analysis, we found that within the reduced 3FGL error box of this source, there is one X-ray source [XRT J112903+375857 with (RA, Dec.) = $21^{h}15^{m}22\overset{s}{.}08, 12^{\circ}18'01\overset{''}{.}8$] detected (Fig. A5, upper left-hand panel). We propose it as the likely X-ray counterpart of this UGS, and the close-up image shows its multifrequency counterparts within the X-ray error circle of radius 4.7 arcsec: the radio source NVSS J112903+375655, the IR objects WISE J112903+375655 and 2MASS 11290325+3756564, and the optical object SDSS J112903.24+375656.7. In the bottom panel, the corresponding multiwavelength SED is reported.

A6 2FGL J1410.4+7411

In the 2FGL catalogue, 2FGL J1410.4+7411 has a 9.8σ significance and a *semimajor axis* of 4.8'. In the 3FGL catalogue, the unassociated source 3FGL J1410.9+7406 is reported with a detection significance of 15.76σ and a *semimajor axis* of 2.4 arcmin . We suggest that 2FGL J1410.4+7411 and 3FGL J1410.9+7406 are the same gamma-ray emitter. There are several short *Swift*/XRT observations provided between 2011 and 2014, and from the resulting XRT sky map, shown in Fig. A6 (upper left-hand panel), we can find two X-ray 1SXPS sources (white crosses). We suggest the brightest one, the source XRT J141045+740609, as the likely X-ray counterpart for 3FGL J1410.9+7406. From the image analysis, the XRT positional error for this source is 4.5 arcsec. Looking at the close-up image (upper right-hand panel), we can see that the IR sources WISE J141046+740511 and the optical USNOB 1640-0083647 are spatially coincident with the X-ray object. The multifrequency SED of 2FGL J1410.4+7411 and 3FGL J1410.9+7406 is obtained by combining the data points of these objects and the X-ray data points provided by the 1SXPS catalogue (blue points).

A7 2FGL J1502.1+5548

In the 3FGL catalogue, this UGS is reported with a detection significance of 12.64σ and a 95 per cent semimajor axis of 4.2 arcmin. 2FGL J1502.1+5548 has been observed by *Swift*/XRT, and ∼4000 s of good exposure time was collected. The XRT sky map is shown in Fig. A7 (upper left-hand panel), and we were able to detect two X-ray sources that are located outside the 3FGL error box, but within the 3FGL error box. From the high-quality 1SXSP catalogue (Evans et al. 2014), we note that the source 1SXSP J150229.0+555204 (with a positional error radius of 5.9 arcsec), coincident with the radio source NVSS J150229+555204, can be considered the most likely counterpart for 2FGL J1502.1+5548. In the close-up image of 1SXSP J150229.0+555204 (upper right-hand panel), we

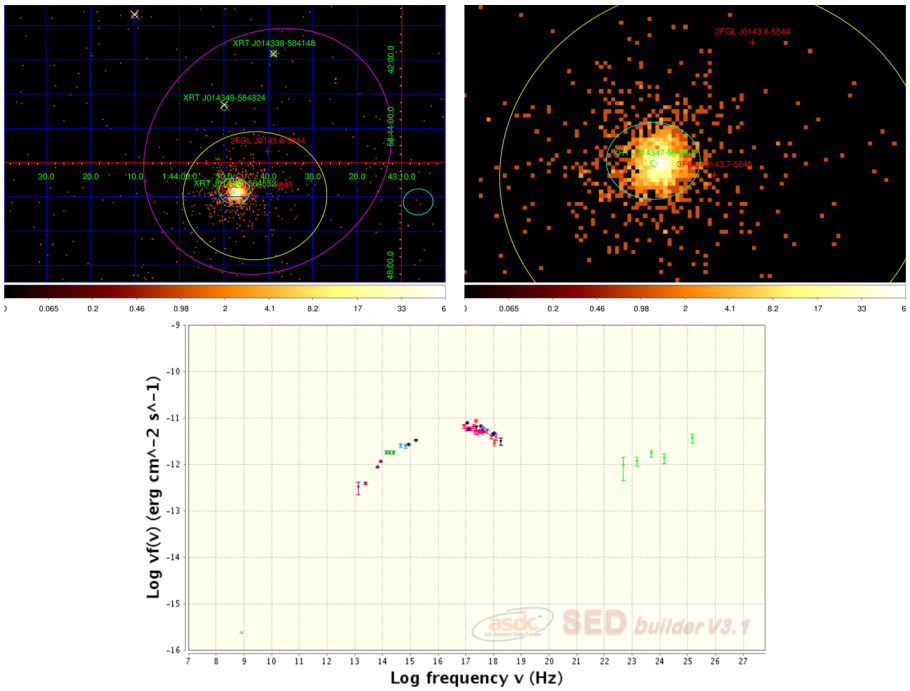

Figure A3. Upper left-hand panel: *Swift*/XRT images of 2FGL J0143.6 −5844 created using the online data analysis tool of UK Swift Science Data Centre. The red crosses are the 2FGL J0143.6−5844 and 3FGL J0143.6−5845 position, and the yellow (magenta) ellipse is the 95 per cent error region of 3FGL catalogue. The XRT sources detected in this work are displayed as green circles with a radius equal to the XRT error radius. The cyan ellipses show the error ellipses of the SUMSS radio sources and, with crosses, are *Swift*/XRT objects of the 1SXPS catalogue. Upper right-hand panel: close-up of the XRT 014347−584551 sky map. The white cross is the position of the XRT source in the 1SXPS catalogue. The blue and magenta crosses are the positions of *WISE* and USNO objects and the green diamonds correspond to 2MASS sources. Bottom panel: broad-band SED of 2FGL J0143.6−5844 created using the SED Builder tool of the ASI ASDC Data Centre. We combine SUMSS radio data (beige points), *WISE* and 2MASS IR data (violet and green points), and USNOA2.0 optical data (light blue points) with the HE gamma-ray data (green points) from the 3FGL catalogue. The X-ray data points are given from our *Swift*/XRT analysis (magenta points), from Takeuchi et al. (2013) (black points) and from the 1SXPS catalogue (blue points).

find that, besides the radio source, only the optical source SDSS J150229.07+555204.9 is spatially coincident with the X-ray counterpart. There are no IR sources detected, and the closest one is located outside the X-ray error box and associated with the star very close to SDSS J150229.07+555204.9 (see the finding chart in Fig. A7, bottom right-hand panel). In the same figure (bottom left-hand panel), the corresponding broad-band SED built is shown.

A8 2FGL J1511.8−0513

In the 3FGL (2FGL) catalogue, this source shows a detection significance of 10.59σ (7.8σ) and a *semimajor axis* of 3 arcmin (4.8 arcmin). In the 3FGL, this source is not unassociated, but it is classified as an active galaxy with an uncertain type. By pointing at the position of the 1FGL source, *Swift*/XRT observed the 2FGL J1511.8−0513 sky region in 2010 for a total time of 4160 s. The XRT data analysis was performed by the UK XRT analysis tool and the resulting sky map is shown in Fig. A8 (upper left-hand panel). Within the 3FGL error box, we found only one X-ray source, with (RA, Dec.) = ($15^{h}11^{m}48^{s}.55$, -05° $13'48''.00$) and a 90 per cent error radius of 1.9 arcsec. We propose it as the X-ray counterpart in agreement with the 3FGL association. From the close-up image in Fig. A8 (upper right-hand panel), the radio source NVSS 151148−051345, the IR sources WISE J151148−051346 and 2MASS 15114857−0513467, and the optical source USNOB U0825.08626045 are spatially coincident with the X-ray position of XRT J151148−051348. The multiwavelength SED (bottom panel) is built by combining all available flux data of this set of counterparts. The X-ray flux is derived by our dedicated *Swift*-XRT analysis (magenta points), and, in addition, we plot the X-ray data points taken from the 1SXPS catalogue (blue points) and Takeuchi et al. (2013) (black points).

A9 2FGL J1544.5−1126

2FGL J1544.5−1126 shows a detection significance of 10.85σ (5.79σ) and a 95 per cent semimajor axis of 4.8 arcmin (8.4 arcmin) in the 3FGL (2FGL) catalogue. *Swift*/XRT did not observe it directly, but pointed to the *ROSAT* source 1RXS J154439.4−112820, from 2006 to 2012, for an exposure time of 13 350 s. This object is the brightest X-ray source within the 3FGL error box (yellow ellipse) of 2FGL J1544.5−1126 (Fig. A9, upper left-hand panel). We suggest it as the likely X-ray counterpart. From the XRT data analysis, we find that this X-ray counterpart has an error box of 1.7 arcsec. In the close-up image (upper right-hand panel), the IR object WISE J154439−112804 and the optical source USNOB1.0 0785−0287377 are positionally coincident, and, hence, we consider them as associated with 2FGL J1544.5−1126. The estimated XRT count rate is ($7.003\times 10^{-2} \pm 2.311\times 10^{-3}$) counts s^{-1} and the integrated 0.3–10 keV flux is 4.4394×10^{-12} erg cm^{-2} s^{-1} (935 total counts). The X-ray differential spectrum (magenta points) is plotted in the multiwavelength SED (bottom panel) together with the X-ray spectrum taken from Takeuchi et al. (2013) (black points) and the data points provided by the 1SXPS catalogue (blue points).

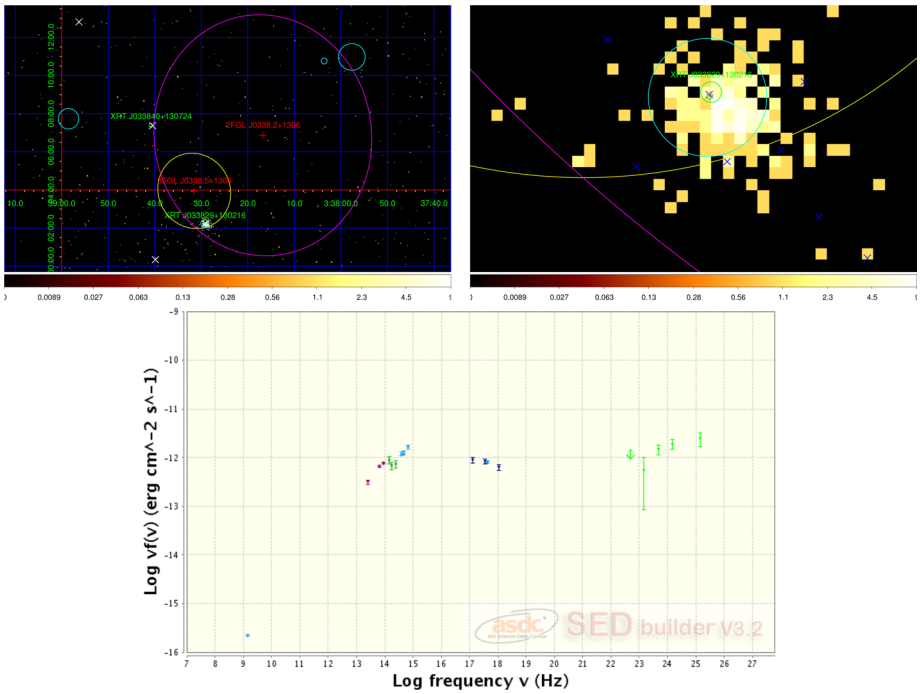

Figure A4. Upper left-hand panel: *Swift*/XRT images of 2FGL J0338.2 +1306 created using the online data analysis tool of the UK Swift Science Data Centre. The red crosses are the 2FGL and 3FGL positions, and the yellow (magenta) ellipse is the 95 per cent error region of the 3FGL (2FGL) catalogue. The XRT sources detected in this work are displayed as green circles with a radius equal to the XRT error radius. The cyan ellipses show the error circles of the NVSS radio sources and the white crosses are the*Swift*/XRT objects of the 1SXPS catalogue. Upper right-hand panel: close-up of the XRT J033829+130216 sky map. The white cross is the position of the XRT source in the 1SXPS catalogue. The blue and magenta crosses are the positions of *WISE* and USNO objects, and the green diamonds correspond to 2MASS sources. Bottom panel: broad-band SED of 2FGL J0338.2+1306 created using the SED Builder tool of the ASI ASDC Data Centre. We combine NVSS radio data (blue point), *WISE* and 2MASS IR data (violet and green points), and USNO B1.0 optical data (light blue points) with the HE gamma-ray data (green points) from the 3FGL catalogue. The X-ray flux points are obtained from the 1SXPS catalogue (blue points).

A10 2FGL J1614.8+4703

2FGL J1614.8+4703 is a very faint gamma-ray emitter with a detection significance of 4.59σ and a rather large Fermi 95 per cent semimajor axis of 13.8 arcmin. In the 3FGL and 3LAC catalogues, this object is a 6.30σ source with a 95 per cent semimajor axis of 5.4 arcmin, and it is associated with the source TXS 1614+473, classified as LSP *blazar*. The *Swift*/XRT pointings for this source were targeted to the IR source 2MASX J16154117+47111 for 4990 s (see Fig. A10, upper left-hand panel). Only the source XRT J161541+471110 is detected and we suggest it as the likely X-ray counterpart, in agreement with the 3FGL association. The close-up image around the XRT J161541+47111 position (upper right-hand panel) shows it to be within the XRT positional error of 4.8 arcsec, and we can find the IR objects WISE J161541+471111 and 2MASS 16154121+4711118, and the optical object SDSS J161541.21+471111.7 spatially coincident. For the latter, the SDSS survey[9] identifies the source with an elliptical galaxy at redshift of 0.19 (bottom right-hand panel). The multiwavelength SED for 2FGL J1614.8+4703 is displayed in the bottom left-hand panel by combining all flux data of the proposed counterparts. The magenta points indicate the X-ray spectrum estimated through our UK online analysis of the XRT J161541+471110 data, while the blue points are the X-ray data flux taken from 1SXPS catalogue.

[9] http://skyserver.sdss3.org/dr10/en/tools/chart/navi.aspx

A11 2FGL J1704.3+1235

Through the UK online analysis of the 2013 XRT data ($\sim$ 4800 s), covering the 2FGL J1704.3+1235 sky region, within the 3FGL (2FGL) 95 per cent semimajor axis error box of 4.2 arcmin (6.6 arcmin), we found only one bright X-ray source, XRT J170409+123421 (Fig. A11, upper left-hand panel), with a count rate of $6.418 \times 10^{-2} \pm 3.68 \times 10^{-3}$ counts s^{-1} . We consider it as the X-ray counterpart for this UGS. Looking at the close-up image (upper right-hand panel) of this X-ray source, with a positional error of 2.6 arcsec, is spatially coincident with the radio source NVSS J170409+123421, the IR source WISE J170409+123421 and the optical object SDSS J170409.58+123421.4. The broad-band SED is built by combining all the corresponding flux data and is shown in the bottom panel: The magenta points are the X-ray differential spectrum obtained by the UK online analysis. We find evidence for the possible contribution of a host galaxy assumed at $z = 0.3$, as illustrated by the green spectrum in Fig. A11.

A12 2FGL J2115.4+1213

In the 3FGL (2FGL) catalogue, 2FGL J2115.4+1213 is an unidentified object with a detection significance = 6.15σ (5.11σ) and a 95 per cent semimajor axis of 9.6 arcmin (8.4 arcmin). In 2012, the *Swift* satellite provided about 3800 s of X-ray data. Through the image analysis, we found that within the *Fermi* error box there are two X-ray sources detected (Fig. A12, upper panel). We propose as the likely X-ray counterpart of this UGS the brightest

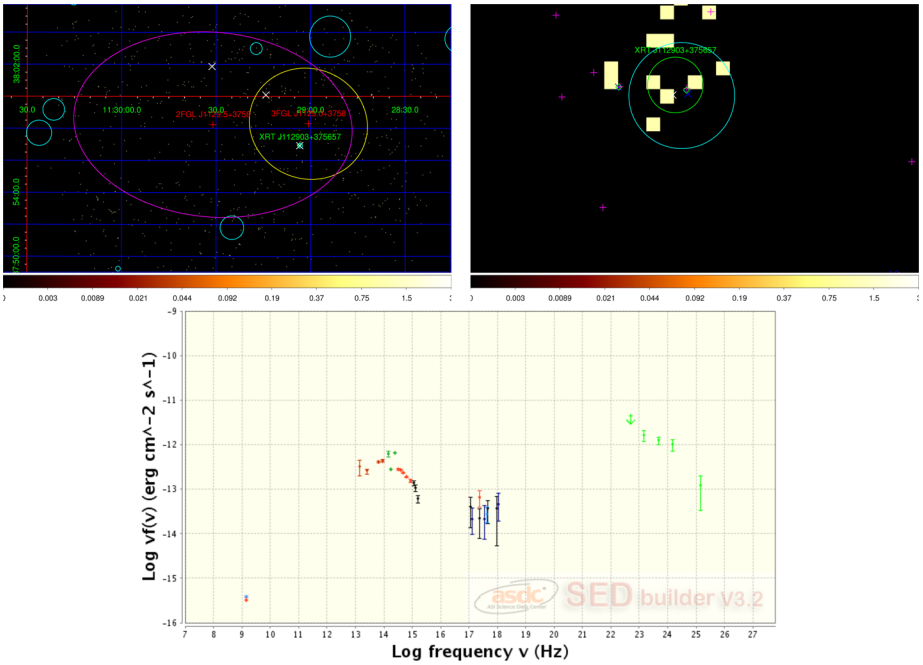

Figure A5. Upper left-hand panel: *Swift*/XRT images of the UGS 2FGL J1129.5 +3758 (3FGL J1129.0+3758) created using the online data analysis tool of the UK Swift Science Data Centre. The red crosses are the 2FGL J1129.5+3758 and 3FGL J1129.0+3758 positions, and the yellow (magenta) ellipse is the 95 per cent error region of 3FGL (2FGL) catalogue. The XRT sources detected in this work are displayed as green circles with a radius equal to the XRT error radius. The cyan ellipses show the error circles of the NVSS radio sources and the white crosses are the *Swift*/XRT objects of the 1SXPS catalogue. Upper right-hand panel: close-up of the XRT J112903−375857 sky map. The white cross is the position of the XRT source in the 1SXPS catalogue. The blue and magenta crosses are the positions of *WISE* and USNO objects, and the green diamonds correspond to 2MASS sources. Bottom panel: broad-band SED of 2FGL J1129.5+3758 and 3FGL J1129.0+3758 created using the SED Builder tool of the ASI ASDC Data Centre. We combine *WISE* and 2MASS IR data (brown points and dark green points, respectively) with the HE gamma-ray data (green points) from the 3FGL catalogue. The X-ray flux estimates by the 1SXPS catalogue are in blue and the black data points are taken from Takeuchi et al. (2013).

X-ray object (details in the corresponding table) with 30 counts and (RA, Dec.) = ($21^h15^m22\overset{s}{.}08$, $12°18'01\overset{''}{.}8$). In the middle panel, the multiwavelength SED of XRT J211522+121801 is shown with the close-up image that shows the multifrequency counterparts for XRT J211522+121801 within the X-ray error circle of radius 3.3 arcsec: the radio source NVSS J211522+121802, the IR objects WISE J211522+121802 and 2MASS 21152198+1218029, and the optical object SDSS J211522.00+121802.8.

A13 2FGL J2246.3+1549

In the 3FGL (2FGL) catalogue, this *Fermi* object has a detection significance of 9.47σ (8.21σ) and a 95 per cent semimajor axis of 3 arcmin (6.6 arcmin). This object is associated and classified as an active galaxy of uncertain type. *Swift*/XRT observed 2FGL J2246.3+1549 in 2010 for a total of 3381 s. The XRT sky map of the 2FGL J2246.3+1549 region is shown in Fig. A13 (upper left-hand panel), and only one X-ray source with (RA, Dec.) = ($22^h46^m05\overset{s}{.}1$, $+15°44'34\overset{''}{.}07$) is detected within the 2FGL error ellipse, with a count rate of $8.718 \times 10^{-3} \pm 1.648 \times 10^{-3}$ counts s^{-1}, and the integrated 0.3–10 keV flux is 4.1156×10^{-13} erg cm^{-2} s^{-1}. However, this X-ray source is not inside the 3FGL error region, but we decide to consider it as the likely X-ray counterpart for 2FGL J2246.3+1549 because it is the only X-ray source detected in the larger 2FGL error region, and, moreover, this choice is in agreement with the association provided by the 3FGL catalogue. From the close-up image (upper right-hand panel), within the X-ray positional error of 3.2 arcsec, we see that the radio source NVSS J224605+154437, the IR sources WISE J224604+154435 and 2MASS 22460500+1544352, and the optical object SDSS J224604.99+154435.3 can be associated with XRT J224605+154434. In the bottom panel, the broad-band SED built by combining the flux data points of the multifrequency counterparts is displayed.

A14 2FGL J2347.2+0707

2FGL J2347.2+0707 is an object of the 3FGL (2FGL) catalogue with detection significance = 13.83σ (7.2σ) and a 95 per cent semiaxis error of 3 arcmin (6.0 arcmin). In the 3FGL catalogue, the source is classified as an active galaxy of uncertain type and associated with the object TXS 2344+068. From the UK online analysis of the 2011 XRT data (∼5000 s), we obtain the X-ray count map of the 2FGL J2347.2+0707 sky region (Fig. A14, upper left-hand panel). Inside the 3FGL error ellipse, we have only one X-ray source detected from *Swift* with (RA, Dec.) = ($23^h46^m40\overset{s}{.}01$, $+07°05'07\overset{''}{.}0$) with a count rate of $2.090 \times 10^{-2} \pm 2.055 \times 10^{-3}$ counts s^{-1}. We propose this object as the most likely X-ray counterpart for 2FGL J2347.2+0707 in agreement with the 3FGL association. From the close-up image focused on XRT J234640+070507 (upper right-hand panel) within the X-ray error circle of 2.1 arcsec, we have the radio source NVSS J234639+070504, the optical source SDSS J234639.93+070506.8, and the IR objects WISE J234639+070506 and 2MASS 23463993+0705068. In the bottom panel, the multiwavelength SED of 2FGL J2347.2+0707 is shown with the X-ray differential spectrum obtained by our dedicated X-ray analysis (green points) and the 1SXPS data points (blue points).

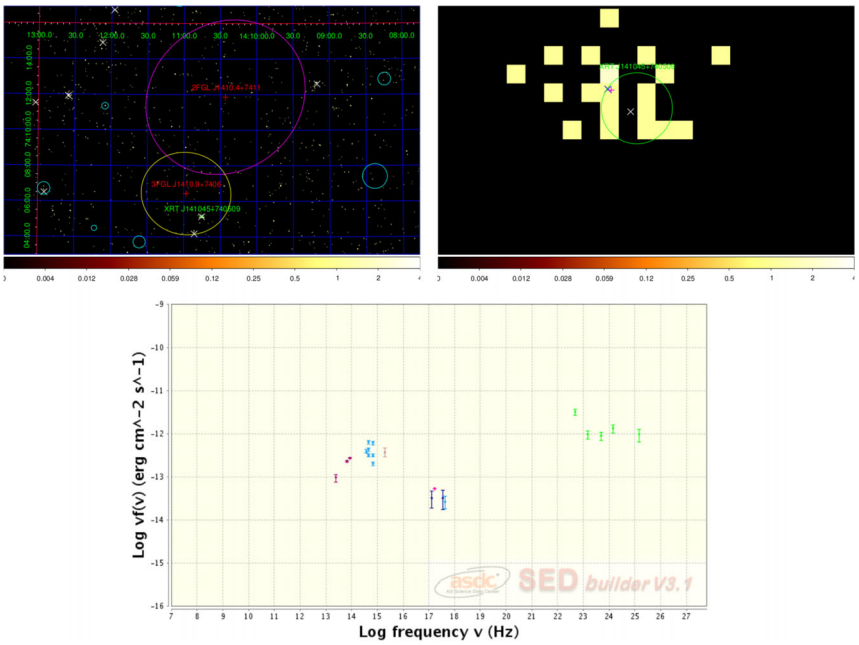

Figure A6. Upper left-hand panel: *Swift*/XRT images of the UGS 2FGL J1410.4 +7411 (3FGL J1410.9+7406) created using the online data analysis tool of the UK Swift Science Data Centre. The red crosses are the 2FGL J1410.4+7411 and 3FGL J1410.9+7406 positions, and the yellow (magenta) ellipse is the 95 per cent error region of 3FGL (2FGL) catalogue. The XRT sources detected in this work are displayed as green circles with a radius equal to the XRT error radius. The cyan ellipses show the error circles of the NVSS radio sources and the white crosses are the*Swift*/XRT objects of the 1SXPS catalogue. Upper right-hand panel: close-up of the XRT J141045+740609 sky map. The white cross is the position of the XRT source in the 1SXPS catalogue. The blue and magenta crosses are the positions of *WISE* and USNO objects, and the green diamonds correspond to 2MASS sources. Bottom panel: broad-band SED of the UGSs 2FGL J1410.4+7411 and 3FGL J1410.9+7406 created using the SED Builder tool of the ASI ASDC Data Centre. We combine *WISE* IR data (violet points) and USNO B1.0 optical data (light blue points) with the HE gamma-ray data (green points) from the 3FGL catalogue. The X-ray flux data points are taken from the 1SXPS catalogue (blue points).

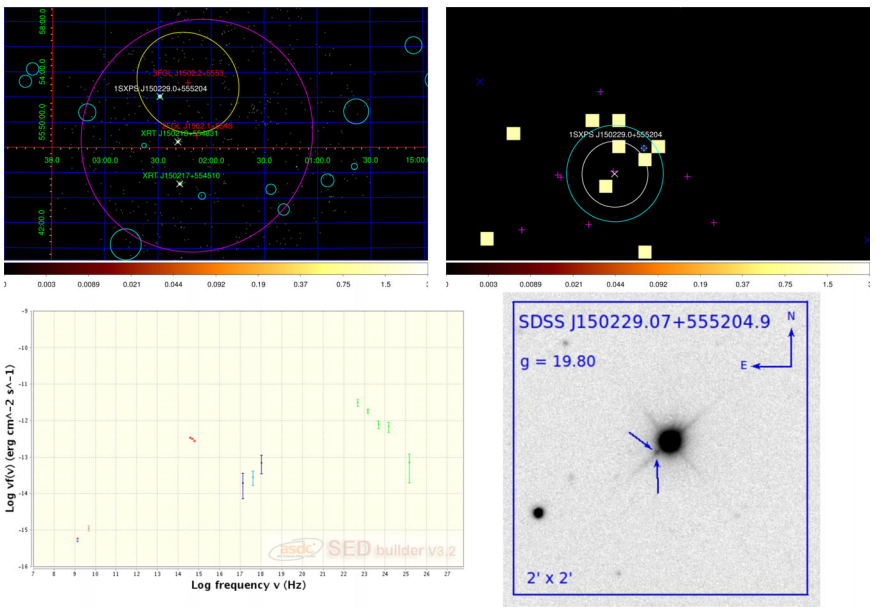

Figure A7. Upper left-hand panel: *Swift*/XRT image of 2FGL J1502.1 +5548 created using the online data analysis tool of the UK Swift Science Data Centre. The red cross is the 3FGL position and the yellow (magenta) ellipse is the 95 per cent error region of 3FGL (2FGL) catalogue. The XRT sources detected in this work are displayed as green circles. The cyan ellipses show the error circles of the NVSS radio sources and the white crosses are *Swift*/XRT objects of the 1SXPS catalogue (Evans et al. 2014). Upper right-hand panel: close-up of the 1SXPS J150229.0+555204 sky map. The white cross is the position of the XRT source in the 1SXPS catalogue. The blue and magenta crosses are the positions of *WISE* and SDSS objects, and the green diamonds correspond to 2MASS sources. Bottom left-hand panel: broad-band SED for the source 2FGL J1502.1+5548 created using the SED Builder tool of the ASI ASDC Data Centre. We combine the SDSS optical data (red points) with the HE gamma-ray data (green points) from the 3FGL catalogue. The X-ray flux points are from the 1SXPS catalogue (blue points). Bottom right-hand panel: optical finding chart centred on the optical source SDSS J150229.07+555204.9, the optical counterpart proposed for the UGS 2FGL J1502.1+5548.

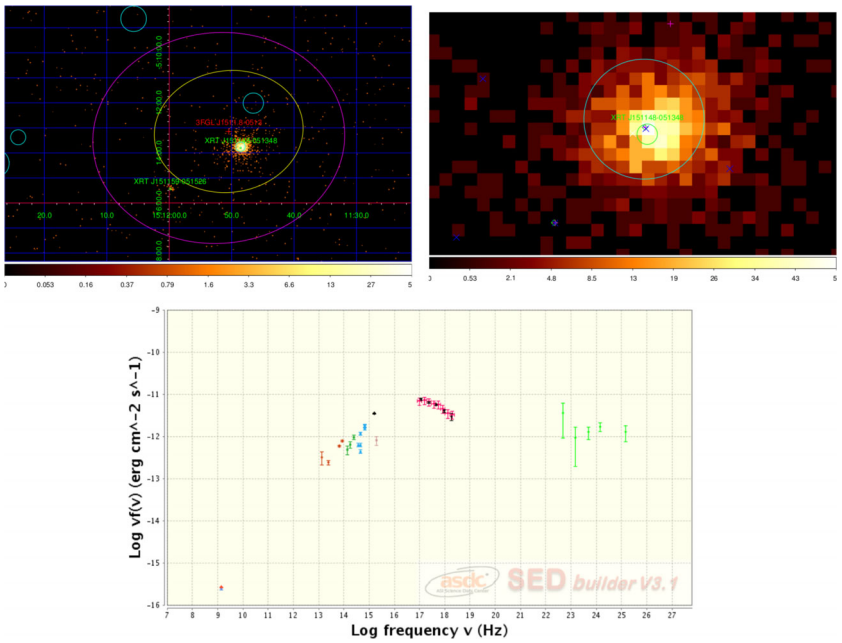

Figure A8. Upper left-hand panel: *Swift*/XRT image of 2FGL J1511.8 −0513 created using the online data analysis tool of the UK Swift Science Data Centre. The red cross is the 3FGL position and the yellow (magenta) ellipse is the 95 per cent error region of 3FGL (2FGL) catalogue. The XRT sources detected in this work are displayed as green circles. The cyan ellipses show the error circles of the NVSS radio sources and the white crosses are *Swift*/XRT objects of the 1SXPS catalogue (Evans et al. 2014). Upper right-hand panel: close-up of the XRT J151148−051348 sky map. The white cross is the position of the XRT source in the 1SXPS catalogue. The blue and magenta crosses are the positions of *WISE* and USNOB1.0 objects, and the green diamonds correspond to 2MASS sources. Bottom panel: broad-band SED for the source 2FGL J1511.8−0513 created using the SED Builder tool of the ASI ASDC Data Centre. We combine the *WISE* IR data (brown points), the 2MASS IR data (green points) and the USNOB1.0 optical data (light blue points) with the HE gamma-ray data (green points) from the 2FGL catalogue. The X-ray flux points are from the *Swift*-XRT data analysis performed in this work (magenta points), from the 1SXPS catalogue (blue points) and from Takeuchi et al. (2013) (black points).

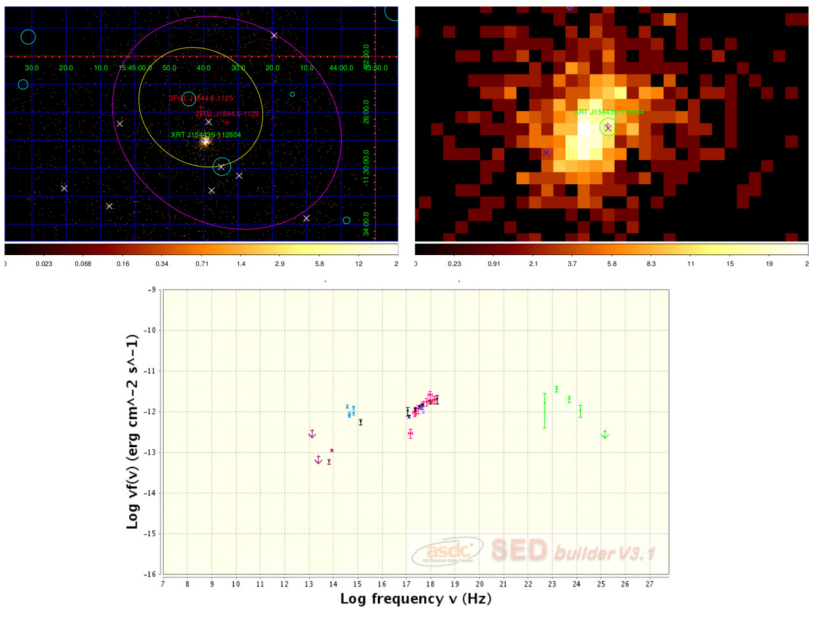

Figure A9. Upper left-hand panel: *Swift*/XRT images of 2FGL J1544.5 −1126 created using the online data analysis tool of the UK Swift Science Data Centre. The red crosses are the 2FGL and 3FGL positions and the yellow (magenta) ellipse is the 95 per cent error region of the 3FGL (2FGL) catalogue. The XRT sources detected in this work are displayed as green circles with a radius equal to the XRT error radius. The cyan ellipses show the error circles of the NVSS radio sources and the white crosses are the *Swift*/XRT objects of the 1SXPS catalogue. Upper right-hand panel: close-up of the XRT J154439−112804 sky map. The white cross is the position of the XRT source in the 1SXPS catalogue. The blue and magenta crosses are the positions of *WISE* and USNO objects, and the green diamonds correspond to 2MASS sources. Bottom panel: broad-band SED of the UGS 2FGL J1544.5−1126 created using the SED Builder tool of the ASI ASDC Data Centre. We combine *WISE* IR data (violet points) and USNO B1.0 optical data (light blue points) with the HE gamma-ray data (green points) from the 3FGL catalogue. The X-ray data points given from our *Swift*/XRT analysis are in magenta, while the data taken from Takeuchi et al. (2013) are in black and those from the 1SXPS catalogue in blue.

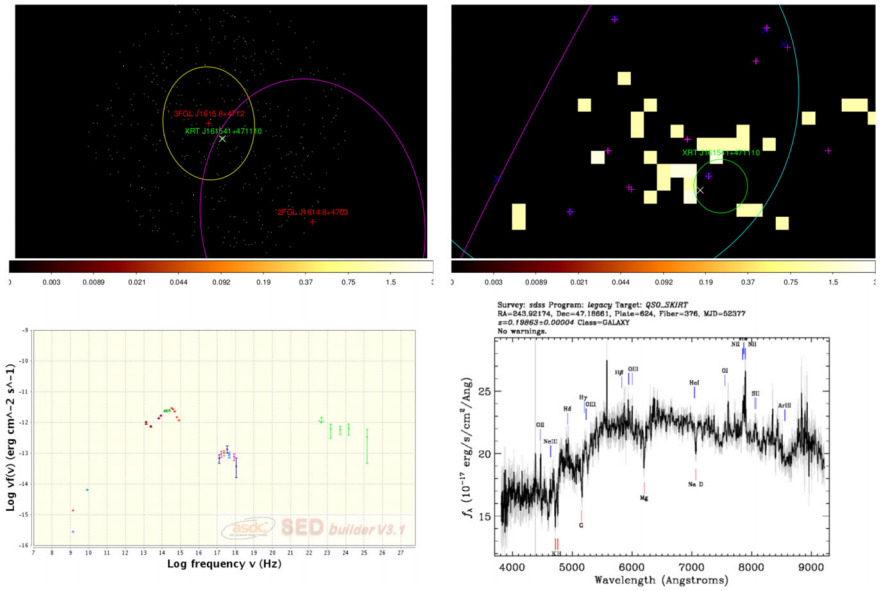

Figure A10. Upper left-hand panel: *Swift*/XRT image of 2FGL J1614.8 +4703 created using the online data analysis tool of the UK Swift Science Data Centre. The red crosses are the 2FGL J1614.8+4703 positions and the yellow (magenta) ellipse is the 95 per cent error region of 3FGL (2FGL) catalogue. The XRT sources detected in this work are displayed as green circles with a radius equal to the XRT error radius. The cyan circles show the error circles of the NVSS radio sources and the white crosses are the*Swift*/XRT objects of the 1SXPS catalogue. Upper right-hand panel: close-up of the XRT J161541+471110 sky map. The white cross is the position of the XRT source in the 1SXPS catalogue. The blue and magenta crosses are the positions of *WISE* and SDSS objects, and the green diamonds correspond to 2MASS sources. Bottom left-hand panel: broad-band SED for the UGS 2FGL J1614.8+4703 created using the SED Builder tool of the ASI ASDC Data Centre. We combine radio data, *WISE* IR data (brown points), the 2MASS IR data (green points) and the SDSS10 optical data (red points) with the HE gamma-ray data (green points) from the 3FGL catalogue. The X-ray flux points (magenta points) are performed from the *Swift*-XRT data analysis of this work, and the blue points are the X-ray data taken from the SXPS catalogue. Upper right-hand panel: optical spectrum for the optical counterpart provided by the SDSS survey.

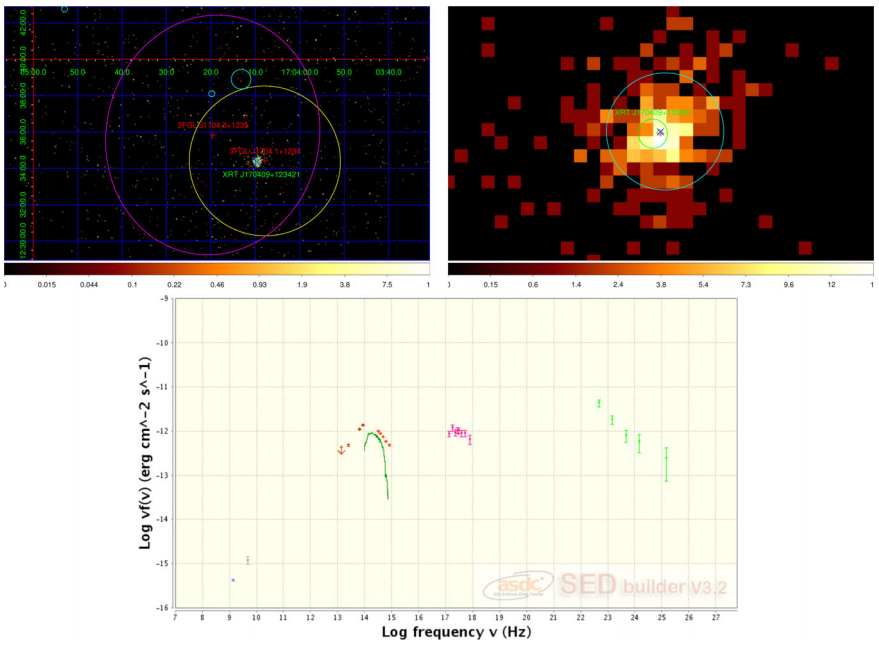

Figure A11. Upper left-hand panel: *Swift*/XRT image of the 2FGL J1704.3 +1235 created using the online data analysis tool of the UK Swift Science Data Centre. The red crosses are the 2FGL and 3FGL positions and the yellow ellipse is the 95 per cent error region of the 2FGL catalogue. The XRT sources detected in this work are displayed as green circles with a radius equal to the XRT error radius. The cyan circles show the error circles of the NVSS radio sources and the white crosses are the *Swift*/XRT objects of the 1SXPS catalogue. Upper right-hand panel: close-up of the XRT J170409+123421 sky map. The blue and magenta crosses are the positions of *WISE* and SDSS objects, and the green diamonds correspond to 2MASS sources. Bottom panel: broad-band SED for 2FGL J1704.3+1235 created using the SED Builder tool of the ASI ASDC Data Centre. We combine the *WISE* IR data (brown points), the 2MASS IR data (green points) and the SDSS10 optical data (red points) with the HE gamma-ray data (green points) from the 3FGL catalogue. The X-ray flux points (magenta points) are performed from the *Swift*-XRT data analysis of this work.

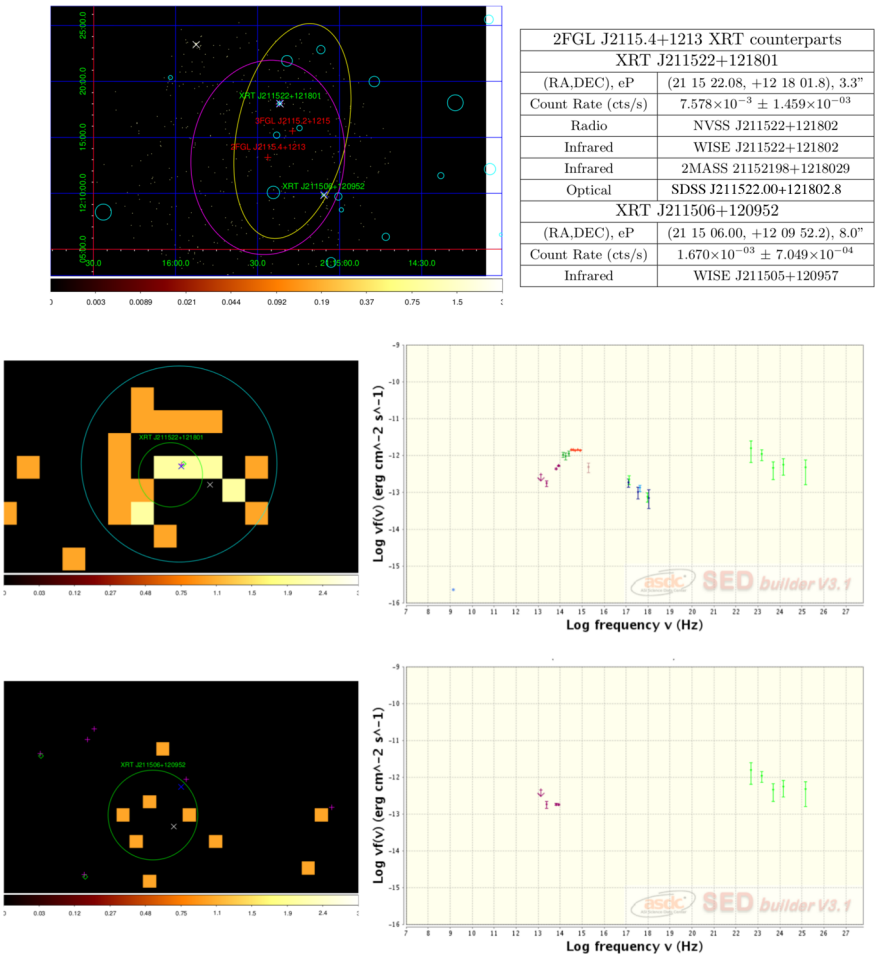

2FGL J2115.4+1213 XRT counterparts	
XRT J211522+121801	
(RA,DEC), eP	(21 15 22.08, +12 18 01.8), 3.3"
Count Rate (cts/s)	$7.578\times10^{-3} \pm 1.459\times10^{-03}$
Radio	NVSS J211522+121802
Infrared	WISE J211522+121802
Infrared	2MASS 21152198+1218029
Optical	SDSS J211522.00+121802.8
XRT J211506+120952	
(RA,DEC), eP	(21 15 06.00, +12 09 52.2), 8.0"
Count Rate (cts/s)	$1.670\times10^{-03} \pm 7.049\times10^{-04}$
Infrared	WISE J211505+120957

Figure A12. Upper panel: *Swift*/XRT image of the UGS 2FGL J2115.4 +1213 created using the online data analysis tool of the UK Swift Science Data Centre. The red crosses are the 3FGL (2FGL) positions and the yellow (magenta) ellipse is the 95 per cent error region of 3FGL (2FGL) catalogue. The XRT sources detected in this work are displayed as green circles. The cyan ellipses show the error circles of the NVSS radio sources and the white crosses are *Swift*/XRT objects of the 1SXPS (Evans et al. 2014). Middle left-hand panel: close-up of XRT J211522+121801 sky map. The white cross is the position of the XRT source in the 1SXPS catalogue. The blue and magenta crosses are the positions of *WISE* and USNOB1.0 objects, and the green diamonds correspond to 2MASS sources. Middle right-hand panel: broad-band SED for XRT J211522+121801 created using the SED Builder tool of the ASI ASDC Data Centre. We combine the *WISE* IR data (brown points), the 2MASS IR data (green points) and the USNOB1.0 optical data (light blue points) with the HE gamma-ray data (green points) from the 2FGL catalogue. The X-ray flux points (green points) are from the *Swift*-XRT data analysis performed in this work and from the 1SXPS catalogue (blue points). Bottom left-hand panel: close-up of the XRT J211506+120952 sky map. The white cross is the position of the XRT source in the 1SXPS catalogue. The blue and magenta crosses are the positions of *WISE* and USNOB1.0 objects, and the green diamonds correspond to 2MASS sources. Bottom right-hand panel: broad-band SED for XRT J211506+120952 created using the SED Builder tool of the ASI ASDC Data Centre. We combine the *WISE* (violet points) with the HE gamma-ray data (green points) from the 2FGL catalogue.

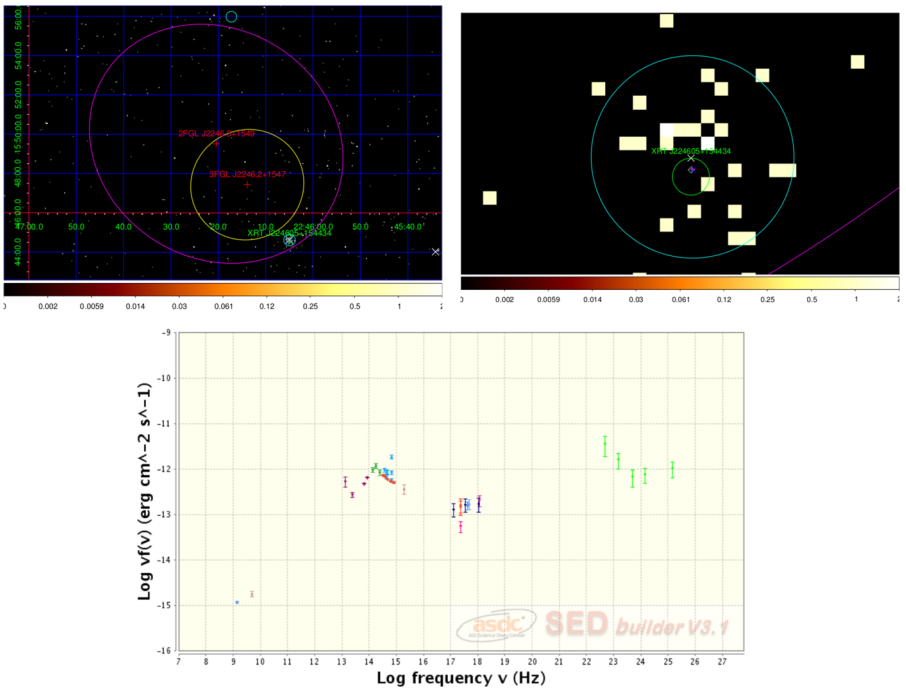

Figure A13. Upper left-hand panel: *Swift*/XRT image of 2FGL J2246.3 +1549 created using the online data analysis tool of the UK Swift Science Data Centre. The red crosses are the 2FGL J2246.3+1549 positions and the yellow (magenta) ellipse is the 95 per cent error region of the 3FGL (2FGL) catalogue. The XRT sources detected in this work are displayed as green circles with a radius equal to the XRT error radius. The cyan circles show the error circles of the NVSS radio sources and the white crosses are the *Swift*/XRT objects of the 1SXPS catalogue. Upper right-hand panel: close-up of XRT J224605+154434 sky map. The blue and magenta crosses are the positions of *WISE* and SDSS objects, and the green diamonds correspond to 2MASS sources. Bottom left-hand panel: broad-band SED for 2FGL J2246.3+1549 created using the SED Builder tool of the ASI ASDC Data Centre. We combine radio data, the *WISE* IR data (brown points), the 2MASS IR data (green points) and the SDSS10 optical data (red points) with the HE gamma-ray data (magenta points) from the 2FGL catalogue. The X-ray flux points are provided by our *Swift*-XRT data analysis (magenta points) and by the 1SXPS catalogue (blue points).

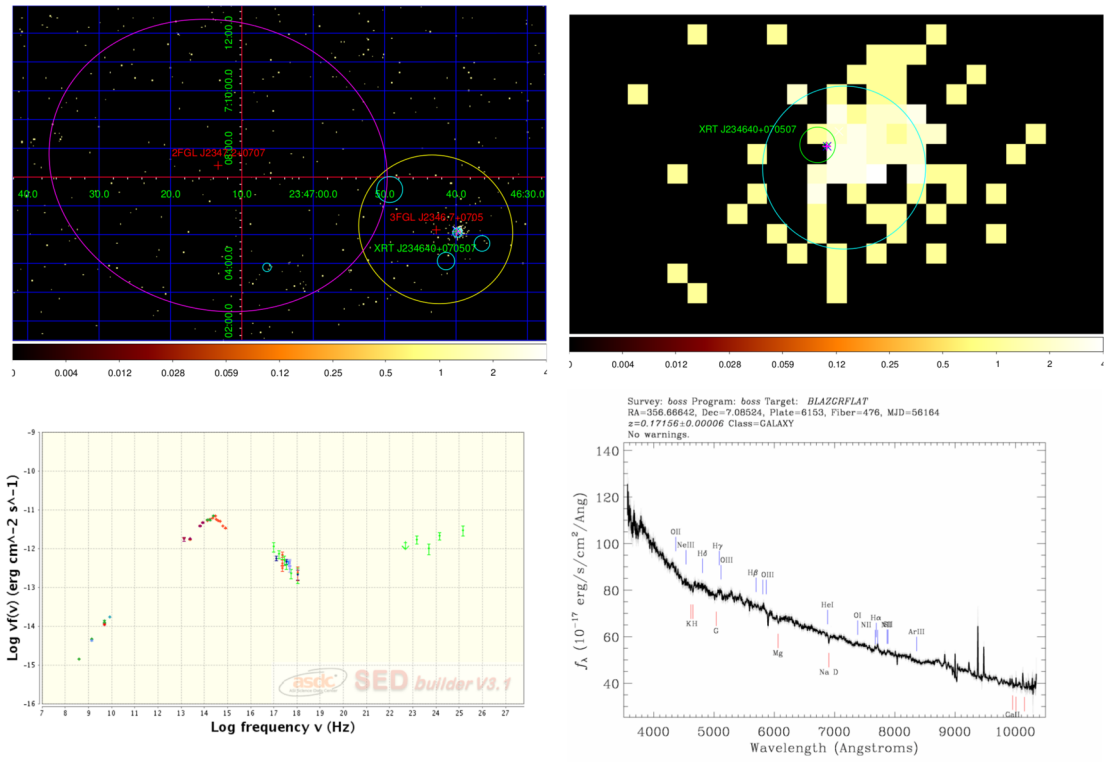

Figure A14. Upper left-hand panel: *Swift*/XRT image of 2FGL J2347.2+0707 created using the online data analysis tool of the UK Swift Science Data Centre. The red crosses are the 3FGL and 2FGL positions and the yellow (magenta) ellipse is the 95 per cent error region of 3FGL (2FGL) catalogue. The XRT sources detected in this work are displayed as green circles with a radius equal to the XRT error radius. The cyan circles show the error circles of the NVSS radio sources and the white crosses are the*Swift*/XRT objects of the 1SXPS catalogue. Upper right-hand panel: close-up of the XRT J234640+070507 sky map. The blue and magenta crosses are the positions of *WISE* and SDSS objects, and the green diamonds correspond to 2MASS sources. Bottom left-hand panel: broad-band SED for 2FGL J2347.2+0707 created using the SED Builder tool of the ASI ASDC Data Centre. We combine the *WISE* IR data (brown points), the 2MASS IR data (green points) and the SDSS10 optical data (red points) with the HE gamma-ray data (green points) from the 2FGL catalogue. The X-ray flux points are performed from the *Swift*-XRT data analysis of this work (green points) and taken from 1SXPS catalogue (blue points). Bottom right-hand panel: the SDSS optical spectrum of the optical counterpart 2FGL J2347.2+0707, which shows a power-law shape and indicates a *blazar* origin.

This paper has been typeset from a TEX/LATEX file prepared by the author.